Development and Application of a Synthetic Near Infrared Fluorescent Probe for Imaging Modulatory Neurotransmitters

By

Abraham G. Beyene

A dissertation submitted in partial satisfaction of the

requirements for the degree of

Doctor of Philosophy

in

Chemical Engineering

in the

Graduate Division

of the

University of California, Berkeley

Committee in charge:

Professor Markita Landry, Chair
Professor David Schaffer
Professor Wenjun Zhang
Professor Evan Miller

Fall 2019

Development and Application of a Synthetic Near Infrared Fluorescent Probe for Imaging Modulatory Neurotransmitters

by

Abraham G. Beyene

Abstract

Development and Application of a Synthetic Near Infrared Fluorescent Probe for Imaging Modulatory Neurotransmitters

by

Abraham G. Beyene

Doctor of Philosophy in Chemical Engineering

University of California, Berkeley

Professor Markita Landry, Chair

Dopamine neurotransmission plays critical roles in brain function in both health and disease and aberrations in dopamine neurotransmission are implicated in several psychiatric and neurological disorders, including schizophrenia, depression, anxiety, and Parkinson's disease. Until recently, measuring the dynamics of dopamine and other neurotransmitters of this class could not be achieved at spatiotemporal resolutions necessary to study how dopamine regulates the plasticity and function of neurons and neural circuits, and how dysfunctions in this regulation lead to disease. Probes that satisfy critical attributes in spatiotemporal resolution and chemical selectivity are needed to facilitate investigations of dopamine neurochemistry.

To address this need, this dissertation describes the synthesis and implementation of an ultrasensitive near-infrared "turn-on" nanosensor (nIRCat) for the catecholamine neuromodulators dopamine and norepinephrine. To guide probe development, we present results from a computational model that offers insight into the spatiotemporal dynamics of dopamine in the striatum, a subcortical structure that is enriched in dopamine. With this model, we elucidated the kinetic requirements for a prototypical optical indicator as well as optimal imaging framerates needed for measuring dopamine neurochemical dynamics. Stochastic modeling of dopamine dynamics, driven by kinetic phenomena of vesicular release, diffusion and clearance, provide a platform to evaluate dopaminergic volume transmission arising from a single terminal or ensemble terminal activity. With this work, we illustrate that only probes with kinetic parameters in a particular range are feasible for dopamine imaging at spatiotemporal scales likely to be encountered in brain tissue.

In two subsequent chapters, we describe the development and *in vitro* characterization of nIRCats, synthesized from functionalized single wall carbon nanotubes (SWCNT) that fluoresce in the near infrared range of the spectrum. We show that nIRCats exhibit maximal relative change in fluorescence intensity ($\Delta F/F_0$) of up to 35-fold in response to catecholamines and have optimal dynamic range that span physiological concentrations of their target brain analytes. Through a combination of experimental and molecular dynamics approaches, we elucidate the photophysical principles and

intermolecular interactions that govern the molecular recognition and fluorescence modulation of nIRCats by dopamine.

Finally, we demonstrate that nIRCat can be used to measure electrically and optogenetically evoked release of dopamine in striatal brain slices, revealing hotspots of activity with a median size of 2 μm, and exhibiting a log-normal size distribution that extends up to 10 μm. Moreover, nIRCats are shown to be compatible with dopamine pharmacology and permit studies of how receptor-targeting drugs modulate evoked dopamine release. Our results suggest nIRCats may uniquely support similar explorations of processes that regulate dopamine neuromodulation at the level of individual synapses, and exploration of the effects of receptor agonists and antagonists that are commonly used as psychiatric drugs and psychoactive molecules that modulate the release and clearance profiles of dopamine. We conclude that nIRCats and other nanosensors of this class can serve as versatile synthetic optical tools to monitor interneuronal chemical signaling in the brain extracellular space at spatial and temporal scales pertinent to the encoded information.

Table of Contents

Acknowledgements

Thank you to my dissertation advisor Professor Markita Landry. I am grateful to you for your vision and guidance, and for empowering me as a scientist to trust and pursue my intuitions at critical junctures of my training. I am deeply indebted to you for your tireless work to advance my career.

I would like to extend a deeply felt gratitude to our collaborators Professor Linda Wilbrecht and Dr. Kristen Delevich. You generously expended valuable time and resource on key aspects of my project and my training. Your mentorship over the years has benefited me in ways I cannot recount here.

I would like to thank Dr. Jackson Travis Del Bonis-O'Donnell for building the microscopy system that facilitated parts of my projects and for automating the data analysis workflow which significantly contributed to my efficiency.

I would like to acknowledge Professor Marla Feller for her mentorship and guidance on navigating several fellowship applications and for critical feedback on my manuscripts.

Thank you to Dr. Polina Kosillo for FSCV measurements and for advice on imaging experiments. Thank you to Dr. David Piekarski and Sarah Yang for help with imaging experiments. Thank you to Wan Chen Lin for help with optogenetics experiments.

I would like to thank my qualifying and dissertation committee members, Professor David Schaffer, Professor Wenjun Zhang, Professor Clay Radke and Professor Evan Miller, whom I have had the pleasure of being mentored by over the course of my training.

Thank you to Linda Chio, Darwin Yang and Gözde Demirer for embarking on this journey with me as the founding members of the Landry lab. Thank you to the rest of the Landry Lab members for making our lab a fun and collaborative place to do science.

I would like to acknowledge The UC Berkeley Regents, National Science Foundation, National Institutes of Health and Howard Hughes Medical Institute for financial support.

I would like to thank my parents for sparking in me a deep love for reading at a very young age. It is the best thing a parent can do for a child, and for that I am forever grateful.

Lastly and most importantly, I would like to thank my family. To my wife Ketsu, we embarked on this journey when we were kids and it is remarkable how far we have come. Thank you for being a steadfast partner all these years and for balancing my ever-serious outlook on life with a healthy dash of levity. To my daughter Christian, what a pleasure it has been to have you in our lives! I love you and I dedicate this work to you. To my dog Mocha, thank you for keeping me on my toes. Were it not for your incessant need for exercise, I would likely have succumbed to diabetes and completely missed out on California's beautiful parks.

Chapter 1

1.1 Introduction

Portions of this chapter are reproduced with permission from Ref 1.[1] *Copyright 2018. American Chemical Society.*

Communication between neurons is mediated by a series of electrical and chemical signaling modalities that occur in highly specialized structures called chemical synapses. When a neuron fires an action potential, a fast, depolarizing burst of electrical impulse propagates through its plasma membrane and travels down an axonal process where it invades presynaptic terminals and gates Ca^{2+}-permeable ion channels. The influx of Ca^{2+} triggers a biochemical machinery that induces exocytotic vesicle fusion and the release of neurotransmitters into the synaptic cleft, which diffuse across gap junctions and activate receptors on the recipient target neurons to produce postsynaptic signals. Chemical synapses constitute the fundamental processing units of the brain and enable interneural communications that underpin normal brain function.

A wide range of investigative methods have been developed to investigate the electrical activity of neurons and neuronal networks, spanning the realms of molecular biology, genetics, chemistry, optics, and engineering, and forming a nexus of discovery that has accelerated our understanding of how certain facets of brain function, such as memory and learning, are encoded by neuronal electrical activity. Whereas neuronal electrical excitability is a hallmark property of neurons and justifiably draws much attention, chemical signaling between neurons – mediated by hundreds of neurotransmitters, neuromodulators, hormones, and other signaling molecules – is equally important, but more elusive in its regulation of brain function for motor control, learning, and behavior. Tools that can monitor dynamic brain chemistry at pertinent spatial and temporal scales are necessary to advance our understanding of brain function but have been lagging tools for monitoring electrical activity in their robustness and sophistication.

In addition to the diversity of chemicals that neurons use to communicate, the modes of chemical signaling between neurons may also be different, which further complicates tool development. In a canonical fast synaptic neurotransmission, signaling is mediated by amino acids such as glutamate and γ-amino butyric acid (GABA), and occurs on millisecond time scales and over highly specialized nanoscale spatial domains, and results in the influx of ions through ligand-gated ion channels on postsynaptic neurons. On the other hand, unlike classical neurotransmitters, neuromodulators do not produce immediate electrical effects that excite or inhibit target neurons. Instead, neuromodulators tune the intrinsic or synaptic properties of neurons, most commonly through interaction with G-protein coupled receptors (GPCRs). Neuromodulators can escape the synaptic cleft and diffuse broadly, over micrometer length and second time scales, allowing them to influence the activity of many neurons in a state-dependent manner. Consequently, the spatial component of neuromodulatory signaling between neurons becomes important. The diversity of chemical species as well as the range of the relevant spatiotemporal dynamics adds to the challenges of developing effective methodologies for monitoring and manipulating neurochemistry.

1.2 Fluorescent Indicators of Neuronal Electrical and Chemical Activity

Advances in neuroscience are inextricably linked to the emergence of new tools and techniques that facilitate new discoveries by unraveling phenomena that elude inquiry through conventional methods. One of the earliest explorations in neuroanatomy utilized Golgi's silver staining method to visualize neuronal connectivity, which gave rise to the neuronal doctrine of modern neuroscience. In subsequent decades, developments in electrophysiology, driven by the invention of electrode or patch clamp recording techniques, facilitated recording of the electrical activity from small group of neurons at a time, enabling the first measurements of neuronal electrical activity in reduced preparations, and subsequently in awake behaving animals. In parallel, early investigations of dynamical neurochemical processes primarily relied on highly invasive techniques such as microdialysis, in which chemical analytes are recovered from the interstitial space of brain tissue by dialysis and characterized downstream using various analytical approaches such as liquid chromatography, capillary electrophoresis, and mass spectrometry. Amperometry and cyclic voltammetry enabled quantifying the neurochemistry of certain redox-active molecules in the brain with high temporal resolution. While these classical methods have contributed significantly to quantitative measurements of important brain analytes, they have low throughput, are highly invasive and do not operate at pertinent spatial resolutions. In recent decades, rapid advances in molecular biology, genetics, chemistry and microscopy have formed a synergistic nexus and provided a library of light-activated reporters and actuators of brain activity that are minimally invasive, highly targetable and operate with improved throughput, enabling recording of neuronal electrical and chemical activity over significant spatial scales.

Fluorescent activity indicators in particular have addressed the need for monitoring dynamical electrical and chemical activity of neurons at pertinent spatial and temporal scales. Such fluorescent indicators can be categorized into two broad families: genetically-encoded fluorescent proteins and synthetic fluorescent molecules. Genetically-encoded fluorescent indicators take a "nature knows best" strategy, in which naturally existing protein recognition motifs are conjugated to fluorescent proteins (FP). The conjugate is a chimeric construct capable of translating ligand-binding induced conformational changes to fluorescence intensity or Förster Resonance Energy Transfer (FRET) changes in the FP. These chimeric constructs can be expressed in the cytoplasm or plasma membrane of specific cellular populations via genetic engineering strategies. Genetically-encoded probes were initially developed for measuring calcium (Ca^{2+}) activity in neurons by coupling a calcium sensing protein (for example, calmodulin) to an FP (for example, GFP) via a short peptide linker. Alternative strategies use FRET as a read-out of protein conformational changes. In both approaches, iterative improvements over the course of nearly two decades have produced a diverse library of Ca^{2+} activity indicators with spectral properties, kinetics, sensitivity and targetability suited for a broad range of applications. Although not as mature as Ca^{2+} indicators, genetically-encoded voltage indicators (GEVI) have made impressive advances in the recent past and are rapidly becoming an indispensable part of the

neuroscience investigative toolkit. Most recently, genetic and protein engineering approaches have been expanded to generate fluorescent indicators for interneuronal chemical signaling molecules, including neurotransmitters and neuromodulators. [2–4]

Genetically-encoded probes demonstrate how advances in fluorescence microscopy, transgene delivery and protein engineering intersect to accelerate tool development for neuroscience research. Despite their success, protein-based probes have certain drawbacks that motivate the need for alternative platforms for sensor development. First, the spectrum of available colors in the fluorescent protein library is primarily limited to the visible range of the electromagnetic spectrum and there has so far been limited success in producing stable and bright far red and near infrared emissive FPs. Spectral overlap between optical indicators or actuators of neuronal activity in the visible range of the spectrum limit multiplexed usage. Additionally, scattering of visible-range photons by brain tissue adversely affects imaging depth and resolution. Moreover, genetically encoded probes rely on genetically tractable model organisms and require robust protein expression for successful implementation, which further motivates the need for approaches that do not require gene delivery and protein expression and can be rolled out seamlessly across many species and experimental preparations.

The second family of fluorescent indicators exploits synthetic small molecules to generate useful neural activity indicators. Before being supplanted by genetically encoded probes, the earliest Ca^{2+} activity indicators were generated from synthetic calcium chelating moieties (for example, BAPTA) that are covalently fused to organic fluorescent scaffolds (for example, fluorescein). Despite their lack of cellular specificity and challenges in delivery, small molecule organic fluorophores offer certain advantages over FPs: they tend to have superior photostability and brightness, which can be advantageous for capturing photon-limited fast transients at video rate temporal resolutions. Here too however, the spectrum of available colors is mostly confined within the visible-range (400 – 700 nm). Near-infrared emissive synthetic dyes are the subject of active research but still suffer from challenges of low quantum yield and poor photostability. Furthermore, whereas full and semi-synthetic Ca^{2+} and voltage activity reporters have been demonstrated, neurochemical sensing using synthetic constructs are yet to be demonstrated at any useful scale.

An alternative class of synthetic fluorescent species, including semiconducting fluorescent nanostructures such as transition metal quantum dots and graphitic nanomaterials, possess attributes that have recently drawn considerable interest from biological researchers. These nanocrystalline materials exhibit superior photostability, have large extinction coefficients, and a tunable emission spectrum that can be extended into the near infrared region of the spectrum. Fluorescent nanoparticles allow surface chemical modifications that can optimize their photophysical and chemical properties and they can be conjugated to motifs for molecular recognition and single particle tracking. Therefore, this class of synthetic fluorescent materials offer attributes that can be exploited to continue to address some of the outstanding needs in optical tool development, particularly within the context of neuroscience research.

This dissertation describes the use of a class of carbon nanostructures called single wall carbon nanotubes (SWCNT) as scaffolds for the synthesis and implementation of fluorescent indicators of neurochemical activity. SWCNT are semiconducting nanocrystals composed of sp^2-hybridized graphitic carbon atoms that are rolled seamlessly into cylindrical tubes of approximately 1 nm in diameter and length scales that can be up to four

orders of magnitude larger. In SWCNTs, quantum confinement effects in the radial dimension give rise to fascinating photophysical and electrical properties that draw interest from a myriad of fields. Within the context of biological imaging, SWCNTs exhibit superior photostability and fluorescence intrinsically in the relatively tissue-penetrating near infrared (NIR) range of the spectrum (1000 – 1300 nm), a window that has heretofore been largely inaccessible with organic synthetic molecules and FPs. Biological tissue exhibits remarkably diminished scattering and autofluorescence in this window of the spectrum, which in principle should allow imaging in deeper brain structures than may not be accessible with visible-photon emitting dyes. Moreover, the 1000 – 1300 nm window is sufficiently far removed from and possesses little spectral overlap with the existing suite of optical activity indicators and actuators. This suggests that SWCNT-based tools can be seamlessly implemented in conjunction with existing tools. Finally, chiral diversity of SWCNTs offers a palette of colors within the NIR region that offers tantalizing opportunities for ratiometric sensing and multiplexing within the NIR window of the spectrum.

Covalent and non-covalent strategies can be employed to conjugate recognition motifs to SWCNTs for the development of NIR-emissive fluorescent indicators. In this dissertation, we use non-covalent conjugation of SWCNT with amphiphilic biopolymers as recognition moieties to develop fluorescent indicators for catecholamine neuromodulators, a class of biogenic amines that play critical roles in a wide range of brain functions and are implicated in several neurological and psychiatric diseases. With this tool, we demonstrated optical detection of extracellular dopamine dynamics in *ex vivo* brain slices at micron spatial and sub-second temporal scales, which are resolutions pertinent to applications in molecular and circuit neuroscience. We conclude that SWCNT-based optical probes can offer a suite of NIR fluorescent activity indicators within a window of the electromagnetic spectrum that has considerable favorable attributes for biological research.

1.3 Outline of Dissertation

The contents of this dissertation are organized into the following chapters. We provide synopses and highlight conclusions from each chapter below.

Chapter 2

Here, we present a stochastic model of dopamine neuromodulation, which we developed from a first principles mathematical framework and with model parameters obtained from an extensive review of the neuroanatomical and physiological literature. We outline the temporal and spatial scales of dopamine neuromodulation within the striatal region of the basal ganglia as predicted by our model, arising from three competing dynamic processes: quantal dopamine release, diffusion and transporter-mediated clearance. Using this model, we asked what the kinetic requirements are for such an optical probe and what the optimal imaging parameters are for measuring the dynamics of dopamine in brain tissue at video frame rates. This model afforded identification a dopamine-to-probe binding affinity window and imaging frame rate that is optimal for recording dynamics in the striatum. This work provided valuable insights that contributed to sensor development and

guided subsequent endogenous dopamine imaging experiments in brain tissue, which are topics of subsequent chapters of this dissertation.

Chapter 3

Here, we discuss the development of a SWCNT-based "turn-on" sensor for the catecholamines dopamine and norepinephrine. The sensor is synthesized from noncovalent functionalizations of SWCNTs with single strand DNA (ssDNA) oligonucleotides. We present methodologies for sensor synthesis, experimental work that characterizes the spectroscopic properties of the probe and its performance in *in vitro* conditions. We show that non-covalent associations between ssDNA and SWCNTs form colloidal suspensions that exhibit exquisite "turn-on" sensitivity to and selectivity for dopamine and norepinephrine. We uncover experimentally accessible tuning parameters, including nucleobase chemistry, ssDNA oligonucleotide length, SWCNT bandgap and polymer surface density that play critical roles in setting the sensitivity and dynamic range of the probe.

Chapter 4

In this chapter, we introduce molecular dynamics simulation strategies to bridge macroscale experimental observations with molecular processes that underpin them. First, we will present results from molecular dynamics simulation studies that elucidate the organization of ssDNA oligonucleotide surface corona on SWCNTs. We explore the molecular processes that drive target recognition and the mechanisms of optical signal transduction within the underlying SWCNT-oligonucleotide scaffold for the dopamine sensor presented in Chapter 3. Our findings in this chapter rationalize key experimental observations and offer mechanistic insights into the influence of ssDNA oligonucleotide surface moieties on SWCNT photophysics and how interactions with dopamine molecules induce perturbations that engender SWCNT fluorescence modulation.

Chapter 5

In this chapter, we demonstrate that optical probes based on ssDNA-SWCNT technology can measure endogenous dopamine dynamics in *ex vivo* acute brain slices prepared from mice. We have named this nanosensor platform nIRCat, short for near infrared catecholamine nanosensor. Using nIRCats, we show hotspots of putative dopamine release in the dorsomedial striatum that are vary in size from 2 to 10 μm. We demonstrate the compatibility of nIRCats with pharmacological agents that modulate dopamine release and clearance from tissue. We show that nIRCats have the temporal and spatial resolution that enable investigations into presynaptic control of dopamine release, including how presynaptic control is modulated by dopamine receptor agonists and antagonists. We conclude that nIRCats and other similar probes of its class offer a valuable category of tools with unique photophysical attributes that can facilitate new discoveries in neuroscience.

Chapter 6

We summarize our work and offer concluding remarks for the dissertation.

Chapter 2

Simulations of Striatal Dopamine Neuromodulation for Design and Implementation of Optical Probes in Extracellular Space

Imaging the dynamic behavior of neuromodulatory neurotransmitters in the extracellular space arising from individual quantal releases would constitute an important addition to the neuroscience toolkit. The spatial and temporal scales of these highly stochastic events necessitate concurrent advances in the chemical development of optical probes selective for neuromodulators, in concert with advances in imaging methodologies to capture millisecond-scale neurotransmitter release. Here, we developed a stochastic model to describe the dynamics of the neuromodulator dopamine in extracellular space (ECS) of the brain dorsal striatum, which can be used to guide the design and implementation of optical probes that can record dynamical neurochemical processes in the ECS. Our model is developed from first principles and simulates release, diffusion, and reuptake of dopamine in a 3D simulation volume of striatal tissue. We find that imaging endogenous neuromodulatory dynamics requires simultaneous optimization of the probe's reversibility and sensitivity. Our work shows that dopamine imaging in the dorsal striatum is best accomplished with probes that have dissociation constant (K_d) on the order of 1 μM. Furthermore, as a result of the probabilistic nature of vesicular fusions that lead to quantal release, our model suggests that video frame rates of 20 Hz are optimal for recording temporally resolved release events. Our work provides a modeling platform to probe how neuromodulatory processes can be studied with optical indicators and enables facile assessment of probe kinetic properties and imaging framerates. Our stochastic model is generic for evaluating and optimizing fluorescent chemical activity indicators for brain systems whose neuroanatomical and neurophysiological properties are sufficiently understood.

2.1 Introduction

Diffuse volume transmission constitutes an important element of neuronal signaling for certain neurotransmitters such as acetylcholine, dopamine, norepinephrine, and serotonin. While classical neurotransmission is confined to communication between the pre- and postsynaptic neuron, and is mediated by fast acting ligand-gated ion channels, neuromodulation employs slower acting metabotropic receptors that exhibit a high level of extrasynaptic expression. [6] Thus, modulatory neurotransmitter activity extends well beyond the synapse. As a consequence, neuromodulators such as dopamine influence a population of neurons beyond the synapse, enabling a single neuron to modulate the activity of a larger network of connections. It is therefore of great interest to develop tools to observe and quantify the release, diffusion, and reuptake of neuromodulatory neurotransmitters such as

dopamine, where the spatial and temporal dynamics observed in the brain extracellular space (ECS) can be directly linked to receptor activation, neuronal activity modulation, and ultimately, behavior.

Among the most prominent dopaminergic systems are the nigrostriatal, mesocortical, and mesolimbic projections. Small clusters of dopamine neuron cell bodies located in the substantia nigra pars compacta (SNc) make extensive connections with the medium spiny neurons (MSN) of the dorsal striatum, forming the nigrostriatal pathway. [7,8] This pathway is responsible for controlling fine motor movements and its dysfunction underlies the pathology of Parkinson's disease.[9] Axons of dopaminergic cell bodies in the ventral tegmental area project into the nucleus accumbens and the prefrontal cortex, forming the mesolimbic and mesocortical pathways, respectively.[7,8] These systems play significant roles in cognitive control of behavior and reward processing, and their dysfunction contributes to the pathology of depression, addiction, schizophrenia and attention deficit hyperactivity disorder (ADHD), among others.[10–14] In all of these systems, neuromodulation, as opposed to neurotransmission, is the primary mode of influence. The diffusion-mediated transport of dopamine in the ECS is also known as volume transmission.[15]

One of the most ambitious pursuits in neuroscience is elucidating the relationship between neurons, neural circuits, behavior, and disease.[16] Successful chronic and real-time recording of neurotransmitter mediated chemical signaling would be a decisive step in that direction.[17] Current methods to measure the dynamics of dopamine volume transmission in ECS lack the spatial and/or temporal resolution of relevance to study neuromodulation. Voltammetry and amperometry are electrode-based methods used to record the presence of neuromodulators via redox chemistries yet require penetration of the brain tissue and only assay neurotransmitter concentration at one point in space. Optical probes include cell-based neurotransmitter fluorescent-engineered reporters (CNiFERs) that have been engineered to express a chimeric dopamine receptor and a genetically encoded calcium indicator.[18] CNiFERs utilize slow G-protein coupled receptor (GPCR) responses and thus do not report millisecond or micron-scale neurotransmitter activity. Fluorescent false neurotransmitters (FFNs) fluorescently label dopaminergic vesicles to provide single release site resolution but do not report the evolution of neurotransmitter concentrations in ECS.[19–21] Calcium imaging can show bouton activity in dopamine axons preceding release but tell us little about extracellular dopamine concentration. In sum, existing methods are insufficient to enable reliable measurements of dopamine and other modulatory neurotransmitters in the ECS with the necessary spatial and temporal resolutions pertinent to their neurophysiological function.

Over the last two decades, tremendous advances have been made in the development of optical activity indicators for two important facets of neuronal activity: cytoplasmic calcium dynamics and membrane voltage. These technologies provide excellent spatial and temporal resolutions at reasonably high throughput and with remarkable targetability.[22,23] However, development of probes for chemical signaling molecules have only made modest advances. One contributing factor in this lag is the lack of knowledge about the native spatiotemporal dynamics of neurochemicals, which hinders probe development. To address this need, we developed a mathematical model that estimates dopamine dynamics in striatal tissue and can therefore be used to guide probe development for implementation under *ex vivo* and *in vivo* imaging conditions. We coupled our model-derived dopamine dynamics with probe kinetic properties and found that only probes with kinetic properties in a small critical

window ($K_d \sim 1$ μM) are optimal for measuring dopamine dynamics. Probes with higher affinity ($K_d < 10$ nM) were found to be prone to saturation by tonic dopamine levels, which leads to diminished response to transient phasic dopamine signals. Probes with lower affinity ($K_d > 10$ μM) are likely to have a diminished overlap between their dynamic range and dopamine concentration ranges estimated by our model.

2.2 Results and Discussion

We model the diffusion driven dynamics of dopamine in the ECS of striatal tissue by numerically solving the diffusion equation with dopamine source and sink terms. Dopamine sources are the quantal releases from dopaminergic terminals within a defined simulation volume, while the reuptake of dopamine from the ECS acts as a sink. Reuptake parameters are assumed to be uniform throughout the simulation volume. We set the simulation volume as a cubic block of striatal tissue comprised of evenly interspaced dopamine terminals. A schematic of striatal tissue model with dopamine terminals depicted as yellow spheres is shown in Figure 2.1a. We use the nigrostriatal projection as a model system owing to its critical role in reward and reinforcement, addictive behavior, habit formation, and its implications for motor disorders, such as Parkinson's disease. Furthermore, the nigrostriatal system is well described in the literature, providing requisite physiological parameters relevant to dopaminergic neurotransmission with which to implement our model.

Simulation Volume

Dopamine terminals are the source of dopamine in our simulation, and dopamine transporters (DATs) drive dopamine reuptake. To elucidate the spatiotemporal dynamics of dopamine concentration in the ECS, we define our simulation space as a 1000 μm^3 (10 μm x 10 μm x 10 μm) volume of striatal neural tissue containing 100 dopaminergic terminals. Terminals are arranged in a periodic lattice structure filling the simulation volume. The structural and functional parameters of our simulation volume are summarized thus: (i) the density of dopaminergic terminals in the striatum, (ii) probability of dopamine release upon membrane depolarization, (iii) amount of dopamine released per quanta (per vesicle fusion), (iv) effective diffusivity of dopamine in tissue and (v) dopamine reuptake kinetics by DATs. A summary of parameter values and literature sources is provided in Table 1.

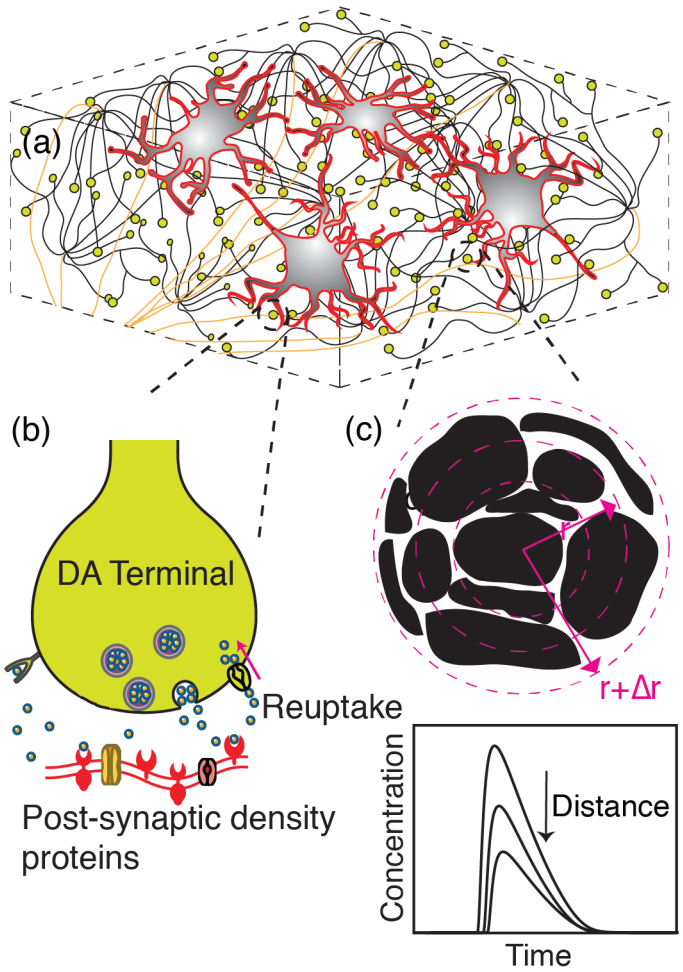

Figure 2.1 Schematic of dopamine model. (**a**) Dorsal striatum with medium spiny neurons (MSN - red contours/gray body), dopamine terminals (yellow), and projection axons (tan) from SNc. (**b**) A magnified view of an individual dopamine terminal forming a synapse onto a dendritic shaft of MSN. Dopamine release: An action potential causes a dopamine-containing vesicle to release dopamine into the synaptic cleft. Dopamine encounters post-synaptic receptor proteins, triggering further downstream neuronal processes. Dopamine reuptake: DATs clear dopamine from the ECS to be recycled. (**c**) Space discretization around a dopaminergic terminal representing tortuous morphology of brain tissue. Black represents tissue surrounded by void ECS. Concentric circles depict simulation volume elements. Inset graph: Dopamine concentration fluctuates in space and time as a result of release, diffusion and reuptake.

Model Representation of Dopamine Terminals

We define dopamine terminals as the boutons of axonal projections from the SNc into the dorsal striatum (Figure 2.1a). Cell bodies of dopaminergic neurons of the nigrostriatal pathway are located in the SNc and their axonal projections ascend into the dorsal striatum and make connections with dendritic spines or dendritic shafts of MSNs.[8,24,25] These ascending axonal tracts are notable for their high terminal density, where each axon is estimated to make on the order of 400,000 connections in the striatum.[26–28] A dopaminergic terminal contains a cluster of vesicles in close proximity to symmetric membrane densities, forming dopaminergic synapses with MSNs (Figure 2.1b). Asymmetric synapses also constitute a minority of synaptic configurations.[8] Our simulation considers these sites as

point release sources in a three dimensional space. We recreate the neuroanatomy within the simulation volume as described in previous computational studies.[29–32]

Table 2.1 Values of Simulation Parameters and Literature Sources

Parameter	Value	Ref.
Dopamine terminal density in the dorsal striatum (ρ_t)	0.1 μm^{-3}	[26]
Dopamine molecules released per quanta (Q_0)	5000	[29]
Terminal release probability ($\psi(p)$)	0.06	[19,20,30]
Effective diffusivity (D)	322 $\mu m^2 \cdot s^{-1}$	[29,35]
Void fraction of striatal tissue (α)	0.21	[36]
Maximum reuptake rate (r_{max})	4.1 $\mu M.s^{-1}$	[37]
Michaelis-Menten constant (K_m)	0.21 μM	[37]

Dopamine Release Sites and Probability of Release

Neurotransmitter release occurs at release sites within synapses. We execute our model for which each dopamine terminal possesses a single release site[33] (Figure 2.1b), where dopamine release probability per action potential per terminal is set to 6%.[30] The probability of quantal release is a function of the size of the readily releasable pool (RRP) in proportion to the total pool size which encompasses the RRP, the recycling, and reserve pools.[34] For dopaminergic activity in striatum, the low dopamine release probability is further supported by experimental results, which reveal that many dopamine terminals remain "silent" during stimulation.[19,20] We assume a constant probability of release and quantity of release in our simulation. Furthermore, membrane depolarization, which drives neurotransmitter release, is mediated by voltage-gated sodium channel activity which remain inactive for ~10 ms following an action potential. Thus, we impose a constraint in our simulation to limit sequential dopamine release events to occur at intervals greater than 10 ms per terminal, for a 100 Hz maximum release rate for any given terminal. Despite this maximum release rate, the low probability of release makes it such that the 100 Hz boundary condition is rarely encountered in our simulations.

Simulation of Release, Diffusion and Reuptake

Our simulation of dopamine concentration in the ECS invokes the equation of change for species conservation surrounding a dopaminergic terminal[31]

$$\frac{\partial c(r,t)}{\partial t} = D\nabla^2 c(r,t) + Q(r,t) - U(r,t) \qquad 1$$

where *c(r,t)* represents spatial (*r*) and temporal (*t*) variation in dopamine concentration, and *Q(r,t)* and *U(r,t)* represent quantal release of dopamine into the ECS and reuptake by DATs, respectively. *D* is the effective diffusivity of dopamine in tissue after accounting for tortuosity of brain tissue.[35,36] We solve this governing equation at each dopamine release terminal using finite difference method, and obtain the solution for temporal and spatial dopamine dynamics resulting from release from one dopamine terminal. Striatal tissue is composed of approximately 1 terminal per 10 μm^3.[26,28] With this terminal density, we determine the temporal profile of dopamine concentration resulting from the activity of all terminals included in the simulation volume of interest as described in Methods in Appendix I. Lastly, we discretize the governing equation to solve it numerically, since no known analytical solutions exist for this equation. The difference equation is written in spherical coordinates as forward difference in time and central difference in space.

Quantal Release

In equation 1, *Q(r,t)* represents quantal dopamine release following vesicle fusion and is represented by:

$$Q(r,t) = \frac{(Q_0 / N_A)}{\alpha[2\pi(dr)^2]^{3/2}}\left(\frac{e^{-(n-1)^2}}{1.386}\right)\psi(p)\delta(t - t_f) \qquad 2$$

where Q_0 represents the number of dopamine molecules released per exocytosis event and N_A represents Avogadro's number. The parameter ψ assumes a value of 1 or 0 based on a release probability *p.* A release event increases the concentration of the first spatial element of the simulation volume (Figure 2.1c) by an amount represented by:

$$\frac{(Q_0 / N_A)}{\alpha[2\pi(dr)^2]^{3/2}}\left(\frac{1}{1.386}\right) \qquad 3$$

This is the volume element immediately surrounding the location of the dopamine release site (Figure 2.1b, c). The parameter α accounts for porosity of brain tissue.[31] We use a Gaussian probability density function to determine the spatial distribution of dopamine immediately after release, normalized to ensure that only 5000 (Q_0) molecules of dopamine are released per quanta (Table 1). Dopamine spillover after quantal release is instantaneous.[29] Thus, a quantal release event affects the concentration of volume elements away from the center of the release site by an amount equal to the increase in the center of the release site (eqn. 3) scaled by an exponential decay term, $e^{-(n-1)^2}$. This exponential term is a function of the distance of the volume element from the center of the release site *r = (n-1)dr*, where *n* represents the spatial index, *n = 1, 2…N,* representing each volume element in the simulation. The sum of this exponential scaling term over the spatial indices gives rise to the normalization constant, 1.386. Firing frequency (*F*) sets the number of action

potentials over a given simulation period. The temporal distribution of action potentials over the simulation time period, t_f, is modeled as a Poisson distribution with mean a firing rate of F. $\delta(t - t_f)$ is a delta function in time and ensures that release can only occur during an action potential firing event with a binary probability ψ.

Dopamine Reuptake (U)

Reuptake of dopamine from the ECS occurs via DATs. In our model, we assume a uniform distribution of DATs in the simulation volume and model dopamine reuptake with a Michaelis-Menten rate equation with parameters r_{max} and K_m and in a medium of porosity α. [31,37]

$$U(r,t) = \frac{r_{\max} c(r,t)}{\alpha(c(r,t) + K_m)} \qquad 4$$

Dopamine saturation must be taken into account especially for simulation regions in close proximity to a terminal, where dopamine concentration immediately following a release can be very high. This non-linear expression allows for saturation of the dopamine reuptake process at high physiological dopamine concentrations, corresponding to the case of transporter saturation.

Single Terminal Behavior

The spatiotemporal dynamics of dopamine in the ECS following release from a single terminal influences dopamine receptors within the diffusion volume prior to dopamine reuptake. Dopamine is the primary endogenous ligand for two dopamine receptor sub-classes: D_1-type and D_2-type receptors, with EC_{50} binding affinities of 1 μM and 10 nM respectively.[29,38] We define the sphere of influence of a quantal release of dopamine after release from a terminal based on these activation EC_{50} values.[29] Our simulation shows that for a single quantal release from a terminal, the sphere of influence on low affinity D_1-type receptors and high affinity D_2-type receptors is 7 μm and 17 μm, respectively (Figure 2.3a). The spatiotemporal dynamics of a quantal release from a single terminal over a 20 μm radial distance shown in Figures 2.2a,b, Figure 2.3a and Figure 2.S1, is consistent with prior studies that show that dopamine diffuses from synaptic termini in quantities that overflow the synaptic cleft, giving rise to dopamine volume transmission.[29,32]

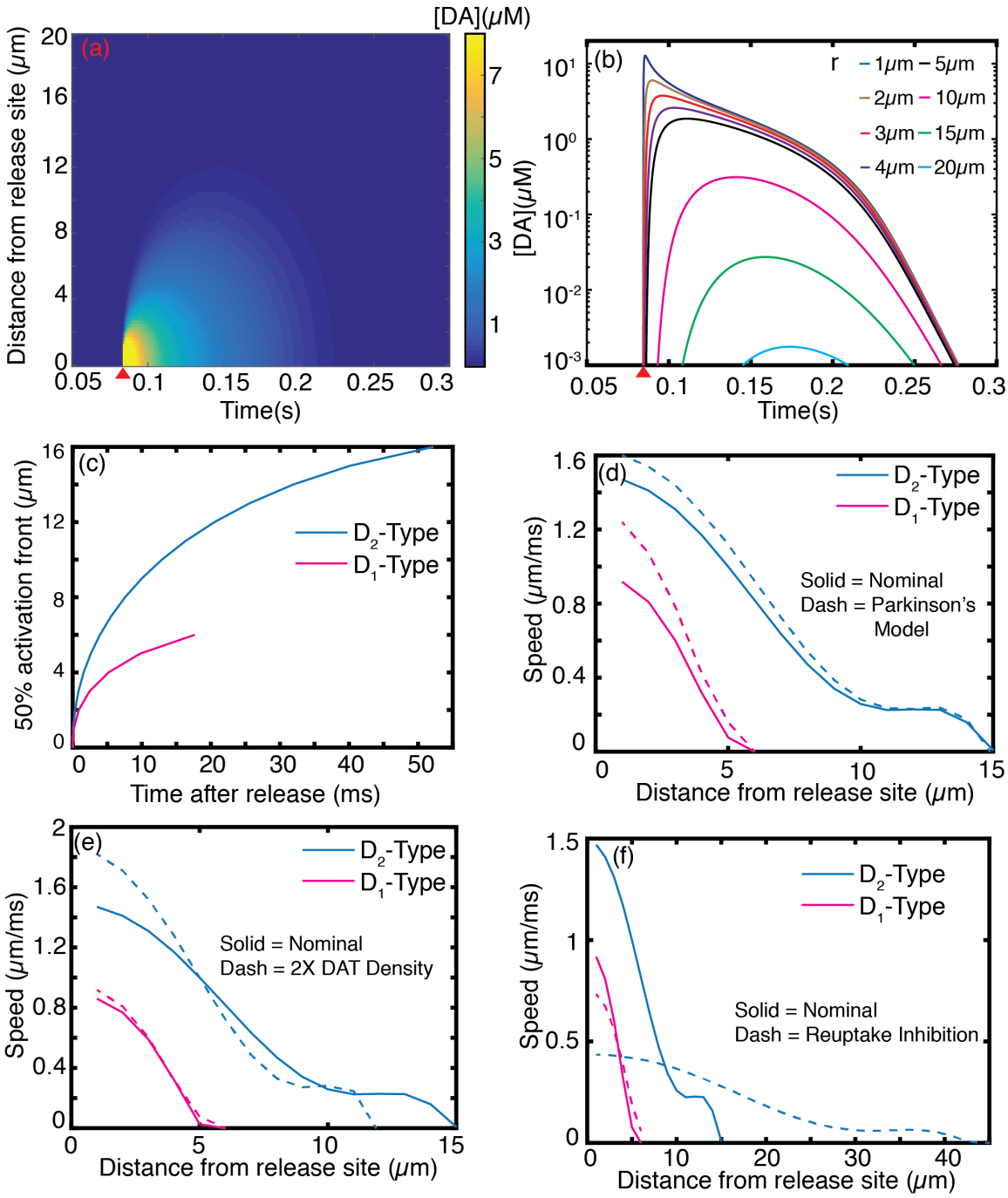

Figure 2.2 Spatiotemporal dopamine dynamics following a single action potential driven quantal release of dopamine. (**a**) Dopamine concentration profile evolution following a single quantal release as a function of distance and time. Red wedge indicates quantal dopamine release. (**b**) Dopamine spatial concentration profile at varying distances from release site. (**c**) Front (instance where EC_{50} is exceeded) of dopamine receptor activation following dopamine release for D_1 (pink) and D_2 (blue) type receptors. (**d**) Propagation speed of D_1 and D_2-type receptor activation after a quantal release obtained from first derivative of (**c**) (solid trace) compared with propagation speed obtained with porosity and tortuosity of ECS in Parkinson's disease. (**e**) Nominal propagation speeds compared with speeds computed with DAT density increased by a factor of 2. (**f**) Nominal propagation speeds compared with speeds in which dopamine clearance is competitively inhibited.

Dopamine propagation from the center of the synaptic cleft occurs on short time scales relative to dopamine diffusive effects. Our simulation shows that the activation EC_{50} for both D_2 and D_1-type receptors within the sphere of influence of a terminal are exceeded within 50 ms and 20 ms of dopamine release, respectively (Figure 2.2c). Furthermore, we compute the speed of propagation of receptor activation as a function of distance from the release site (Figure 2.2d, solid). The D_2-type receptor activation EC_{50} wave front (10 nM dopamine) moves forward at peak speeds approaching 1.5 μm/ms and slows to 0 μm/ms as a function of distance from the release site. Similarly, we observe peak propagation speeds of 1 μm/ms for D_1-type receptor activation (1 μM of dopamine). Our simulations provide estimates for speeds of dopamine volume transmission, and the time dependence of dopamine's activity on distal receptors from the release point. As expected, dopamine volume propagation speeds we compute for D_1- and D_2-type receptors is four to five orders of magnitude slower than reported speeds of electrical signal propagation in nerve fibers. To our knowledge, this is the first quantitative report on the speed of chemical signaling of dopamine in the dorsal striatum.

We studied the effect of varying simulation parameters on the speed of signal propagation in the striatum. Changes in morphology of the ECS in disease states and under hypoxic conditions could affect dopamine volume transmission. Brain tissue afflicted by Parkinson's disease shows changes in the tortuosity and porosity of the ECS morphology, where porosity and tortuosity decrease by 33% and 5% respectively.[39] When such parameters are varied in our simulation, we observe modest increases in the speed of propagation for both D_1 and D_2 receptor types, with the effect being slightly higher for D_1-type receptors (Figure 2.2d). We next explored the anisotropy of volume transmission that could arise from heterogeneous DAT expression. When we double the density of DATs, we observe enhanced transmission speeds for D_2-type receptors for proximal regions that are co-localized with high DAT expressions, and slower transmission speeds for distal sites and a correspondingly reduced overall sphere of influence (Figure 2.2e). On the other hand, competitive inhibition of DATs by cocaine slows the speed of D_2-type receptor activation but increases the activation sphere of influence (Figure 2.2f, Figure 2.3c). Combined, these results suggest that anisotropy in dopamine neuromodulation could in part be driven by heterogeneities in capacity for dopamine clearance in the striatum. In regions close to the release site (< 5 μm), high DAT expression creates a concentration gradient driving force that speeds up the activation of colocalized receptors, whereas reuptake inhibition slows the speed of volume transmission.

Non-linear reuptake kinetics we defined in equation 4 is sometimes approximated by a linear expression of the form $(r_{max}/K_m)c(r,t)$.[31] While a linear approximation of dopamine reuptake facilitates an analytical solution for the governing equation, linearization creates significant deviation from dopamine dynamic behavior obtained with non-linear reuptake kinetics (Figure 2.3a). The impact of the linear approximation on dopamine reuptake kinetics arises from neglecting the fact that DATs in close proximity to the releasing terminal are saturated ($c(r,t) >> K_m$) and can only clear dopamine at a maximum rate of r_{max}. The linear approximation overestimates uptake in regions proximal to the point of dopamine release, resulting in different linear versus non-linear reuptake kinetics. Our model implements non-linear reuptake kinetics with a Michaelis-Menten rate equation, and enables us to calculate the spatial sphere of influence with the biologically-relevant influence of saturating dopamine reuptake proximal to the release site. Indeed, our results show the spatial sphere

of influence with linear uptake is only half of that obtained with non-linear kinetics for D_1-type receptors (Figure 2.3a). To demonstrate the importance of treating the reuptake kinetics as a non-linear saturable process, we compared the linear model at nominal r_{max} and K_m values (Table 1) with a non-linear model in which r_{max} was increased by a factor of 10 (equivalent to increasing the density of DATs by an order of magnitude) and found the two dynamic behaviors to be comparable (Figure 2.S2). Our results exemplify the importance of treating dopamine clearance from ECS as a non-linear process, especially when spatial and temporal domains are simultaneously considered, and provide a quantitative comparison between linear and non-linear reuptake on the dynamics of dopamine in ECS.

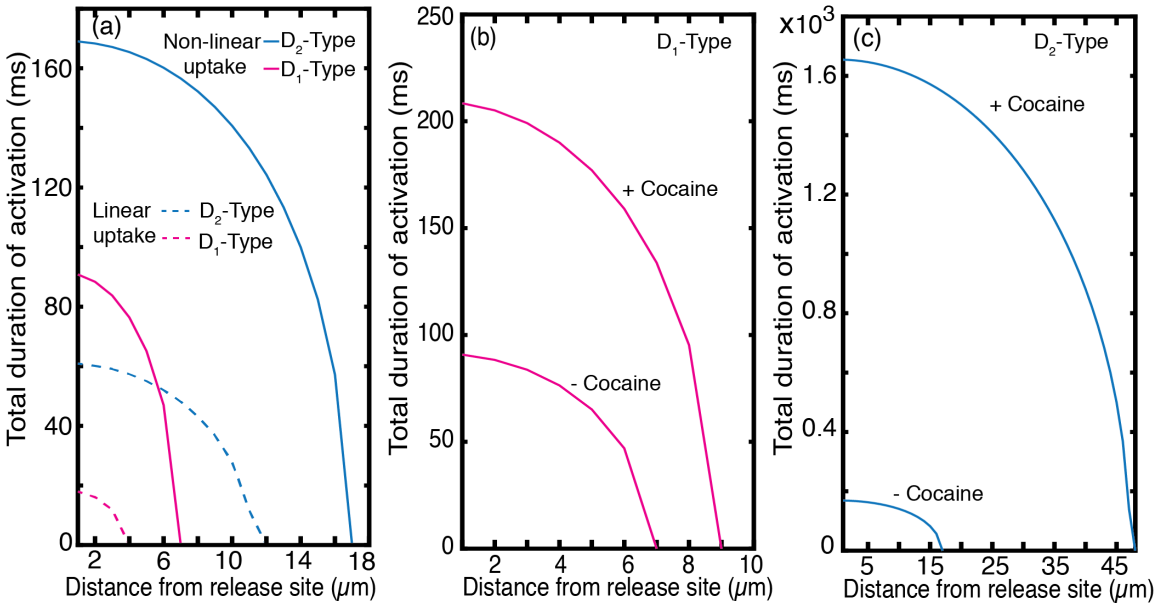

Figure 2.3 Non-linear computation of receptor activation by dopamine diffusion. (**a**) Sphere of influence of a single dopaminergic terminal over D_1- and D_2-type receptors. Time over which the EC_{50} of each receptor type is exceeded is plotted as a function of distance from the terminal. D_1- type receptors are insensitive to quantal release at 7 μm radial distance beyond the release site, whereas D_2-type receptors can be influenced by a single quantal release through a radial distance of 17 μm. The duration during which the EC_{50} of each receptor type is exceeded decreases monotonically with distance. Broken lines represent spheres of influence of linear uptake kinetics with the nominal r_{max} and K_m values listed in Table 1. (**b**) Effect of dopamine reuptake blocker, cocaine, on sphere of influence of D_1-type receptors, plotted as receptor activation duration as a function of distance from release site. (**c**) The same competitive inhibition effect on D_2-type receptor activation. Cocaine increases the sphere of influence on D_2-type receptors dramatically.

Certain psychostimulants act by competitively binding to DATs and modulating dopamine clearance rate from the ECS. We demonstrate the applicability of our model to probe the neurophysiology of dopaminergic systems by testing the effect of dopamine reuptake inhibition by cocaine. Cocaine has been shown to increase the affinity parameter in equation 4, K_m, from 0.21 μM to 8 μM.[40] Our simulation shows that inhibition of dopamine reuptake by cocaine increases the duration of D_1-type receptor activation by up to two fold and that of D_2-type receptors by up to six fold (Figure 2.3b, c). The spatial spheres of influence from a quantal release increase from 7 μm to 9 μm, and from 17 μm to 47 μm, for D_1 and D_2-type receptors, respectively. Our results suggest that competitive inhibitors –

whether therapeutic or abusive – have drastic effects on the dopamine sphere of influence for a singular dopamine terminal, the extent of which is best demonstrated when we model dopamine reuptake as a non-linear process.

Many-Terminal Behavior

Dynamic dopamine behavior at a point in the striatal ECS is influenced by the behavior of all active terminals in the vicinity. Dopaminergic neurons exhibit slow tonic and fast burst firing activity.[41,42] A burst in firing activity correlates with reward reinforcement as a response to salient events, whereby striatal dopamine neurons burst in spike trains of 4 to 7 spikes per burst event at a spiking frequency of 20 Hz.[42–44] Conversely, a pause in firing is correlated with response to adverse events or withdrawal of an expected reward. Tonic activity underlies dopaminergic activity at rest.[41–44] We implement our model to calculate dopamine concentrations in a volume of striatal brain tissue for a simulated spike train of physiological relevance. To account for the neurologically relevant case of collective multi-terminal activity, we extend our model to employ spatiotemporal summation of solutions from each terminal surrounding of a point of interest in the ECS (Methods in Appendix I). To this end, we evaluate spatiotemporal dopamine dynamics at a point of interest surrounded by 100 dopamine terminals (Figure 2.4a) and, separately, at a point surrounded by 25 terminals (Figure 2.4b) arranged at uniformly spaced cubic lattice points, with no terminal located closer than 2 μm to the point of interest. The terminal spacing of each cluster is based on density parameter defined in Table 1. We chose an extrasynaptic point located at least 2 μm from the closest terminal to avoid capturing the dominant behavior of synaptic dopamine hot spots in which behavior is dominated by the firing activity of the closest terminal. We simulate a 2-second spike train representative of phasic firing behavior by implementing our model over four distinct firing regimes (Figure 2.4a, b). The simulated firing frequency and duration is chosen based on experimentally observed *in vivo* spiking activity of dopaminergic neurons[42,43]: we simulate an ensemble of dopaminergic neurons undergoing a 4 Hz tonic firing rate for t = 0 to t = 0.4 s, followed by a 20 Hz burst firing regime for t= 0.4 s to t = 0.7 s, followed by a 0.5 s pause (0 Hz) until t = 1.2 s. For the last 0.8 s of the simulation, we return to a 4 Hz tonic firing regime. Note that each firing rate is the mean of a Poisson distribution of firing rates among the ensemble, as we described in preceding sections and in Methods in Appendix I. The simulation ensemble size is commensurate with experimental fast scan cyclic voltammetry (FSCV) assays where the carbon fiber electrode samples dopamine overflow from a region encompassing ~100 dopaminergic terminals.[21]

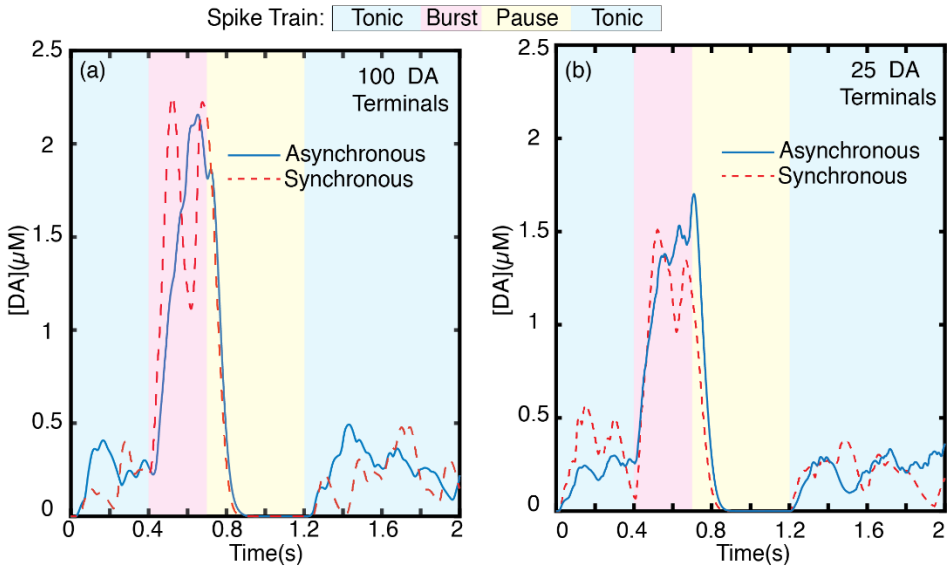

Figure 2.4 Dopamine concentration evolution profile for a simulated volume. Dopamine dynamics at an extrasynaptic point surrounded by (**a**) 100 and (**b**) 25 phasically firing dopaminergic neurons with asynchronous firing (blue trace, solid) and synchronous firing (red trace, dash). Each trace represents the average of N=20 independent simulation runs.

We present results from a cluster of 100 dopaminergic terminals and 25 dopaminergic terminals firing phasically with the above-described spike train to highlight how the underlying functional connectivity of terminals can result in different spatiotemporal dopamine behavior. While the firing activity of an individual or a pair of dopaminergic neurons is well studied, the number of terminals in a phasically firing ensemble is not well understood.[43,45] It is predicted that functional or sub-functional connectivity influences the size of phasically firing ensembles and their synchrony.[43] As such, we simulate a spike train from a phasically firing cluster of 100 dopaminergic terminals (Figure 2.4a) compared to a cluster of 25 dopaminergic terminals (Figure 2.4b) firing synchronously or asynchronously. Dopamine release is a highly stochastic process and the results presented here are average behavior from N = 20 separate runs of our simulation. We present individual simulation runs and run average for the 100 terminal asynchronous firing case in Figure 2.S3. In both terminal clusters, asynchronous firing results in a more temporally homogenous concentration profile. Synchronous firing concentration profiles exhibit sharp dopamine concentration transience in all firing regimes (Figure 2.4a, b). Peak dopamine concentration during burst phase is modestly higher for the 100-terminal cluster, and its scale and diffusion also has a larger spatial extent. Tonic dopamine concentration levels, however, are roughly the same for both the 100 and 25 terminal clusters. For both simulated terminal cluster sizes, tonic asynchronous firing gives rise to a steady basal dopamine level whereas synchronous firing does not. The pause in firing following burst firing activity clears dopamine from the ECS in both cases; complete clearance is achieved within 150 ms of the onset of pause in firing. The observation that tonic dopamine concentrations are mediated by uncorrelated, asynchronous firing is in agreement with prior studies, which show that tonic activity gives rise to the basal dopamine level measured in ECS.[8] It is worth noting the concentration profile depicted in Figure 2.4 measures dopamine

for a singular point in ECS. Of relevance to the spatial and temporal limitations of existing experimental tools to probe brain neurotransmission, we implement our model for space averaged dopamine dynamics, as detailed below.

Dopamine Optical Probes in the Striatal ECS

Of relevance to fluorescent probes for measuring neurotransmitter concentrations in the ECS, our model captures spatial evolution of dopamine in the ECS, in addition to the temporally-relevant information obtained from FSCV. Fluorescent optical probes hold great promise for probing volume transmission dynamics in the ECS in a space and time resolved manner. First, optical probes can fit into the intricate porous and tortuous morphology of the ECS, allowing them proximate access to synaptic and extrasynaptic locations to record dynamic concentration behavior. Second, optical probes can be distributed over large volumes of the ECS to provides much needed spatial information. Here, we develop a model of a prototypical optical probe's fluorescence modulation in response to dynamic analyte behavior. Denoting the total number of dopamine binding probe sites as L, the free (dopamine unbound) sites as *, the dopamine-bound sites as DA* and free dopamine molecules as DA, we establish equilibrium conditions for reversible dopamine binding to an ensemble of optical probe sites in the ECS:

$$\begin{aligned} [L] &= [*] + [DA*] \\ DA + * &\Leftrightarrow DA* \end{aligned} \qquad 5$$

The first expression represents the dopamine active site balance and the second approximates that the dopamine adsorption process equilibrates on relatively short time scales compared to dopamine diffusion timescales in tissue. We define equilibrium constant, K_{eq} for the dopamine-sensor binding process as:

$$K_{eq} = \frac{[DA*]}{[DA][*]} \qquad 6$$

We next substitute the equilibrium constant into the site balance equation to derive an expression for the dopamine probe fluorescent response as follows:

$$L = [*] + K_{eq}[DA][*] \qquad 7$$

$$\frac{[DA*]}{L} = 1 - \frac{[*]}{L} = \frac{[DA]K_{eq}}{1 + [DA]K_{eq}} \qquad 8$$

We note that the increase in probe fluorescence intensity is directly proportional to bound active sites $\frac{[DA^*]}{L}$. Thus, the expression for change in intensity normalized against initial sensor fluorescence, $\frac{\Delta F}{F_0}$, can be represented as:

$$\frac{\Delta F}{F_0} = \alpha\left(\frac{([DA]Keq)^n}{1+([DA]Keq)^n}\right) \qquad 9$$

The additional fitting parameter, *n*, is introduced to account for dopamine binding cooperativity.

Temporal Resolution Is Determined by Probe Kinetics and Imaging Frame Rate

Optical technologies to measure neurotransmitters in the ECS must capture hundred millisecond-scale dopamine release and clearance, as shown by our simulations. Temporally resolved neurotransmitter measurements with FSCV need only account for temporal sampling rates, which are achieved with a high scan rate voltammogram. Conversely, for probes with fluorescence readouts, both temporal and spatial sampling rates will influence the measurement signal-to-noise, due to hardware limitations in fast sampling rates. Our simulations above set the physiologically relevant dopamine spatiotemporal dynamics in the striatum. Henceforth, we consider optical probe performance limitations that are imposed by imaging hardware and binding kinetics. During video-rate fluorescence imaging, substantive deviations from theoretical probe response profiles are likely to be encountered owing to the short time scales over which dopamine is released into and cleared from the ECS. Specifically, our model results show that dopamine dynamic behavior occurs on similar timescales as the exposure time used in conventional fluorescence microscopy (tens to hundreds of milliseconds). We must therefore account for possible temporal distortion imposed on probe response by imaging hardware. The probe $\Delta F/F_0$ observed using a video-rate fluorescence imaging is evaluated as:

$$\left(\frac{\Delta F}{F_0}\right)_{obs}(t) = \frac{1}{T_{\exp}}\int_{t}^{t+T_{\exp}}\left(\frac{\Delta F}{F_0}\right)_{theo}(t)\,dt \qquad 10$$

where $\left(\frac{\Delta F}{F_0}\right)_{obs}(t)$ is the observed probe response when imaging by fluorescence microscopy, and $\left(\frac{\Delta F}{F_0}\right)_{theo}(t)$ is the theoretical probe response function given by eqn. 9. T_{exp} is the camera exposure time and is inversely related to the nominal frame rate of imaging.

To optimize probe performance, we tuned several parameters in eqn. 9. Our goal is to determine which probe parameters will enable us to resolve dopamine dynamics of physiological relevance in the striatum. The equilibrium constant (K_{eq}), the proportionality factor (α), and the cooperativity parameter (*n*), are intrinsic to the probe and can be tuned to optimize probe performance. The parameter α weighs the fluorescent quantum yield

increase toward the imaging SNR. Higher α corresponds to stronger turn-on response ($\Delta F/F_0$) and improves SNR over the entire physiological dopamine concentration range. K_{eq} is a measure of the affinity between the probe and dopamine analyte. High K_{eq} (or low dissociation constant, K_d) improves response at low concentrations of dopamine, but also leads to quicker sensor saturation. On the other hand, low K_{eq} results in probes that are unresponsive to low concentrations of dopamine. Thus, to maximize the dynamic range of the dopamine probe for the range of experimentally relevant dopamine concentrations of 30 nM – 10 μM we sought to identify parameters that are amenable to capturing *in vivo* endogenous dopamine dynamics. First, we set a 5% $\Delta F/F_0$ lower-limit at the spatial boundary of the D_2-type receptor sphere of influence (17 μm), and this fixed $\alpha = 2$. We set the cooperativity factor at n =1 as representative for most validated optical probes. Fixing α and n, we vary K_{eq} over several orders of magnitude and determine $K_{eq} = 1\ (\mu M)^{-1}$ to be optimal for a fluorescent probe, which balances reversibility and sensitivity according to biologically imposed boundary conditions. To evaluate reversibility, we simulated probe response to two quantal release events located 0.2 seconds apart from the same terminal (Figure 2.5a). We define reversibility as the fall in probe intensity during clearance of the first quantal release, divided by rise in intensity in response to the first quantal release. The parameter $\alpha = 2$ sets maximum sensor response, and we define sensitivity as the measured peak $\Delta F/F_0$ divided by α. With these definitions, we varied K_{eq} over five orders of magnitude to develop the parameter maps shown in Figure 2.5b and Figures 2.6a, b. High K_{eq} values enhance sensitivity, enabling the probe to turn-on at low dopamine concentrations. However, high K_{eq} values cause the probe to saturate rapidly and adversely impact probe reversibility (Figures 2.5a, b). On the other hand, low K_{eq} values have very good reversibility but reduced sensitivity. At $K_{eq} = 1\ (\mu M)^{-1}$, we observe that the probe both responds instantaneously to quantal dopamine release, and also captures dopamine reuptake kinetics to accurately discern between two quantal release events 0.2 seconds apart. Thus, we identify $K_{eq} = 1\ (\mu M)^{-1}$ as optimal for imaging dopamine dynamics in the dorsal striatum, in which the fastest sequential quantal release events occur at least 0.2 seconds apart during tonic firing. [41]

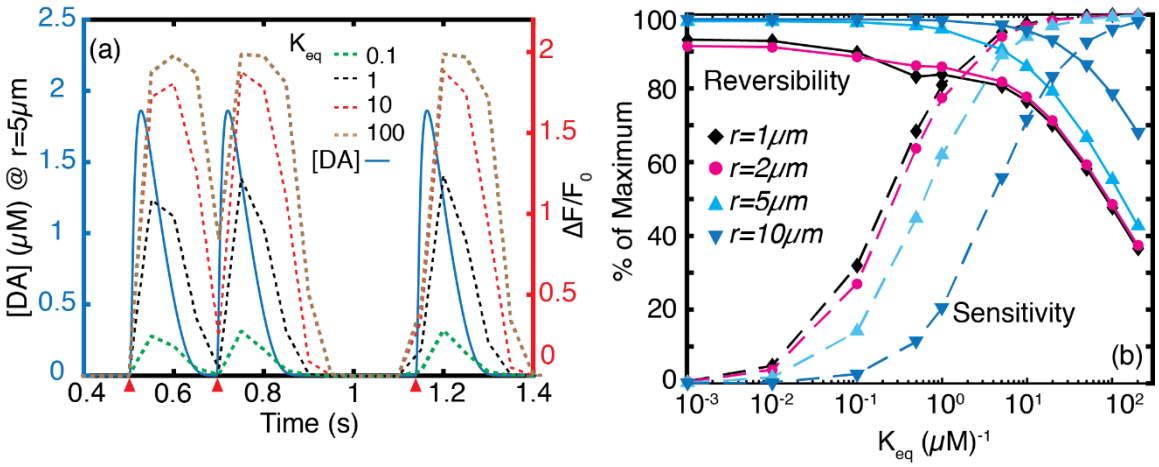

Figure 2.5 Effect of probe affinity parameter, K_{eq}, on performance. (**a**) Dynamics of three quantal release events (red wedges) imaged using probes for which K_{eq} varies over three orders of magnitude. The first two quantal releases are located 0.2 s apart. Plots of $\Delta F/F_0$ for a 20 Hz frame rate (eqn. 10) corresponding to each K_{eq} value are plotted in dash. At $K_{eq} = 100\ (\mu M)^{-1}$ the probe's affinity for dopamine is too strong, which adversely

affects reversibility. The second release event cannot be resolved. Peak $\Delta F/F_0$ values increase with increasing K_{eq}. At low K_{eq} values, the probe shows high reversibility but poor sensitivity. (**b**) Parameter space for reversibility and sensitivity at r = 1 µm, 2 µm, 5 µm and 10 µm from release site corresponding to a 20 Hz imaging frame rate. High dopamine concentrations proximal to the release site yield high sensor sensitivity. However, maintaining good reversibility suffers proximal to the release site.

The parameter space we developed to optimize spatiotemporal signal acquisition of dopamine optical probes with various K_{eq} values can now allow us to test how camera frame rates affect the sensor reversibility and sensitivity parameter space. As we show in Figure 2.6a, fast imaging frame rates are needed if the probe binds the dopamine analyte too strongly (large K_{eq}) to temporally resolve the two quanta released 0.2 s apart. Therefore, we conclude that an optimal frame rate is a necessary but not sufficient condition to resolve the temporal heterogeneities of dopamine dynamics in the striatum. The probe's chemical responsivity and adsorption/desorption kinetics, combined with the imaging hardware limitations, both contribute to the spatiotemporal profiles of dopamine evolution that can be captured. Corresponding to the 1 $(\mu M)^{-1}$ optimal K_{eq} we identified previously, a 20 Hz imaging rate offers the best reversibility (Figure 2.6a) and SNR (Figure 2.6c). When sequential release events faster than 0.2 s apart are considered, the reversibility curves shift towards sensors with lower K_{eq} in a manner similar to that observed for imaging close to the release site (Figure 2.5b). Therefore, recording of faster dynamic events demands probes with lower K_{eq}, and comes with an opportunity cost of low sensitivity (Figure 2.5b) and higher noise (Figure 2.6c, Figure 2.S4). The second chemical parameter of the probe, the turn-on response parameter α, has little effect on probe sensitivity and reversibility (Figure 2.6b), and which we set at $\alpha = 2$.

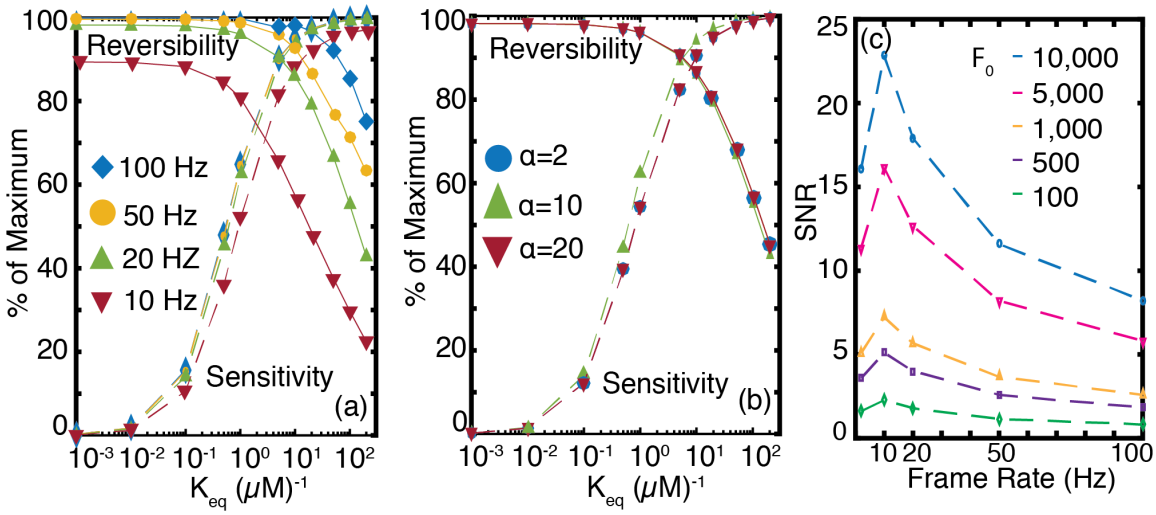

Figure 2.6 Sensor sensitivity, reversibility, and signal-to-noise ratio, probed for varying frame rates, chemistries, and baseline fluorescence. (**a**) Sensor parameter space for frame rates ranging from 10 Hz to 100 Hz with α = 2. Lower frame rates adversely impact reversibility and sensitivity but improve SNR (panel c). (**b**) Parameter space for sensor turn-on response, α, ranging from 2 to 20. The parameter space is largely insensitive to varying α. (**c**) SNR shows strong dependence on frame rate (abscissa) and baseline intensity (F_0, dashed traces) of the probe. As frame rate increases, SNR passes through a maximum at 10 Hz and monotonously decreases afterwards. The baseline fluorescence intensity F_0 is varied from 100 to 10,000 and corresponds to the 2 Hz frame rate, and units of F_0 are arbitrary. For definition of F_0, see equation 11.

Probe Fluorescence and Imaging Frame Rate Considerations for Optimizing Signal-to-Noise Ratio

The observed optical probe signal ($\Delta F/F_0$) takes into account the relationship between hardware (frame rate & instrument noise), and chemistry (fluorescent signal, sensitivity and reversibility parameters). During optical imaging of fast dynamic events, frame rates cannot be made arbitrarily faster because of their adverse impact on SNR. Here, we provide an analysis to include noise into the observed signal, $\Delta F/F_0$. To elucidate how hardware and sensor chemistry contribute to SNR, we consider the peak signal from a sensor with optimal kinetic parameters of α = 2 and K_{eq} = $1(\mu M)^{-1}$ responding to a single quantal release of dopamine at a radial distance of r = 5 μm. The mathematical derivation of noise for $\Delta F/F_0$ is provided in Methods in Appendix I. We consider the primary contribution of noise to the SNR to be Poisson noise (also known as shot noise) and do not take into account other sources of noise inherent to the imaging system such as read noise, which can be significant at high frame rates. Our analysis confirms that SNR is inversely related to frame rate and imaging frame rate should be carefully selected to optimize SNR in conjunction with the competing interest of maintaining high temporal resolution (Figure 2.6c). Furthermore, we identify the baseline fluorescence intensity (brightness) of the sensor, F_0, as an important parameter that influences SNR. SNR varies directly with F_0 and nearly inversely with frame rate, with a local maximum at 10 Hz (Figure 2.6c). The observed maximum at 10 Hz arises from the diffusion induced broadening of a quantal release (Figure 2.2b). For experiments wishing to optimize the temporal resolution of multiple dopamine firing events, choosing probes with strong baseline fluorescence will enable doing so via higher frame rates that achieve a decent fluorescent SNR.

The strong dependence of SNR on F_0 requires a closer examination. F_0 depends on variables that are intrinsic to the fluorophore and to the imaging system as follows:

$$F_0 \propto \left(\frac{1}{\Gamma}\right)(NI\sigma)(\eta\phi) \qquad 11$$

where Γ represents frame rate, N, the fluorophore number density, I, the excitation light source intensity and σ, the absorption cross-section of the fluorophore. The last two terms in equation 11 represent the quantum yield of the fluorophore (η) and the photon collection efficiency of the imaging system (ϕ). The direct dependence of SNR on F_0 arises from noise filtering effects that arise from counting large numbers of photons, which inherently reduces Poisson noise. Thus, SNR optimization can be accomplished by tuning the fluorophore's photophysical and chemical properties such as absorption cross-section, quantum yield, and analyte specificity. Two saturation regimes are worth noting: a neurotransmitter analyte saturation regime and a photon saturation regime. For the neurotransmitter concentration regime: the fluorophore number density, N, contributes to improved SNR only as long as the neurotransmitter analyte concentration does not become limiting. If the number of active probe binding sites exceeds available analyte molecules, the relationship between N and SNR will deviate from that shown in Figure 2.6c. For the photon limiting regime: SNR will increase proportional to excitation intensity I, so long as photobleaching or fluorophore saturation

does not dominate the imaging process. These latter effects demonstrate the importance of choosing optimal fluorophore excitation sources.

We implemented the optical probe's performance evaluation paradigm we developed previously to the dopamine nanosensor described by Kruss et al. that has a K_{eq} value of 2.31 $(\mu M)^{-1}$ and α of 0.55.[46] We probed dopamine concentrations at several distances from a terminal within the D_1-type and D_2-type receptor spheres of influence. Consistent with our results above, the spatiotemporal dependence of dopamine concentration evolution and corresponding nanosensor response requires a 20 Hz frame rate to discriminate between two sequential release events occurring 0.2 seconds apart (Figure 2.7a). When camera exposure times are incorporated into our model, we indeed find that longer exposure times decrease the nanosensor fluorescence response recorded by the camera. As a result, the recorded spatial and temporal responsivity of the dopamine nanosensor underestimates the physiological dopamine concentration and misses the true temporal release by overestimating the peak dopamine release time (Figure 2.7a). We compare the discrepancy between true nanosensor response and imaged nanosensor response for 2, 4, 10, and 20 Hz frame rates. The ability of a nanosensor to capture single terminal quantal release is compromised at frame rates below 2 Hz, where observed nanosensor response is only 20% of the predicted peak response, and could introduce a time-delay of up to 0.5 s. Conversely, when imaging with a 20 Hz frame rate, 95% of the nanosensor fluorescence response is captured, and time-delay of no more than 50 ms is introduced between the quantal release event and the nanosensor response. Considering that there is diffusion induced temporal distortion of 30 ms at r = 5μm (Figure 2.S1), this temporal delay at 20 Hz imaging becomes negligible. For the dual quantal events located 0.2 s apart corresponding to tonic activity, a 20 Hz frame rate can indeed identify the two events (Figure 2.7a, b, c). Conversely, both a 2 Hz and 4 Hz frame rate enables the nanosensor to record a spike in local dopamine concentration, but cannot discern that this spike is a result of two distinct quantal release events (Figure 2.7a). However, because the peak turn-on response of the sensor is only α=0.55, the farthest sphere of detection, set by a $\Delta F/F_0$ of at least 5%, is 15 μm (Figure 2.7c).

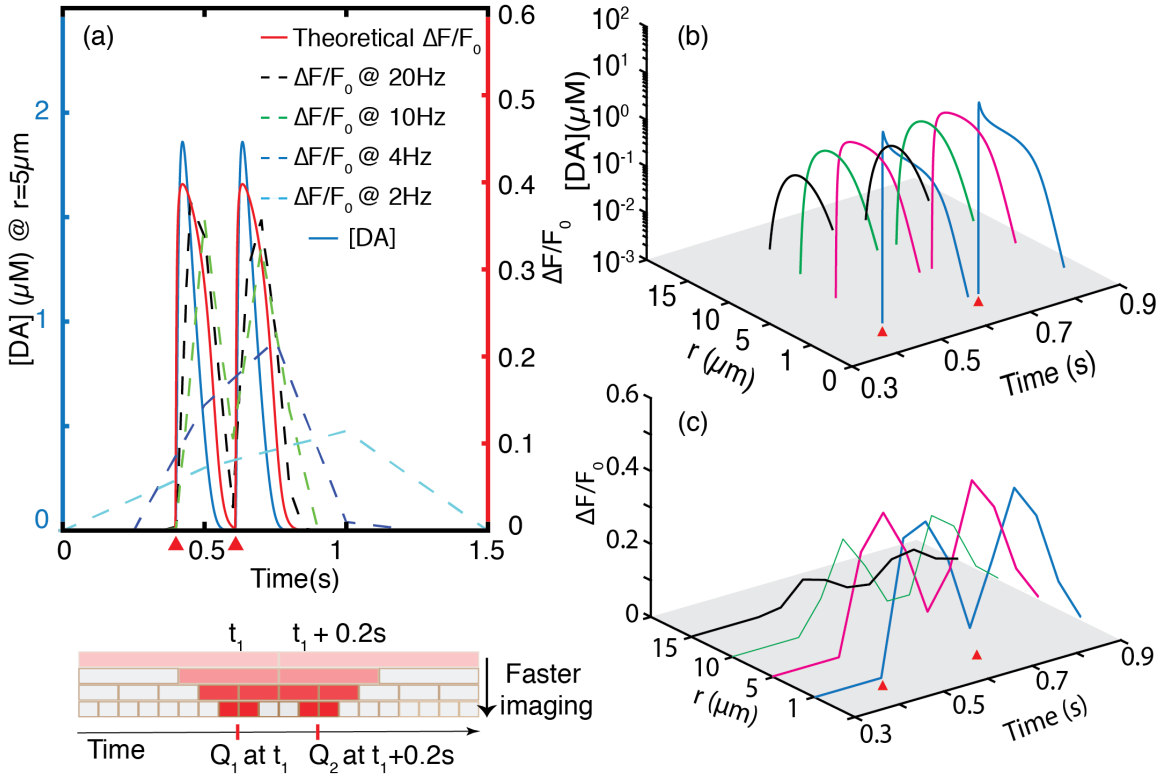

Figure 2.7 Temporal resolution of single and dual quantal dopamine release events. (**a**) Faster imaging frame rates enable resolution of quantal release events. As imaging frame rate increases, the observed response to dopamine more accurately captures the theoretical probe response. Red wedge indicates time of quantal release. Bottom panel: schematic shows how faster imaging more precisely localizes temporal position of a quantal release. Color gradient is to scale, showing the $\Delta F/F_0$ relative to the theoretically expected at each frame rate. (**b**) Dopamine concentration evolution of a dual quantal release of dopamine separated in time. Discrimination between two quantal releases improves as one moves away from release site. Red wedges show times of quantal release positioned 0.2 s apart. (**c**) Probe response to the dual quantal release presented in (a) and (b) imaged with a 20 Hz frame rate. Evolution of the two releases can be imaged up to 15 μm away from the release site with $\Delta F/F_0$ of ≥ 5%.

The preceding analyses show that diffusion of dopamine out of the synaptic cleft and into the brain ECS can be detected by optical probes located up to 17 μm away from the terminal with $\Delta F/F_0$ of 5% or more when sensor kinetics and imaging frame rates are optimally selected. Furthermore, we exemplify how probes can be implemented to image temporal heterogeneities of dopamine dynamics, provided imaging hardware with sufficiently high frame rates. Specifically, frame rates of 20 Hz resolve multiple quantal releases that occur during tonic firing. In general, for optimal K_{eq} values, quantal releases located x ms apart require camera exposure times of less than $x/2$ ms to be resolved. However, imaging frame rates cannot be increased infinitely to fully recapitulate the temporal profile of dopamine release and an optimization needs to be carried out in consideration of SNR. While improving SNR, slower frame rates decrease sensor response ($\Delta F/F_0$) and introduce significant temporal distortion on the measured dopamine response profile.

Optimal Probe Kinetic and Imaging Parameters can Record Behavior-Relevant Dopamine Dynamics for *In Vivo* Applications

The readout from optical probes located in the striatal ESC will report on the space-averaged dopamine dynamics resulting from terminals in the volume surrounding the probe. In practice, we wish to sample the cumulative behavior of dopamine over a region of interest in the ECS. Our model fluorescent single-walled carbon nanotube sensors, with a 250 nm length and 1 nm width, diffuse through the ECS as rigid rods, and sample ECS subdomains on a short characteristic time scale of 200 ms.[47] As such, the ensemble fluorescence modulation of optical nanosensors and other related fluorescent probes reflects average dopamine concentration. We simulate the ensemble fluorescence modulation of fluorescent indicators in the ECS by averaging dopamine concentration over the simulation volume as described in Methods in Appendix I.

The volume averaged dopamine dynamics corresponding to 100 terminals firing phasically is shown in Figure 2.8a, b and Figure 2.S6. We define the phasic firing regime over a 2 second simulation with the physiologically relevant spike train defined in Figure 2.4: A 4 Hz tonic firing rate for t = 0 to t = 0.4 s, a 20 Hz burst firing regime for t= 0.4 s to t = 0.7 s, a 0.5 s pause (0 Hz) until t = 1.2 s, and a 4 Hz tonic firing regime for 1.2 s to 2.0 s. Our simulation shows that when neurons fire asynchronously (Figure 2.8b) tonic dopamine concentrations in the ECS fluctuate between 10 nM and 100 nM (Figure 2.8a, blue regions). Conversely, synchronous firing of terminals (Figure 2.S6b) gives rise to transient dopamine concentrations in the ECS that range from 200 nM to 300 nM, with no basal levels between the peaks (Figure 2.S6a, blue regions). The average tonic dopamine concentration in the striatal ECS obtained with our model is 50 nM (Figure 2.S5), in agreement with results from prior computational studies[30] and experimental measurements.[48,49] This confirms that basal striatal dopamine is mediated by random, uncorrelated firing from dopaminergic terminals belonging to different neurons as opposed to correlated tonic firing. The volume averaging result is consistent with our simulations of many-terminal behavior presented in the previous section (Figure 2.4), validates our volume-averaging model, and corroborates previous experimental hypotheses about the nature of basal dopamine in the striatum originating from asynchronously firing neurons.

We next compute the ensemble dopamine probe response profile for the theoretical versus practical cases of video-rate fluorescence imaging. We implement our results for a 20 Hz imaging frame rate identified previously as optimal for capturing striatal dopamine dynamics with optimal parameters K_{eq} = 1 (μM)$^{-1}$, $\alpha = 2$. During a firing burst that lasts 0.3 seconds, volume-averaged concentration rises to ~ 1 μM for both synchronous and asynchronous firing. These results represent space-averaged concentrations; locally, concentrations are heterogeneous and can be higher than the volumetric averages computed here (Figure 2.4a, b). Corroborating our prior results, imaging at 20 Hz, one can capture transient peaks during tonic firing in addition to the global concentration peak caused by a burst firing (Figure 2.8a, Figure 2.S6). Furthermore, all behaviorally relevant firing regimes can be resolved, including the 0.5 s pause following the burst firing. At an imaging frame rate of 2 Hz, one can only resolve the concentration increase caused by burst firing; neither transient activity during tonic firing nor the pause following burst firing can be resolved

(Figure 2.8a). High affinity probes saturate at tonic dopamine levels (Figure 2.8c) whereas sensors with low dopamine affinity result in low $\Delta F/F_0$ (Figure 2.8d).

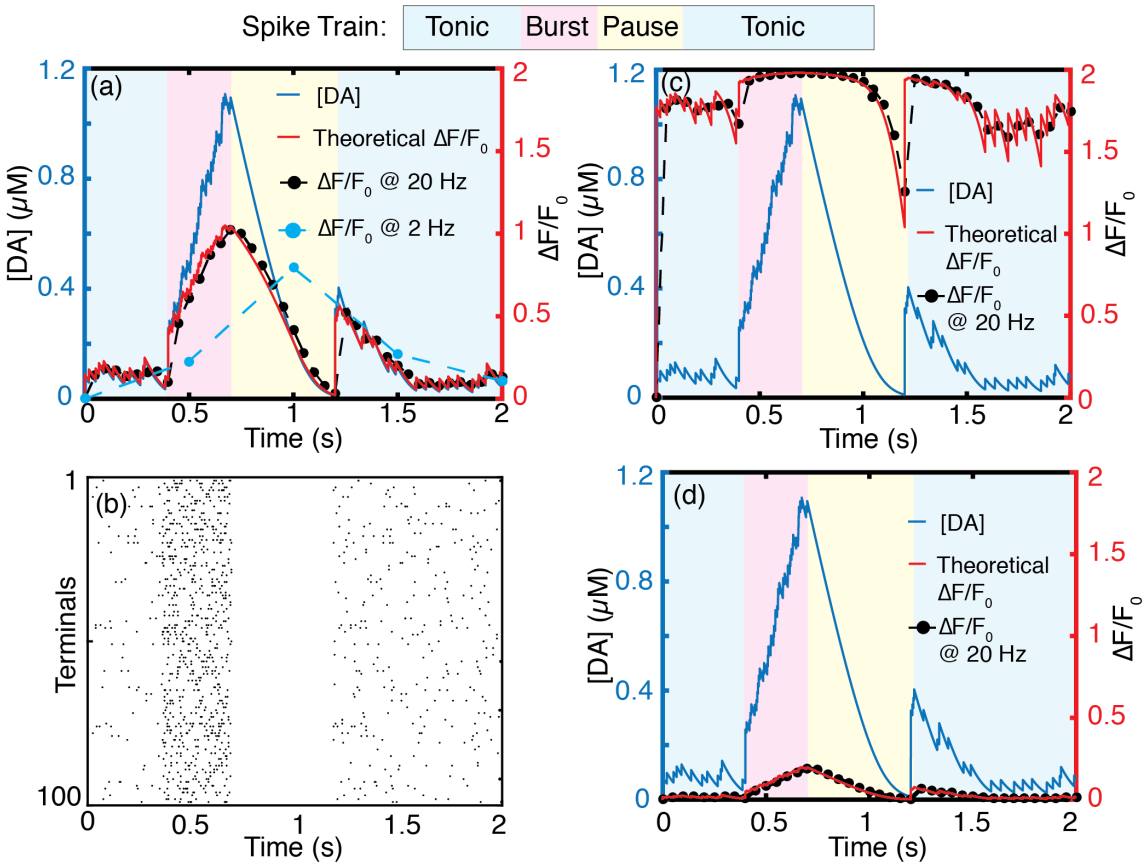

Figure 2.8 Volume averaged concentration profiles of 100 phasically firing dopamine terminals. (**a**) Dopamine concentration profile in which terminals fire asynchronously and corresponding sensor response of theoretical, 20 Hz and 2 Hz video-rate frame rates with K_{eq}=*1 μM*$^{-1}$ and α = 2. (**b**) Raster plot of asynchronous firing activity corresponding to (a). (**c**) Same asynchronous activity imaged with a sensor with K_{eq} = *100 μM*$^{-1}$. The high probe-analyte affinity results in sensor saturation at low (tonic) levels of dopamine (**d**) Same asynchronous activity imaged with a sensor with K_{eq} = *0.1 μM*$^{-1}$. The low probe-analyte affinity results in decreased sensitivity, with an exemplary burst firing event resulting in only 10% of the probe's peak $\Delta F/F_0$.

2.3 Conclusion

The ECS constitutes an interconnected, porous and tortuous milieu that pervades neural tissue and serves as the medium through which neurons communicate with each other by way of chemical signaling. Our work quantifies the spatial and temporal nature of this chemical signal by using the dorsal striatum as a model system and identifies optimal imaging and probe kinetic parameters necessary to record chemical signaling in real time *in vivo*. Dopamine chemical signaling involves significant spillover of molecules from the synaptic cleft into the ECS, and a complex dynamic behavior arises as a consequence of quantal release and simultaneous diffusion and reuptake processes. This work elucidates this dynamics by use of a rigorous, non-linear stochastic simulation, validated against existing experimental and computational literature. We show that the overflow of dopamine can be detected with optical probes placed in the ECS when proper imagining and kinetic parameters are chosen. A parameter space encompassing kinetics and imaging frame rate is developed. Our work can be used to guide new probe development or to optimize those already developed. We use a generic receptor-ligand probe kinetics that makes the results of our work broadly applicable to neurochemical imaging in the brain ECS. Furthermore, the model of the striatum developed here can be easily adapted to explore dynamics in other dopaminergic systems, such as the pre-frontal cortex and the nucleus accumbens, or to study analogous volume transmission phenomena of monoamines such as norepinephrine and serotonin. The simulation is modular and can be efficiently adapted to investigate broader variety phenomena that involve neurotransmitter dynamics such as pharmacokinetics of therapeutic agents and brain disease states.

2.4 Appendix I

Materials and Methods

Dopamine release sites and probability of release

Our model is implemented to study spatiotemporal profiles of neurotransmitter release from synapses. As such, our model is implemented with parameters and boundary conditions relevant to experimentally validated neuronal processes. Central synapses of the nervous system such as those found in the striatum contain a single release site, as comprehensively reviewed in Stevens et al.[33] During an action potential, a single quantal release of dopamine occurs with a certain probability *p*, at each terminal (Figure 2.1b). Dreyer et al. calculate probability of 6% based on studies of neurotransmitter release using FFNs[19,20] and the dopamine content of striatal tissue. As such, our model sets the probability of dopamine release to 6% per action potential per terminal, consistent with experimental observations, and that this release probability remains constant for the simulation time course.

Simulation of release, diffusion and reuptake

Our simulation of dopamine concentration in the ECS invokes the equation of change for species conservation surrounding a dopaminergic terminal

$$\frac{\partial c(r,t)}{\partial t} = D\nabla^2 c(r,t) + Q(r,t) - U(r,t) \qquad 1$$

We solve the governing equation individually for each dopamine terminal, and superimpose temporal solutions of the governing equation to determine dopamine dynamics at any location within the simulation volume. Thus, the temporal change in dopamine concentration at any point in the ECS is the sum of the dopamine dynamics contributed by all terminals in the point of interest vicinity. We note that the error introduced by summing the non-linear reuptake term is negligible: dopamine re-uptake approximates linear behavior at sites distant from a release point, where the spatial summation occurs. For our simulation of dopamine release, diffusion, and reuptake, we use radial steps, *dr,* of 0.2 μm and time steps, *dt,* of 0.02 ms, which yield stable solutions over a wide range of biological parameters.

Discretization scheme and boundary conditions

The model implements finite differences to solve the governing equation (eqn. 1). We take advantage of dopamine diffusion symmetry and isotropy to reduce the problem into 1D in spherical coordinates such that the distance from the release site, *r,* is the only spatial domain in the model. Symmetry at the site of a release site serves as a boundary condition for our numerical solution, and is used to calculate dopamine concentration at the center of the simulation volume. We provide details of the discretization scheme below.

The left-hand side of the governing equation 1 can be written in difference form as:

$$\frac{\partial c}{\partial t} = \frac{c(n, j+1) - c(n, j)}{\Delta t} \qquad 12$$

where indices *n* and *j* represent discrete steps in space and time, respectively.

To cast the right-hand side of equation 1 in difference form, we first expand the Laplacian:

$$\nabla^2 c = \frac{1}{r^2}\frac{\partial}{\partial r}\left(r^2 \frac{\partial c}{\partial r}\right) = \frac{\partial^2 c}{\partial r^2} + \frac{2}{r}\frac{\partial c}{\partial r} \qquad 13$$

and discretize the first and second spatial derivatives as follows:

$$\frac{\partial^2 c}{\partial r^2} = \frac{c(n+1, j) - 2c(n, j) + c(n-1, j)}{(\Delta r)^2} \qquad 14$$

$$\frac{\partial c}{\partial r} = \frac{c(n+1,j) - c(n-1,j)}{2\Delta r} \qquad 15$$

Using these difference equations and leaving the release and uptake terms as Q and U respectively, we can write an explicit equation for *c(n, j+1)* as (eqn.16):

$$c(n,j+1) = c(n,j)\left(1 - \frac{2D\Delta t}{(\Delta r)^2}\right) + \frac{D\Delta t}{(\Delta r)^2}\left(c(n+1,j)\left(1 + \frac{1}{n-1}\right) + c(n-1,j)\left(1 - \frac{1}{n-1}\right)\right) + (Q-U)\Delta t$$

where *r=(n-1)* Δr *.*

The uptake term U is written explicitly in *c(n,j)* space as a Michaelis-Menten rate expression and the quantal release term (Q) is handled as described previously:

$$U(n,j+1) = \frac{r_{\max} c(n,j)}{\alpha(c(n,j) + K_m)} \qquad 17$$

$$Q(n,j+1) = \frac{(Q_0 / N_A)}{\alpha[2\pi(dr)^2]^{3/2}}\left(\frac{e^{-(n-1)^2}}{1.386}\right)\psi(p)\delta(t_{j+1} - t_f) \qquad 18$$

We discretize the symmetry boundary condition as follows. First we note that the governing equation as r → 0 becomes:

$$\frac{\partial c}{\partial t} = 3\left(\frac{\partial^2 c}{\partial r^2}\right) + Q(r,t) - U(r,t) \qquad 19$$

where we used L'Hopital's rule to evaluate the limit. The spatial and temporal derivatives of equation 19 are discretized using equations 12 and 14 and then evaluated for n=1 (center), yielding:

$$c(1,j+1) = c(1,j)\left(1 - \frac{6D\Delta t}{(\Delta r)^2}\right) + c(2,j)\left(\frac{6D\Delta t}{(\Delta r)^2}\right) \qquad 20$$

Simulation algorithm

At each simulation time step, the algorithm determines whether an action potential will invade a terminal based on a Poisson probability distribution with mean firing rate *F*. If there is a firing event, a quantal release of dopamine will occur based on a release probability, *p*, by toggling the binary variable $\psi(p)$ between 1 (release) and 0 (no release). If a quantal release of dopamine occurs, dopamine concentration in the volume immediately surrounding the terminal (*r=0*) will be incremented by an amount in equation 3. Increment

at subsequent volume elements are scaled as $e^{-(n-1)^2}$, a factor that follows directly from a Gaussian probability density function. Once dopamine reuptake is determined, dopamine concentration at the location in space is decreased by an amount equal to the computed reuptake term. Because the discretized governing equation (eqn. 16) fails for *r=0 (n=1),* where it becomes a singularity, we set Neumann's symmetry principle at r=0 as a boundary condition and use it to compute concentration at the center (eqn. 20). We construct our simulation volume such that the effects of dopamine depletion at any point in space will result from dopamine reuptake by DATs within the simulation volume. Thus, we implement the Dirichlet boundary condition to enable modeling of dopamine reuptake effects at any distance from the center of the release site. Determining the exact location of this boundary requires solving the governing equation first, with a free boundary condition. We therefore set dopamine concentration to 0 when dopamine reuptake is higher than the available dopamine concentration at any given location from release point *r=0* as described by Berger et al. for the diffusion and uptake of oxygen in tissue.[50] The simulation is implemented using MATLAB 2016a.

Volume-averaged dopamine dynamics

The dynamics from many terminals averaged over the volume encompassing the terminals is computed as follows:

$$c(j+1) = c(j) + \sum_{n=1}^{Nt}\left(\frac{(Q_0 / N_A)}{\alpha V_{sim}}\psi(p)\delta(t_{j+1} - t_f)\right) - \frac{r_{\max} c(j)\Delta t}{c(j) + K_m} \qquad 21$$

where c(j+1) is the volume averaged concentration of dopamine at time t_{j+1}, c(j) is concentration at time t_j, and j is the time index of the simulation. N_t is the number of terminals in the simulation volume V_{sim} (1000 μm^3). Terminals depolarize at designated times t_f, where t_f is the same for all terminals during synchronous firing and different for each terminal during asynchronous firing. The firing frequency sets the number of action potentials during a given simulation period. A Poisson distribution with a known mean firing rate sets the distribution of action potentials over the simulation time. Synchrony in firing activity is a reflection of the underlying functional connectivity of the ensemble. Synchronous firing (depolarization), however, does not mean all terminals release dopamine simultaneously; release of dopamine at each terminal is probabilistic and independent as per prior experimental literature, and thus set to 6% in our simulations. Note also that $N_t = V_{sim} * \rho_t$ where ρ_t is the density of dopamine terminals (Table 1) and Δt is the simulation time step ($\Delta t = t_{j+1} - t_j$). The volume averaging as defined in equation 21 is valid only for large enough ensembles where diffusive flux out of the volume can be neglected. This is true if the volume is larger than the length scale of dopamine diffusion from a terminal. For small ensemble volume averaging, diffusive flux out of the volume needs to be taken into account because the length scale of the volume is smaller than the diffusion length scale of dopamine (Figure 2.S5).

Signal-to-noise ratio

The noise on the signal $\Delta F/F_0$ is related to the noise on F and F_0. Using uncertainty propagation rules, we have:

$$\xi = \left(\frac{F + F_0}{F_0^2} + \frac{(\Delta F)^2}{F_0^3} \right)^{1/2} \qquad 22$$

where ξ is the noise on our signal $\Delta F/F_0$. We use noise of $\sqrt{F}$ and $\sqrt{F_0}$ on F and F_0 respectively, for Poisson limited imaging.

2.5 Appendix II

Supporting Information

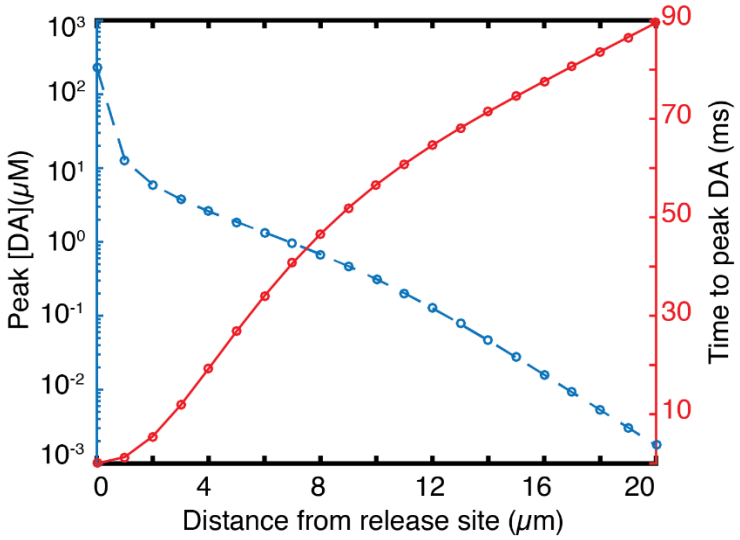

Figure 2.S1. Peak dopamine concentration as a function of distance from release site following a single quantal release. Our simulation shows a peak dopamine concentration of 226μM at r = 0 μm (inside the synaptic cleft), which dissipates instantaneously as it expands out into the ECS. A peak dopamine concentration of 1 nM is observed at a distance of 20 μm from the release site with a diffusion-induced time delay of 90 ms from time of release.

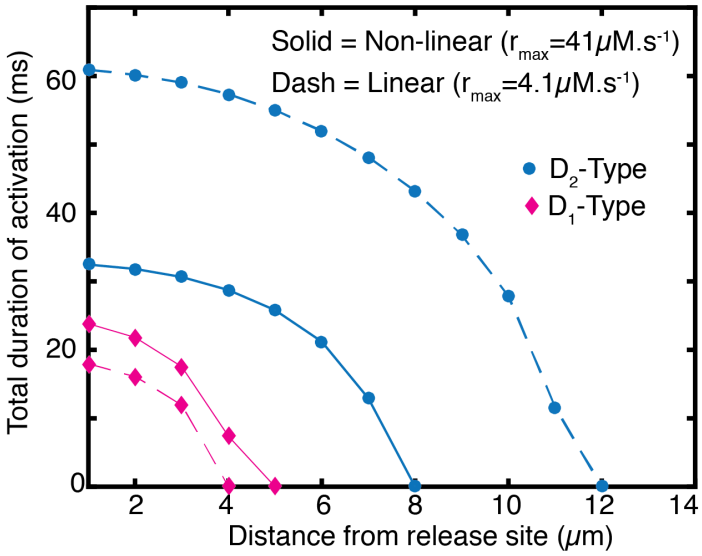

Figure 2.S2. Comparison of non-linear dopamine reuptake versus linear uptake model. Non-linear dopamine reuptake with r_{max} at 41 µM.s^{-1} compared to linear uptake with r_{max} at 4.1 µM.s^{-1}. Both cases are run with an equal K_m of 0.21 µM. D_1 –type receptor activation shows similar behavior for both non-linear (r_{max} = 41µM.s-1) and linear (r_{max} = 4.1µM.s-1) reuptake. Comparison D_2 –type receptor activation shows similar behavior. For both receptor types, linear uptake underestimates the extent of receptor activation when compared to non-linear reuptake model by an order of magnitude.

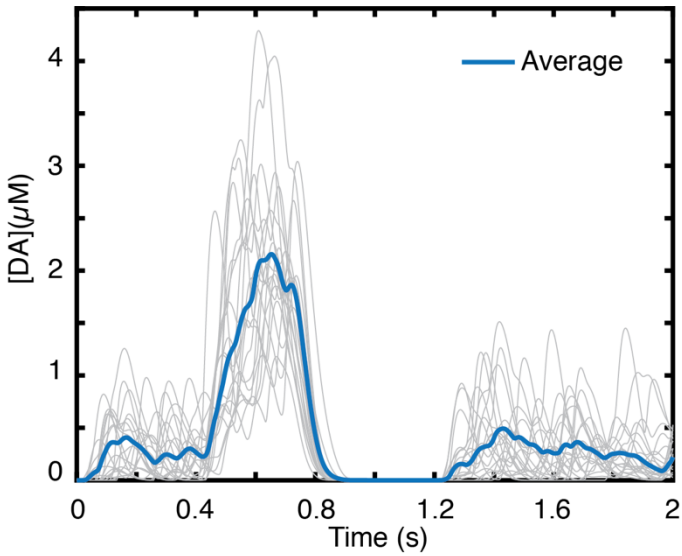

Figure 2.S3. Averaging of multiple simulation runs for asynchronous terminal firing. Average (bold blue trace) of N=20 simulation runs (light gray traces) of 100 asynchronously firing terminals. The firing regime is as defined in Figure 2.4 of the main manuscript and is omitted here for clarity.

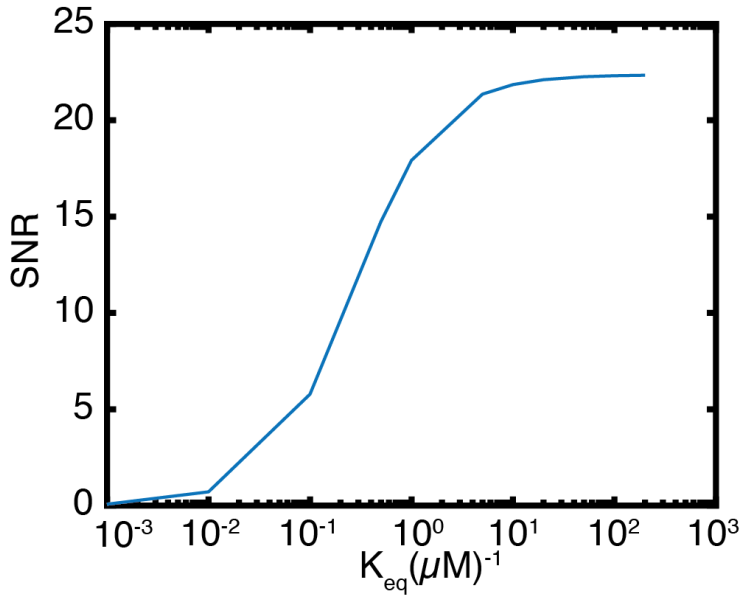

Figure 2.S4. Dependence of SNR on the sensor parameter K_{eq}. High K_{eq} sensors have stronger turn-on response but poor reversibility. Imaging of faster dynamic processes, where temporal resolution is desired, requires fast reversible sensors with low K_{eq} at a cost of lower SNR. Figure is developed for F_0 = 10,000 and imaging frame rate of 20 Hz.

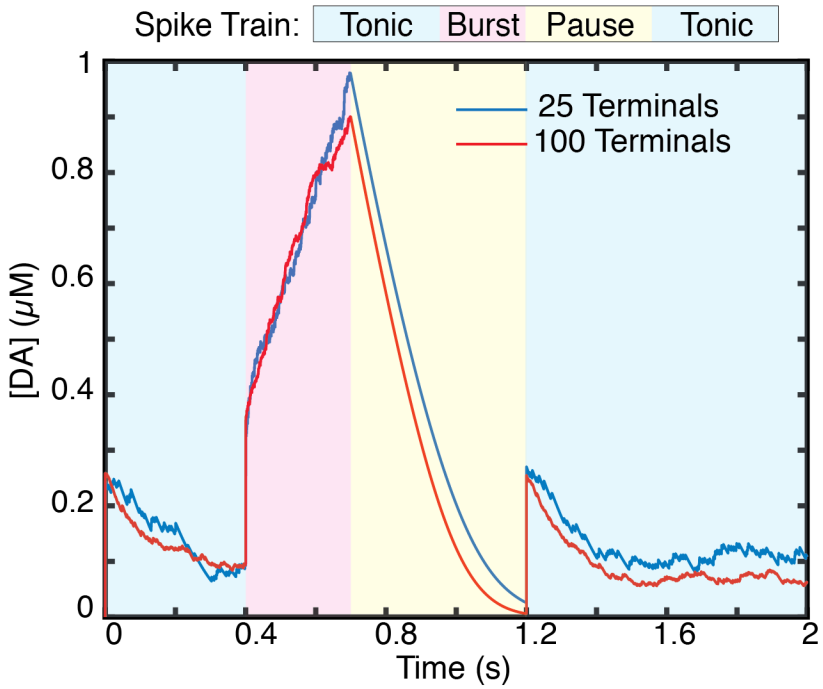

Figure 2.S5. Volume-averaged behavior of 25 terminals vs. 100 terminals firing asynchronously. The result shows an average from N = 20 simulation runs for each 25- (blue) or 100- (red) terminal cluster. Volume-averaged dynamics show behavior that is largely independent of cluster size for behavior-relevant firing regimes of burst firing and pause in firing. At smaller cluster sizes, the diffusive flux of dopamine out of the averaging volume becomes important and can no longer be ignored, resulting in slightly higher concentrations.

For the 100-terminal cluster where release from a terminal does not escape the averaging volume size, accurate tonic and burst concentration levels can be estimated. Tonic dopamine level approaches 50 nM.

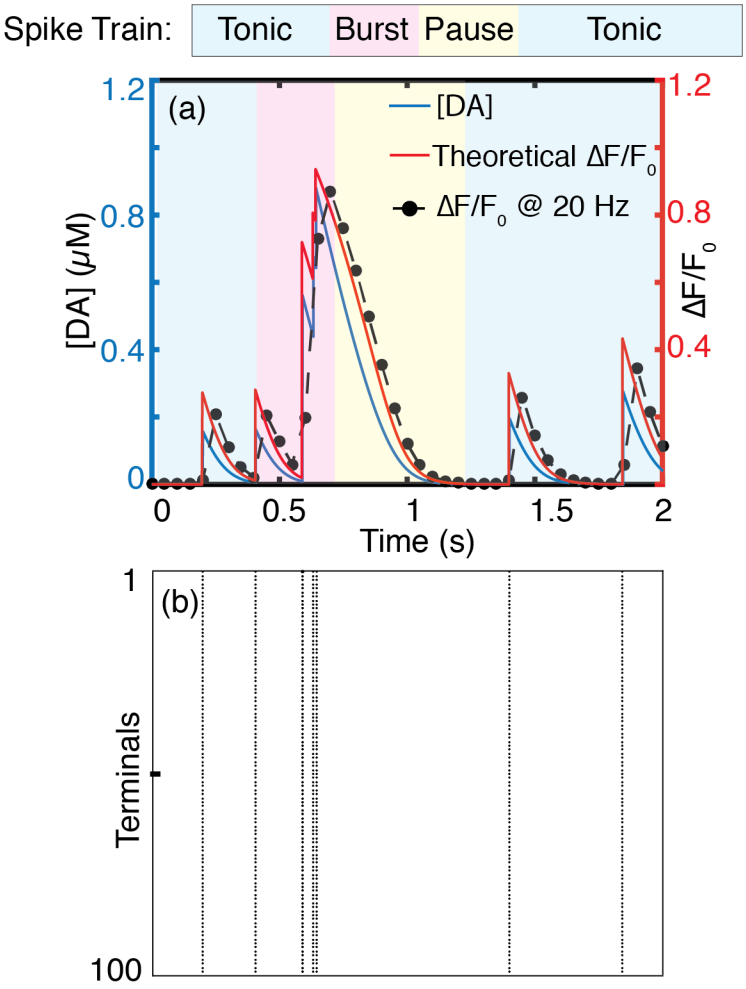

Figure 2.S6. Volume-averaged concentration profiles of 100 phasically firing dopamine terminals. (a) Dopamine concentration profile in which terminals fire synchronously and corresponding sensor response of theoretical and 20 Hz video-rate frame rates with K_{eq}=1 μM^{-1} and α = 2. (b) raster plot of synchronous firing activity corresponding to (a).

Chapter 3

Turn-On Fluorescence Modulation of ssDNA-Functionalized Carbon Nanotubes by Catecholamine Neuromodulators

Portions of this chapter are reproduced with permission from Ref 51.[51] *Copyright 2018. American Chemical Society.*

Non-covalent interactions between single-stranded DNA (ssDNA) oligonucleotides and single wall carbon nanotubes (SWCNTs) have provided a unique class of tunable chemistries for a variety of applications, notably the use of these conjugate materials as optical probes for neuromodulators. However, mechanistic insight into both the photophysical and intermolecular phenomena underlying their utility is lacking, resulting in obligate heuristic approaches for producing ssDNA-SWCNT based nanosensor technologies. In this work, we present an ultrasensitive "turn-on" nanosensor for the catecholamine dopamine and norepinephrine with strong relative change in fluorescence intensity ($\Delta F/F_0$) of up to 35-fold, a signal favorable for *in vivo* neuroimaging. The nanosensor is synthesized from the spontaneous self-assembly of $(GT)_6$ ssDNA rings on SWCNTs. The fluorescence modulation of the ssDNA-SWCNT hybrid structure is shown to exhibit remarkable sensitivity to the ssDNA sequence chemistry, length, and surface density, providing a set of easily accessible experimental parameters with which to tune nanosensor dynamic range and strength of fluorescence turn-on. In a subsequent chapter, we rationalize our experimental observations through molecular dynamics simulations.

3.1 Introduction

Single wall carbon nanotubes exhibit advantageous electronic and photophysical properties that make them attractive for a diverse field of applications in electronics[52–56], sensing[57–60], imaging[61–63,47], and molecular transport[64–66]. SWCNT fluorescence originates from radiative recombination of one-dimensional confined excitons, exhibits exceptional photostability, and is remarkably sensitive to the nanotube geometric and electronic structure as well as the local chemical environment.[67–69] The sensitivity of SWCNT fluorescence to the local chemical environment has been leveraged for the synthesis of optical probes in which polymer functionalizations serve a dual purpose of forming stable SWCNT colloidal suspensions and conferring selective molecular recognition capabilities.[60,70] Several SWCNT-based probes with selective analyte mediated modulations in optical band gaps or in fluorescence quantum yield with $\Delta F/F0$ on the order of 9% to 80% have been reported .[46,60,71–74]

For *in vivo* molecular sensing applications, synthesizing suitable elements capable of transducing *in vivo* signals constitutes a formidable challenge, requiring maximal changes in fluorescence intensity from baseline ($\Delta F/F_0$). The spatiotemporal sensitivity required for *in vivo* utility – in particular for fast processes such as chemical neurotransmission in the brain – must account not just for analyte concentration levels, but also for the spatial spread of the signal (micrometers) as well as its temporal duration (milliseconds).[5,16] An ideal probe

therefore must satisfy several requirements, including high sensitivity, molecular selectivity, and optimal binding kinetics, among others. The versatility and ease with which SWCNTs can be functionalized by a wide range of polymers provides a great opportunity for a rational design of synthetic optical probes capable of detecting biomolecules such as neurotransmitters in their native environment. However, despite proliferating reports of SWCNT-polymer conjugates for biomolecule sensing, a robust pathway for translating SWCNT nanosensors into *in vivo* sensing applications remains elusive. We identify two specific limitations in the development of SWCNT based optical probes – lack of a rational design principle and dearth of *in vivo* implementation – and posit that a lack in fundamental understanding of how SWCNT-polymer hybrid nanomaterials interact with and subsequently undergo selective fluorescence modulation by molecular targets underlies these limitations. This knowledge gap is evident in the status quo for nanosensor discovery, which relies on low-throughput screening techniques, and an inability to tune nanosensor performance once a discovery has been made.

In this work, we report a high turn-on nanosensor for neuromodulators dopamine and norepinephrine. We demonstrate that we can tune SWCNT baseline fluorescence intensities to increase nanosensor analyte sensitivity for key neurotransmitters dopamine and norepinephrine by over an order of magnitude compared to a previously reported catecholamine nanosensor.[46] Sequence-specific 'short' ssDNA polymers produced strongly quenched SWCNT baseline fluorescence and a robust turn-on response to neuromodulators dopamine and norepinephrine. We find this phenomenon to be sensitive to the base sequence chemistry, polymer contour length, nanotube bandgap, and polymer surface density. A sodium cholate (SC)-based corona exchange assay suggested the presence of specific molecular recognition sites in the ssDNA-SWCNT corona which stabilize the surface adsorbed polymer when occupied by dopamine and norepinephrine analytes. In a subsequent chapter, we will introduce computational methodologies to help rationalize key experimental observations.

3.2 Results and Discussion

Strong Fluorescent "Turn-on" Neuromodulator Nanosensors

Prior work has shown the fluorescence intensity of $(GT)_{15}$-SWCNT increases by 60% ($\Delta F/F_0 = 0.6$) upon exposure to 100 μM of dopamine, which translates to $\Delta F/F_0 = 0.3$ at maximal physiological dopamine concentrations that follow burst neuronal firing events (~1 μM).[5,30,46] Here, we denote the baseline (pre-analyte) fluorescence as F_0 and the post-analyte fluorescence as F and define $\Delta F/F_0 = (F-F_0)/F_0$. Motivated by the goal of producing an *in vivo* compatible neuromodulator nanosensor for a broader dynamic range of physiological relevance, we synthesized a $(GT)_N$ based ssDNA-SWCNT library for N = 4, 6, 7, 8, 12, 15, 19, 22, 26, and 30 with a previously described protocol.[75] Near infrared fluorescence and absorption spectroscopy confirm that all sequences from N = 4 to N = 30 produced stable DNA-SWCNT suspensions, as evidenced by sharply defined spectral line shapes corresponding to known SWCNT electronic transitions (Figure 3.1a, 3.1b, Figure 3.S1, Figure 3.S2). We then measured each $(GT)_N$-SWCNT nanosensor response to 100 μM dopamine. Consistent with previous results, dopamine addition increases SWCNT fluorescence for all sequences (Figure 3.1). However, there exists a strong polymer length-dependent trend in

nanosensor response, for which the previously reported $(GT)_{15}$-SWCNT nanosensor represents an apparent minimum ($\Delta F/F_0 = 0.9$), and $(GT)_6$-SWCNT a maximum ($\Delta F/F_0 = 23$) (Figure 3.1a, 3.1b, 3.1e). 'Short' $(GT)_N$ polymers (N = 4, 6, 7, 8) yield $\Delta F/F_0$ = 14, 23, 17, and 10 in response to 100 μM dopamine, respectively, for the (9,4) SWCNT chirality. Conversely, 'long' $(GT)_N$ polymers (N = 12, 15, 19, 22, 26, 30), yield lower $\Delta F/F_0$ = 0.9, 0.9, 0.5, 0.6, 0.4, and 1.8 responses to 100 μM dopamine concentration, respectively (Figure 3.1e inset). We identify low baseline fluorescence, F_0, for 'short' $(GT)_{4\text{-}8}$-SWCNT complexes as the reason for the large $\Delta F/F_0$ values of these constructs (Figure 3.1a, Figure 3.1e insert, Figure 3.S2, Figure 3.S3). We further note that the (GT) base sequence was found to be uniquely selective for catecholamines over other tested sequences such as $(GA)_6$ (Figure 3.S4), thus we did not change the polymer base sequence identity for nanosensor optimization and only screened the length-effect of $(GT)_N$ polymers. Interestingly, the $(GT)_6$-SWCNT construct also shows increased selectivity towards a new neuromodulator target, norepinephrine, with $\Delta F/F_0$ = 35 sensitivity (Figure 3.1d, 3.1f).

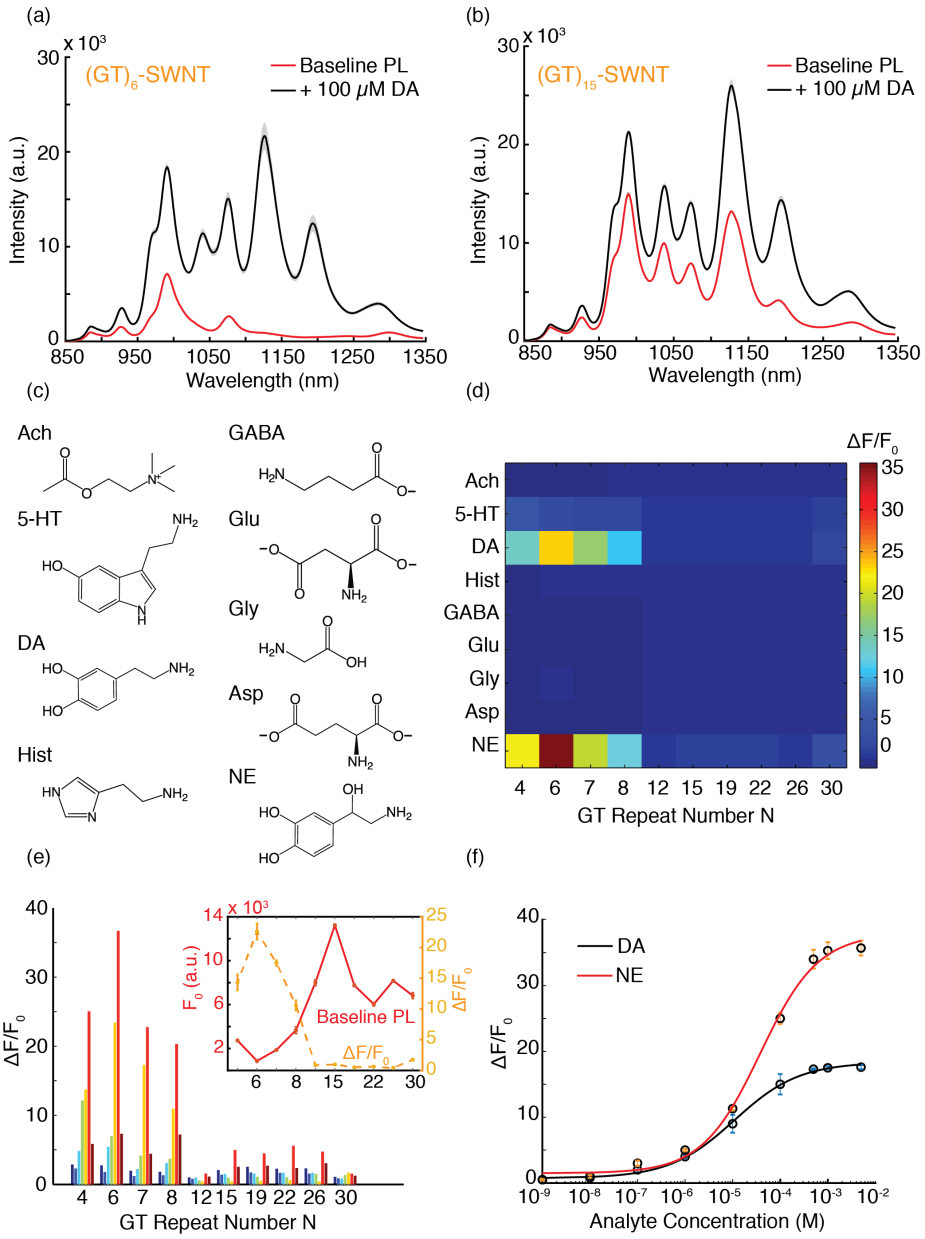

Figure 3.1 Nanosensor response and selectivity for neuromodulators dopamine and norepinephrine as a function of polymer length (a, b) Near-infrared fluorescence spectra of $(GT)_6$-SWCNT and $(GT)_{15}$-SWCNT suspensions before (red trace) and after (black trace) addition of 100 μM dopamine (DA). Mean traces and standard deviation bands from n=3 measurements are presented. **(c, d)** Neurotransmitter analyte library chemical structure and heat map of $\Delta F/F_0$ screen against $(GT)_N$-SWCNT library. Analyte abbreviations: Ach = acetylcholine, 5-HT = serotonin, DA = dopamine, Hist = histamine, GABA = γ-aminobutyric acid, Glu = glutamate, Gly = glycine, Asp = aspartate, NE = norepinephrine. Heat map $\Delta F/F_0$ are computed for the peak intensity of the (9,4) SWCNT chirality (~1127 nm center wavelength) from the convoluted spectra and all measurements were made at pH~7. **(e)** $\Delta F/F_0$ of each sequence suspension, for each SWCNT chirality: (8,3) dark blue, (6,5) blue, (7,5) cyan, (10,2) green, (9,4) and (7,6) yellow, (8,6) and (12,1) red, (10,3) and (10,5) maroon. Insert: Baseline fluorescence intensity of $(GT)_N$ suspensions of the (9,4) chirality (red trace) and change in its fluorescence intensity after addition of 100 μM of dopamine (orange trace). **(f)** $(GT)_6$-SWCNT nanosensor response curve for norepinephrine (red) and dopamine (black) computed for the (9,4) SWCNT peak intensity. Error bars are

standard deviation from n = 3 independent measurements. Experimental data (circles) were fit with Hill equation (solid line).

Our experimental results thus identify polymer length as a key modulator of SWCNT fluorescence quantum yield, which can be exploited for maximizing nanosensor sensitivity and improving selectivity for neuromodulators. Larger diameter SWCNT chiralities exhibited the strongest fluorescence modulation (lowest baseline fluorescence and strongest response to analytes), with the trend emerging most strongly for SWCNT with diameters larger than the (6,5) species (Figure 3.1e, Figure 3.S2, Figure 3.S3). This apparent diameter dependence will be discussed later. We further identify the $(GT)_6$-SWCNT complex as the most suitable nanosensor for imaging both dopamine and norepinephrine, with $\Delta F/F_0$ = 23 and 35, respectively, upon addition of 100 μM analyte concentrations. DNA-SWCNT absorption spectra remain largely invariant to the addition of dopamine and norepinephrine (Figure 3.S1), further suggesting that quantum yield increases drive the increase in nanosensor fluorescence. We next validated the utility of $(GT)_6$-SWCNT to image dopamine and norepinephrine for *in vivo* relevant concentrations. Concentration-dependent fluorescence response curves for $(GT)_6$-SWCNT show fluorescence modulations lie within an optimal dynamic range for *in vivo* imaging of neuromodulation (100 nM to 2 μM) (Figure 3.1f).[30,76,77] At basal dopaminergic and noradrenergic neuronal activity corresponding to at-rest conditions (50 - 100 nM), we observe that the $(GT)_6$-SWCNT construct exhibited $\Delta F/F_0$ values on the order of 1 (100%).[29, 31, 32] At burst firing neuronal activity level typically arising from behavioral response to salient events (1 -2 μM), $\Delta F/F_0$ values on the order of 5 (500%) can be obtained (Figure 3.1f).[29, 31, 32] Equally importantly, the $(GT)_6$-SWCNT construct shows an enhanced selectivity for neuromodulators dopamine and norepinephrine over other potentially competing and ubiquitous neurotransmitters, such as glutamate (Glu), acetylcholine (Ach) and γ-aminobutyric acid (GABA) (Figure 3.1d). We fit our concentration-dependent experimental data points to the Hill equation and determined the dissociation constants (K_d) to be 35 μM for norepinephrine and 10 μM for dopamine (Figure 3.1f).

The molecular selectivity and sensitivity towards catecholamine neuromodulators appears to be highly dependent on nucleobase chemistry. We found that, among others, two poly-C sequences, C_{30}-SWCNT and C_{12}-SWCNT, remain largely non-responsive when exposed to either analyte, consistent with previous studies that show that poly-C ssDNA sequences bind strongly and stably to SWCNT (Figure 3.S4).[78] Other 12-mer sequences, including $(GA)_6$, $(ATTT)_3$, and $(TAT)_4$, similarly exhibit no or negligible sensitivity to both dopamine and norepinephrine (Figure 3.S4). The structure of SWCNT surface adsorbed ssDNA is sensitive to charge screening by counter ions[79] and recent reports have shown that solution ionic strength plays a role in setting the baseline fluorescence ("brightness") of ssDNA-SWCNT constructs.[80] To rule out ionic strength effects, we tested the response of $(GT)_6$-SWCNT to both analytes at solution ionic strengths that varied over two orders of magnitude. We found that the turn-on response remained largely insensitive to ionic strength (Figure 3.S4), suggesting that ionic strength may not play a dominant role in determining baseline fluorescence for short $(GT)_N$ sequences. We also tested the $(GT)_6$-SWCNT nanosensor response to both analytes at low (pH=4), neutral (pH=7), and high (pH=10) conditions. The fluorescence response to dopamine and norepinephrine is observed at all pH conditions, with best responses obtained under physiological pH conditions (Figure 3.S4). We next explored the robustness of the $(GT)_6$-SWCNT nanosensor for potential use in measuring

endogenous dopamine. Time-dependent fluorescence (Figure 3.S5) and absorbance (Figure 3.S6) measurements (Methods in Appendix I) acquired over the course of 7 days confirm polymer-SWCNT stability for all values of N except for N=4.

To probe the stability of our nanosensors in biologically-relevant milieus, we tested the ability of (GT)6-SWCNT to respond to dopamine in both protein-rich media and in artificial cerebral spinal fluid. We observe robust $\Delta F/F_0 = 1.43 \pm 0.16$ turn-on responses to 100 μM dopamine from $(GT)_6$-SWCNT nanosensors that were pre-incubated in cell media (DMEM+ 10% FBS, Methods in Appendix I) (Figure 3.S7a). Furthermore, we tested the compatibility of $(GT)_6$-SWCNT nanosensors for use in artificial cerebrospinal fluid (ACSF), a common media used for *ex-vivo* brain slice imaging studies, and observe nanosensor $\Delta F/F_0$ values of 2.6 ± 0.16 when pre-incubated in ACSF (Figure 3.S7b). We tested the compatibility of our $(GT)_6$-SWCNT nanosensors with potential interfering agents: pharmacological transport inhibitors, and agonists and antagonists of endogenous dopamine receptors. We found that $(GT)_6$-SWCNT fluorescence was insensitive to the dopamine transporter inhibitor nomifensine, and dopamine receptor (DRD2) agonist quinpirole, and antagonists sulpiride and haloperidol (Figure 3.S8). $(GT)_6$-SWCNT incubated in these drugs retained its strong turn-on response to dopamine (nomifensine: 23.7 ± 1.51; sulpiride: 22.7 ± 0.67; quinpirole: 24.27 ± 0.87; haloperidol: 25.77 ± 0.98; all responses to 100 μM dopamine; mean $\pm$ st. dev. from N=3 replicates) permitting the possible use of $(GT)_6$-SWCNT constructs in conjunction with drugs that target endogenous receptors and transporters of dopamine. Lastly, single-molecule total internal reflection fluorescence (TIRF) microscopy of surface immobilized $(GT)_6$-SWCNT nanosensors (Methods in Appendix I) suggest that ssDNA adsorbed onto SWCNT surface is resistant to degradation by endonucleases (Figure 3.S9). We attribute this apparent protective effect to steric hinderance of the SWCNT prohibiting substrate access to the nuclease's active site. Lastly, prior work from our lab has shown that molecular recognition using SWCNT-polymer conjugates is two-photon compatible, suggesting several imaging modalities used in neuroimaging can be exploited to image $(GT)_6$-SWCNT in biological tissue.[62] Taken together, these results suggest that the $(GT)_6$-SWCNT construct can serve as a dopamine and norepinephrine nanosensor with the dynamic range, binding kinetics, and robustness compatible with *in vivo* utility.

Solvatochromic Shifting Reveals Dopamine and Norepinephrine-Specific Molecular Recognition

We performed surfactant displacement experiments to gain further insight into how analytes modulate the quantum yield of $(GT)_N$ polymer functionalized SWCNT constructs. Recent work has shown that, when added to DNA-SWCNT suspensions, surfactants such as sodium cholate (SC) adsorb to exposed SWCNT surface and displace adsorbed ssDNA, thereby altering the SWCNT's surface dielectric properties and causing a solvatochromic shift in exciton optical transition energies (Figure 3.2a, 3.2b).[81–83] As expected, addition of SC to $(GT)_N$-SWCNT induce solvatochromic shifts in $(GT)_N$-SWCNT fluorescence center wavelengths (Figure 3.2b). All constructs showed characteristic SC-induced blue-shifting of center wavelengths corresponding to SWCNT chiralities in the sample. We next repeated SC displacement experiments for all $(GT)_N$-SWCNT suspensions pre-incubated in 10 μM dopamine. Surprisingly, addition of dopamine to $(GT)_N$-SWCNT suspensions before addition

of SC either reduces or eliminates the SC-induced shifting in exciton optical transitions, suggesting that the surfactant is unable to displace the surface adsorbed ssDNA in the presence of dopamine (Figure 3.2c, Figure 3.S10a, 3.S10c, 3.S10d). We propose that the stabilization of $(GT)_N$ polymers on SWCNT arises from a selective interaction between the dopamine analyte and dopamine-specific recognition pockets in the $(GT)_N$-SWCNT conjugate, and that dopamine trapped in binding pockets enhance fluorescence by interacting with both the adsorbed polymer and the SWCNT. We posit that as a result of these interactions, polymer-mediated binding of analytes selectively enhances the fluorescence quantum yield of ssDNA-SWCNT nanosensors, as we further explore using experimental and computational approaches below.

To probe the selectivity of dopamine-induced nanosensor stabilization, we conducted time-resolved SC shift experiments with the $(GT)_6$-SWCNT construct in which *p*-tyramine is added to the suspension before addition of SC. Tyramine, a molecular analogue of dopamine differing by one hydroxyl group, does not modulate the fluorescence of $(GT)_6$-SWCNT (Figure 3.S11a). We reasoned that the recognition of dopamine and norepinephrine is mediated by unique recognition sites in the $(GT)_6$-SWCNT corona, and that tyramine's inability to modulate SWCNT fluorescence is a consequence of its inability to bind these recognition sites. With this hypothesis, the efficacy of SC in displacing surface adsorbed $(GT)_6$ ssDNA and resulting solvatochromic shift should be unaffected by tyramine. Our results do indeed show that 10 μM tyramine, unlike dopamine, does not attenuate the SC induced peak shifts (Figure 3.2d), suggesting that tyramine is unable to bind to and stabilize surface adsorbed ssDNA strands.

Our results further indicate that the stability imparted to the SWCNT-ssDNA corona phase by the binding of dopamine and norepinephrine is related to the analyte-induced fluorescence modulation specific to the GT base sequence. A $(GA)_6$-SWCNT construct, in contrast to $(GT)_6$-SWCNT, exhibits negligible modulation in fluorescence upon addition of either dopamine or norepinephrine (Figure 3.S4). We incubated the $(GA)_6$-SWCNT suspension in dopamine to measure SC induced peak shifts. We observed that dopamine tentatively stabilizes $(GA)_6$-SWCNT corona (Figure 3.2e). However, the dopamine-induced stability of $(GA)_6$-SWCNT is short-lived, with distinctive solvatochromic peak shifting occurring with a 60 second delay following SC addition. Another 12-mer sequence, C_{12}, similarly exhibited SC-induced solvatochromic shifting despite the presence of dopamine (Figure 3.S10b). These results suggests that SC-induced peak shifting is a function of both the dopamine-bound fraction of recognition sites in the SWCNT-polymer corona, and the intrinsic binding affinity between the polymer sequence and SWCNT surface. Furthermore, we found that both dopamine and norepinephrine modulate the Raman G^- band of the $(GT)_6$-SWCNT between 1500 and 1550 cm^{-1}, whereas *p*-tyramine does not (Figure 3.S12). The increased intensity of the Raman G^- band by dopamine and norepinephrine, but not tyramine, is maintained regardless of the subsequent addition of SC. Absorbance measurements show that addition of analytes does not change the E_{22} transition energies of SWCNTs, (Figure 3.S1, 3.S11b) and therefore cannot explain the observed phenomena. A number of interactions can cause changes in Raman intensity or frequency, including changes in polymer conformation, solvation dynamics and variations in local electric field. The presence of degenerate modes in the G^- band of SWCNTs further raises the possibility of analyte-mediated symmetry breaking. The persistence of these changes even after SC

addition further supports the hypothesis we propose regarding polymer-SWCNT-analyte interaction.

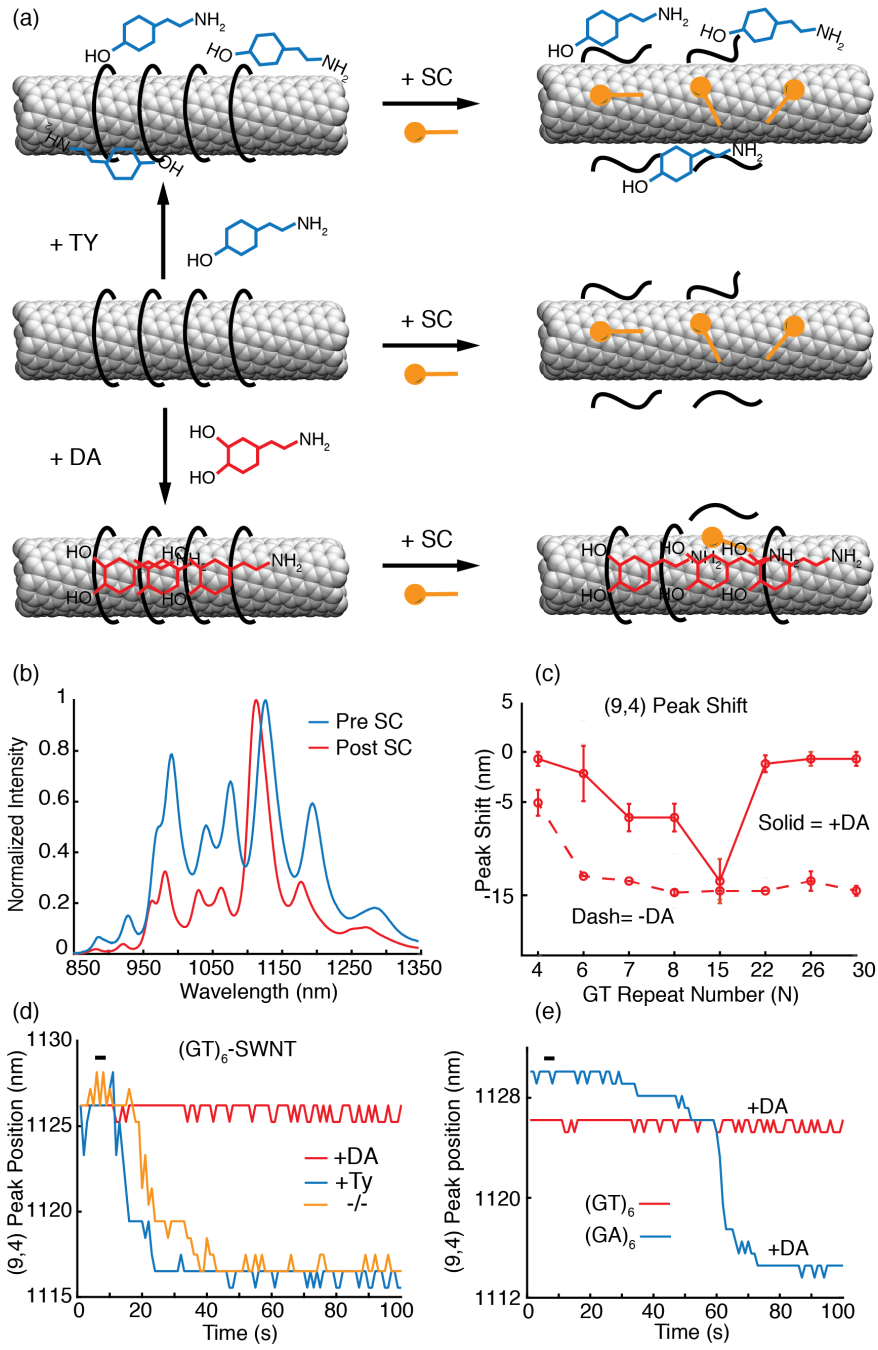

Figure 3.2 Solvatochromic shifts reveal neuromodulator-specific molecular interactions with nanosensors dependent on ssDNA sequence and length (a) Middle row: sodium cholate (SC) binds to exposed SWCNT surfaces and displaces bound $(GT)_N$ polymers. Bottom row: Nanosensor incubation in dopamine (DA) or norepinephrine (NE) stabilizes ssDNA polymers on the SWCNT surface, disallowing SC from accessing the SWCNT surface. Top row: Incubation in p-tyramine (TY) does not stabilize surface adsorbed ssDNA against displacement by SC **(b)** 1 wt.% SC induces a solvatochromic shift in SWCNT fluorescence. The shift for the $(GT)_6$-SWCNT conjugate is presented here as an example. **(c)** Fluorescence peak shift

corresponding to the (9,4) SWCNT chirality (~1127 nm) upon exposure to 1 wt.% SC without (dash trace) and with (solid trace) pre-incubation in 10 μM DA. Error bars are standard deviation from n = 3 measurements. Negative peak shits correspond to blue shifting of the peak in the emission spectrum, as shown in (b). **(d)** Time-resolved fluorescence measurements of $(GT)_6$-SWCNT incubated in 10 μM DA (red trace), 10 μM p-tyramine (TY) (blue trace), and incubated in neither (orange trace). Upon addition of 0.25 wt. % SC indicated by the black bar, solvatochromic peak shift in the dopamine incubated corona is eliminated. **(e)** SC induced solvatochromic peak shift in $(GA)_6$-SWCNT incubated in 10 μM of dopamine suggests $(GA)_6$ exhibits short lived stability on SWCNT following dopamine incubation.

We probed whether the surface density of the $(GT)_N$ polymer on the SWCNT surface can tune the density of molecular recognitions sites available to analyte. We varied polymer surface packing of the $(GT)_6$-SWCNT construct by synthesizing nanosensors with different mass proportions of SWCNT (mS) to $(GT)_6$ DNA polymers (mD). The resulting $(GT)_6$-SWCNT conjugates thus have variable surface-adsorbed polymer density (Figure 3.3a) with nominal mS/mD mass ratios of 2, 5, and 10, representing a spectrum from 'high' to 'low' $(GT)_6$ polymer surface density. The resulting fluorescence intensity from equimolar SWCNT aliquots shows a clear trend whereby the highest polymer surface densities (mS/mD = 2) exhibit the lowest baseline fluorescence (Figure 3.3b). Addition of 10 μM of dopamine enhances the SWCNT fluorescence of all three samples; however, the $\Delta F/F_0$ nanosensor response is highest for the SWCNT sample with the highest surface coverage (Figure 3.3b). These results suggest that (i) the degree of baseline fluorescence quenching of SWCNT by adsorbed $(GT)_6$ is directly proportional to the polymer surface density; (ii) the higher the polymer surface coverage, the higher the number of dopamine binding pockets; and (iii) dopamine enhances SWCNT quantum yield in proportion to the density of bound recognition sites.

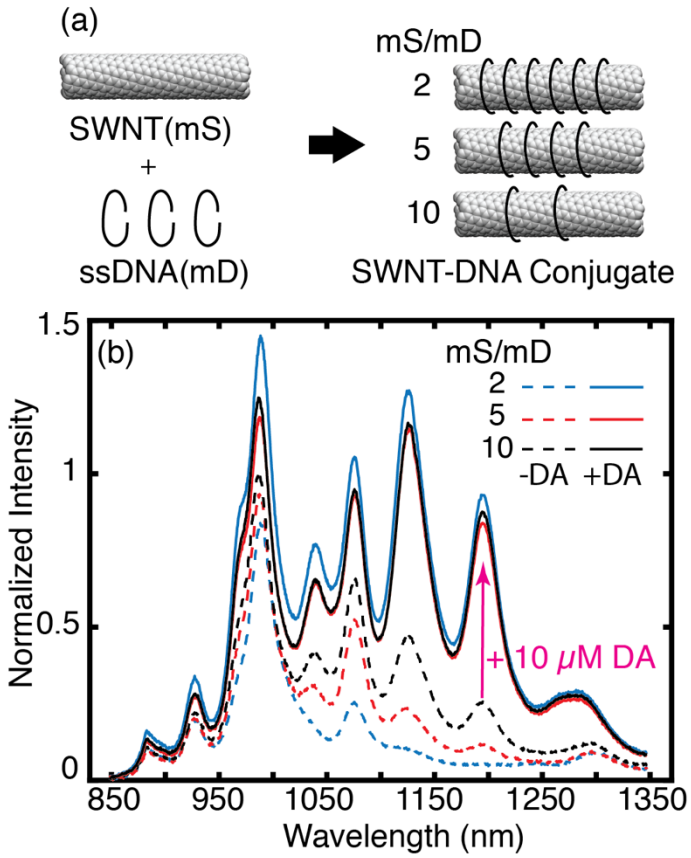

Figure 3.3 DNA surface coverage of SWCNT modulates dopamine binding sites. (**a**) Preparation of SWCNT sensors with varying $(GT)_6$ polymer surface density. The mass ratio of SWCNT to ssDNA (mS/mD) is varied to prepare three suspensions with m/n = 2, 5 and 10. (**b**) Fluorescence spectra of 5 mg/L $(GT)_6$-SWCNT samples (dashed plots), with corresponding fluorescence spectra after addition of 10 μM of dopamine (solid plots), normalized to the peak fluorescence intensity observed for the mS/mD=10 sample before addition of 10 μM dopamine.

3.3 Conclusion

We synthesized a SWCNT based high turn-on probe for the neuromodulators dopamine and norepinephrine. We show that $(GT)_N$-based ssDNA length plays a critical role in setting the baseline brightness of the ssDNA-SWCNT hybrid structures, which in turn dictates critical optical probe parameters, including the strength of turn-on response and the dynamic range of the response. We demonstrate that short ssDNA length alone is not a sufficient criterion to elicit strong turn-on responses and there are at least two other parameters that exert a considerable influence on probe performance. First, we show that the sequence's nucleobase chemistry plays an important role. For example, $(GA)_6$, in contrast to $(GT)_6$, produced suspensions with bright baseline fluorescence that is minimally perturbed by the addition of dopamine. Secondly, we demonstrate that surface density of adsorbed ssDNA moieties contributes to setting the baseline brightness and subsequent turn-on response. Densely functionalized SWCNTs exhibited quenched baseline and

stronger response to dopamine. We introduced a novel surfactant displacement-based assay to show that the process of molecular recognition involves a three-way interaction between the SWCNT surface, dopamine molecules and ssDNA oligonucleotides. This assay helped us harmonize key experimental observations, including the dependence of turn-on response on sequence length and sequence chemistry. When dopamine molecules are absent from solution, sodium cholate (SC)-induced displacement of ssDNA is facile, inducing well-known solvatochromic shifts in the fluorescence emission spectra of SWCNT. Addition of dopamine eliminated this shift in a dose-dependent manner, suggesting that dopamine molecules trapped by surface recognition sites either stabilized the adsorbed ssDNA against SC-induced displacement or disallowed SC access to the SWCNT surface. ssDNA sequences that produced diminished turn-on responses (either because of their chemistry or length) were displaced by SC even in the presence of dopamine, in contrast to sequences that engender strong turn-on response. In Chapter 4, we will introduce molecular dynamics simulation strategies to bridge our macroscale experimental observations with molecular-level processes that underpin our experimental observations.

3.4 Appendix I

Materials and Methods

Suspension of SWCNT in ssDNA

All ssDNA oligonucleotides were purchased from Integrated DNA Technologies (Standard Desalting). HiPCo SWCNT were purchased from NanoIntegris (Batch # HR27-104). Each ssDNA-SWCNT colloidal suspension was prepared by mixing 1 mg of ssDNA and 2 mg of SWCNT in 1 mL of 100 mM NaCl solution. The solution was bath sonicated (Branson Ultrasonic 1800) for 10 minutes and probe-tip sonicated for 10 minutes at 5 W power (Cole Parmer Ultrasonic Processor, 3 mm tip diameter) in an ice-bath. The sonicated solution was incubated at room temperature for 30 minutes. The product was subsequently centrifuged at 16,000 g (Eppendorf 5418) for 90 minutes to remove unsuspended SWCNT bundles and amorphous carbon, and the supernatant was recovered for further characterization. To vary ssDNA SWCNT surface packing, we used 2 mg, 5 mg, or 10 mg of starting SWCNT masses in 1 mg of $(GT)_6$ dissolved in 100 mM NaCl.

Characterizations of SWCNT-ssDNA suspensions

All absorption measurements were taken with a UV-VIS-NIR spectrophotometer (Shimadzu UV-3600 Plus) or UV-VIS (ThermoFisher Scientific Genesys 20). SWCNT concentrations of as-made ssDNA-SWCNT suspensions were determined using absorbance at 632 nm (UV-VIS) and extinction coefficient of $\varepsilon = 0.036\ (mg/L)^{-1}\ cm^{-1}$.[80] Full spectrum absorbance measurements were recorded with UV-VIS-NIR after dilution to 5 mg/L SWCNT concentration in 100 mM NaCl. For fluorescence measurements, each suspension was diluted to 5 mg/L in 100 mM NaCl and aliquots of 198 µL volume were placed in each well of a 96-well plate (CORNING). Fluorescence measurements were obtained with a 20X objective on an inverted Zeiss microscope (Axio Observer.D1) coupled to a Princeton Instruments spectrometer (SCT 320) and liquid nitrogen cooled Princeton Instruments InGaAs detector

(PyLoN-IR). A 721 nm laser (OptoEngine LLC) was used as the excitation light source. To investigate solution ionic strength, $(GT)_6$-SWCNT suspensions were diluted to 5 mg/L in 1 mM, 10 mM, 50 mM, 100 mM, and 200 mM NaCl solution and allowed to incubate for 24 hrs. before fluorescence measurements were taken. pH adjustments were made using HCl or NaOH and fluorescence measurements were taken after 1 hr. equilibration at room temperature. We used 2 s exposure times at laser power of 65 mW for most measurements. In very bright SWCNT suspensions, exposure times were reduced to 0.5 s or 1 s and fluorescence counts were rescaled for comparison and analysis. All absorbance and fluorescence measurements were background corrected with a blank 100 mM NaCl solution. All measurements were made in triplicate. Reported results are averages and standard deviations of the triplicate measurements.

$(GT)_N$-SWCNT stability experiments

We tested the stability of all $(GT)_N$-SWCNT suspensions with fluorescence and absorbance spectroscopy. Prior work has shown that DNA-SWCNT fluorescence stability directly correlates with DNA polymer stability on the SWCNT surface.[78] To rule out the possibility that spontaneous DNA polymer rearrangement or dilution effects contribute to the large increase in nanosensor fluorescence we observed for 'short' sequences, we measured the time-dependent fluorescence stability of all $(GT)_N$-SWCNT suspensions with near infrared fluorescence spectroscopy. The fluorescence spectra of all $(GT)_N$-SWCNT suspensions were collected for a period of > 2 hrs. immediately following dilution to 5 mg/L in 100 mM NaCl. Most $(GT)_N$-SWCNT suspensions exhibit stable fluorescence ($\Delta F/F_0 < -15\%$) with the exception of $(GT)_4$-SWCNT, which shows higher degree of fluorescence instability ($\Delta F/F_0 = -40\%$) (Figure 3.S5). Importantly, all sequences exhibit a decrease in intensity that is over an order of magnitude less than the fluorescence increase observed in response to both analytes (Figure 3.S5) suggesting that nanosensor response to analytes arises from specific molecular interaction between $(GT)_N$-SWCNT and the analyte and does not arise from volume or dilution effects. The differences in time-dependent fluorescence modulation exhibited by each suspension, as shown in Figure 3.S5, suggests that polymer length affects the base stacking stability of the (GT)N-SWCNT suspensions with an apparent instability for N = 4.

Absorbance measurements were also carried out to study the stability of different (GT)N polymers on SWCNT. After synthesis of each (GT)N-SWCNT construct, excess ssDNA was removed from the colloidal suspension (Amicon Ultra 100kDA MWCO), and absorption spectra were recorded with a UV-VIS-NIR spectrophotometer. The filtered suspension was then left to incubate at room temperature for 1 week (7 days). After 1 week, absorbance spectra were again collected for each $(GT)_N$-SWCNT construct and compared to the sample's initial absorbance. Absorbance values near 260 nm, the DNA absorbance peak, reveal that negligible ssDNA polymer desorption occurs from $(GT)_N$-SWCNT constructs within the 1-week timeframe, with the exception of $(GT)_4$-SWCNT that shows appreciable $(GT)_4$ polymer desorption from the SWCNT surface (Figure 3.S6). Our results suggest that $(GT)_N$ sequences with N>4 form stable non-covalent conjugates with SWCNT. For $(GT)_4$-SWCNT, we observe a significant increase in absorbance at ~260nm (presumably due to absorbance in the sample filtrate from desorbed DNA). We further note that sequences shorter than $(GT)_4$ did

not enable suspension of SWCNT. These results provide further evidence for colloidal stability of $(GT)_6$-SWCNT, the ultrasensitive dopamine and norepinephrine nanosensor.

Analyte fluorescence response measurements

All neurotransmitters were purchased from Sigma-Aldrich. For neurotransmitter response measurements, we collected fluorescence from 198 μL volumes of suspensions (5 mg/L SWCNT concentration) before and after addition of 2 μL of 10 mM solutions of each analyte (for 100 μM final analyte concentration in each well). For dose response curves, analyte stock concentrations were prepared to obtain the target concentration in each well upon addition of the 2 μL volumes. Responses to drugs were measured in the same manner. We used 96-well plates (CORNING, 200 μL total volume per well) for screening experiments. Analytes were incubated for 5 minutes before taking post-analyte fluorescence measurements. Responses were calculated for the (9,4)-SWCNT chirality peak (~1127 nm center wavelength) as $\Delta F/F_0 = (F-F_0)/F_0$, where F_0 is fluorescence before analyte addition and F is fluorescence after analyte addition and following a 5-minute incubation period. Peak heights (amplitudes) at center wavelengths corresponding to known SWCNT (n,m) chiral index in the convoluted spectra are used for all $\Delta F/F_0$ calculations (Figure 3.1e). Dose-response measurements were fitted to Hill equation, from which dissociation constants were evaluated.[84,85] All measurements were made in triplicate. Reported results are averages and standard deviations of the triplicate measurements. To measure dopamine response of $(GT)_6$-SWCNT in DMEM (Dulbecco's) supplemented with 10% Fetal Bovine Serum (FBS) (Gibco, ThermoFisher Scientific), we diluted the as made suspension to 5 mg/L SWCNT concentration in the media and allowed 1 hr. incubation at room temperature. Dopamine response was measured as described above. The same procedure was used for artificial cerebrospinal fluid (ACSF) (119 mM NaCl, 26.2 mM $NaHCO_3$, 2.5 mM KCl, 1mM NaH_2PO_4, 1.3 mM $MgCl_2$, 10 mM Glucose, 2 mM $CaCl_2$).

Single molecule TIRF experiments

We used visible fluorophore (Cy5) tagged single strand DNA, Cy5-$(GT)_6$ and total internal reflection fluorescence (TIRF) to show that ssDNA adsorbed on SWCNT surface are resistant to degradation by nucleases. To do this, we dissolved biotinylated-Cy5-tagged $(GT)_6$ (referred to as Cy5-$(GT)_6$ in this study) (Integrated DNA Technologies) in 100 mM NaCl (nuclease free) by gentle shaking at 50 RPM (Waverly S1C-E) for 30 minutes, then diluted it to 150 pM concentration. Cy5-tagged $(GT)_6$-SWCNT suspensions (referred to as Cy5-$(GT)_6$-SWCNT in this study) were prepared as described previously, and spin-filtered with 100 kDa Amicon filters (Ultra-0.5mL Centrifugal Filter) 10 times with nuclease-free water to remove free (unsuspended) $(GT)_6$. The SWCNT concentration of the resulting supernatant was measured and the solution diluted to 0.2 mg/L SWCNT concentration. S1 nuclease (Promega) was diluted using 1x reaction buffer to 250 nM. We used 6-channel slides (ibidi μ-Slide VI 0.5 Glass). Prior to use, each channel was washed by adding 100 μL of 100 mM NaCl to one end and removing 60 μL on the opposite end. The addition of any subsequent solution was immediately followed by the removal of an equal volume of solution at the other end of the channel. In all subsequent steps, substrates were added in 50 μL volumes, and

channels flushed with 50 μL solution (100 mM NaCl) to remove unbound substrates post-incubation. First, 0.25 mg/mL of biotinylated Bovine Serum Albumin (BSA-Biotin) and 0.05 mg/mL NeutrAvidin (ThermoFisher Scientific) were added to each channel and incubated for 5 minutes. Non-specific adhesion afforded labeling of the glass surface with BSA-Biotin-NeutrAvidin complexes. Next, Cy5-$(GT)_6$ or Cy5-$(GT)_6$-SWCNT were incubated in experimental channels for 5 minutes. Biotin-Cy5-$(GT)_6$ would bind to surface immobilized BSA-Biotin-NeutrAvidin complexes through specific biotin-NeutrAvidin interactions. On the other hand, non-specific adhesion between SWCNT surface and BSA/Neutravidin proteins affords immobilization of the nanosensor (Figure 3.S9). After DNA or SWCNT-DNA immobilization, each channel was incubated for 15 minutes in 250 nM S1 nuclease and rinsed with 50 μL NaCl solution to remove degraded DNA. All images were collected with laser excitation at 642 nm, a 655 nm LP emission filter, TIRF angle of 65.35°, and exposure time of 1000 ms (Zeiss Elyra PS.1). The channels were imaged pre and post nuclease incubation. A negative control for each ibidi slide involved using 100 mM NaCl solution in place of DNA or DNA-SWCNT. A second negative control used incubation in 100 mM NaCl solution in place of S1 nuclease (Figure 3.S9). The acquired images were processed in MATLAB. An algorithm removed dead pixels and background noise before the image underwent thresholding to obtain a binary image. A built-in function quantified the number of Cy5 fluorophores (spot count) present per field of view. Approximately 25 fields of view were acquired per channel, and each channel experiment was conducted in triplicate. Spot counts for each channel were averaged over the 25 fields of view and the percentage change computed for each channel using pre and post nuclease incubation.

Surfactant-induced solvatochromic shift experiments

We used sodium cholate (SC) (Alfa Aesar) for surfactant displacement experiments. SC solutions was prepared in deionized water and aliquots were added to each well of a 96-well plate for final SC concentrations of 0.25 wt.% for time-resolved experiments and 1 wt.% for steady-state experiments. For time-resolved solvatochromic shift experiments, spectra were collected at 1 s intervals and SC was added 10 s after start of acquisition to obtain 0.25 wt.% SC in each well. Each acquisition lasted between 2 and 5 minutes and SC was allowed to diffuse passively through the well during acquisition. For analyte incubated wells, the wells were spiked to final analyte concentrations of 10 μM for time-resolved experiments or 100 μM for steady-state experiments. Analytes were allowed to incubate for 5 minutes before addition of SC to a final concentration of 0.25 wt.% or 1 wt.%.

$(GT)_6$-SWCNT Raman measurements

Raman spectra were acquired on a Horiba LabRAM HR Raman microscope. All samples were excited with a 532 nm laser line (50 mW) through a 20x objective and the Raman spectra were collected in a backscattering geometry from 200 μL volume 96-well plates. For all experiments, $(GT)_6$-SWCNTs were prepared to a concentration of 20 mg/L in 100 mM NaCl. Stock solutions containing dopamine (DA), norepinephrine (NE) and tyramine (TY) were added to each well for a final analyte concentration of 100 μM. Sodium cholate (SC) was added to select samples for a final concentration of 0.5 wt.% in each well.

In measurements containing analytes and SC, the analyte was added to the $(GT)_6$-SWCNT solution first and allowed to incubate for 1 minute before SC was added.

3.5 Appendix II

Supporting Information

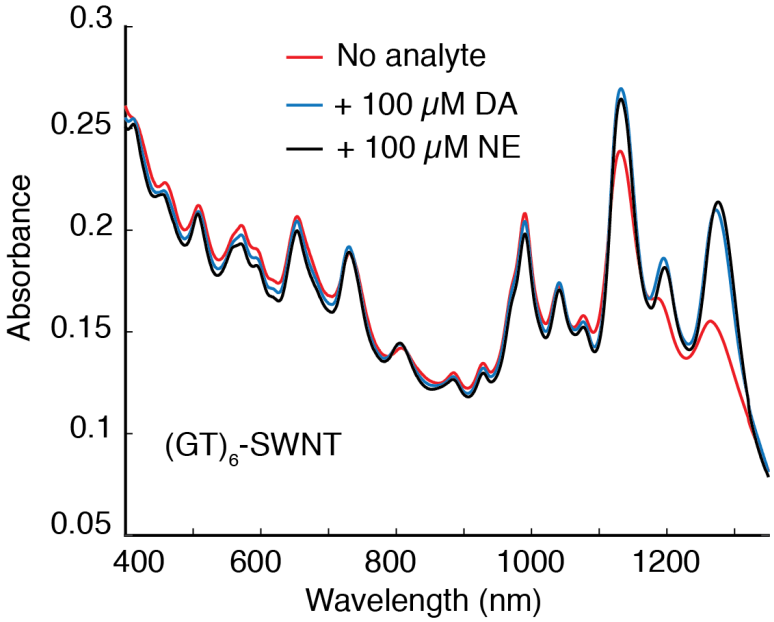

Figure 3.S1. Absorption spectra of $(GT)_6$-SWCNT before and after analyte addition. Absorbance of $(GT)_6$-SWCNT before (red trace) and after (black and blue traces) addition of 100 μM dopamine (DA) and norepinephrine (NE) shows little change at 721 nm, the excitation wavelength used for all fluorescence measurements in this study. E_{22} transitions are unaffected whereas addition of analytes is observed to reduce transition bleaching in the E_{11} region of the spectrum.

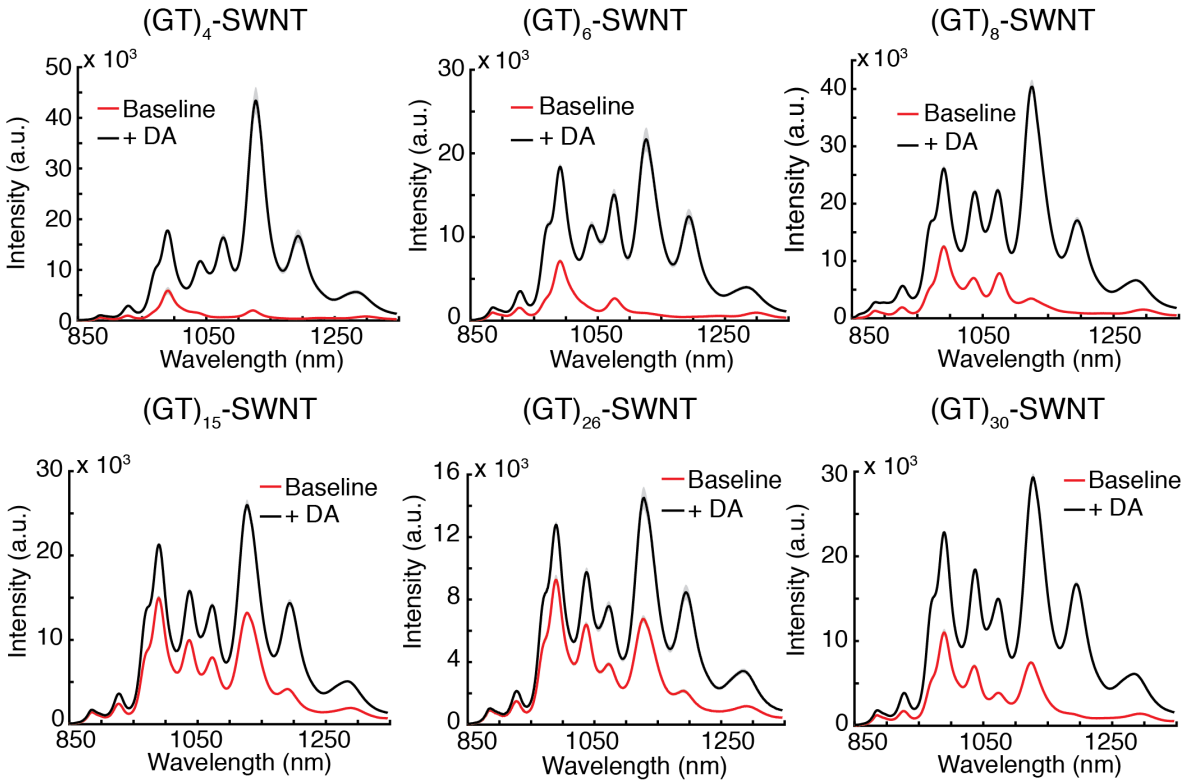

Figure 3.S2 Fluorescence spectra of three short (N=4, 6, 8) and long (N=15, 26, 30) of $(GT)_N$-SWCNT suspensions. Fluorescence before addition (red trace) and after (black trace) addition of 100 μM of dopamine (DA) is shown. Mean traces and standard deviation (gray band) from N=3 technical replicates are presented.

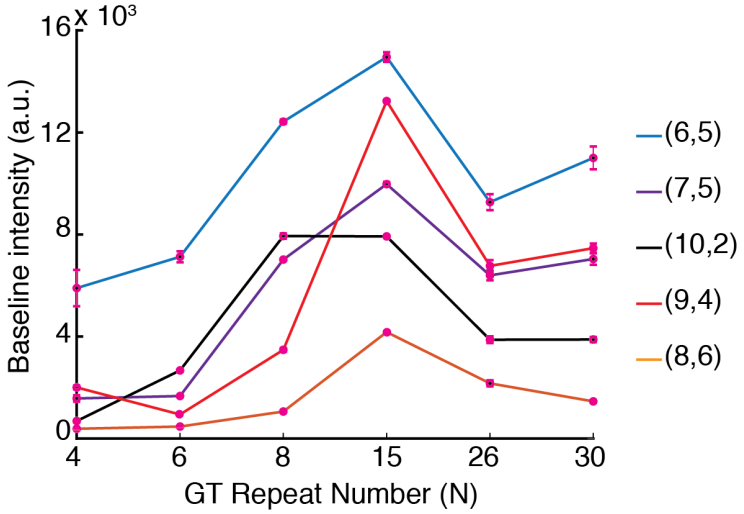

Figure 3.S3 Baseline fluorescence intensity of $(GT)_N$-SWCNT before any analyte addition shows a diameter dependent fluorescence quenching. SWCNT chiralities bigger than the (6,5) species show the lowest baseline fluorescence that increases with increasing N. Error bars are standard deviation of N=3 technical replicates.

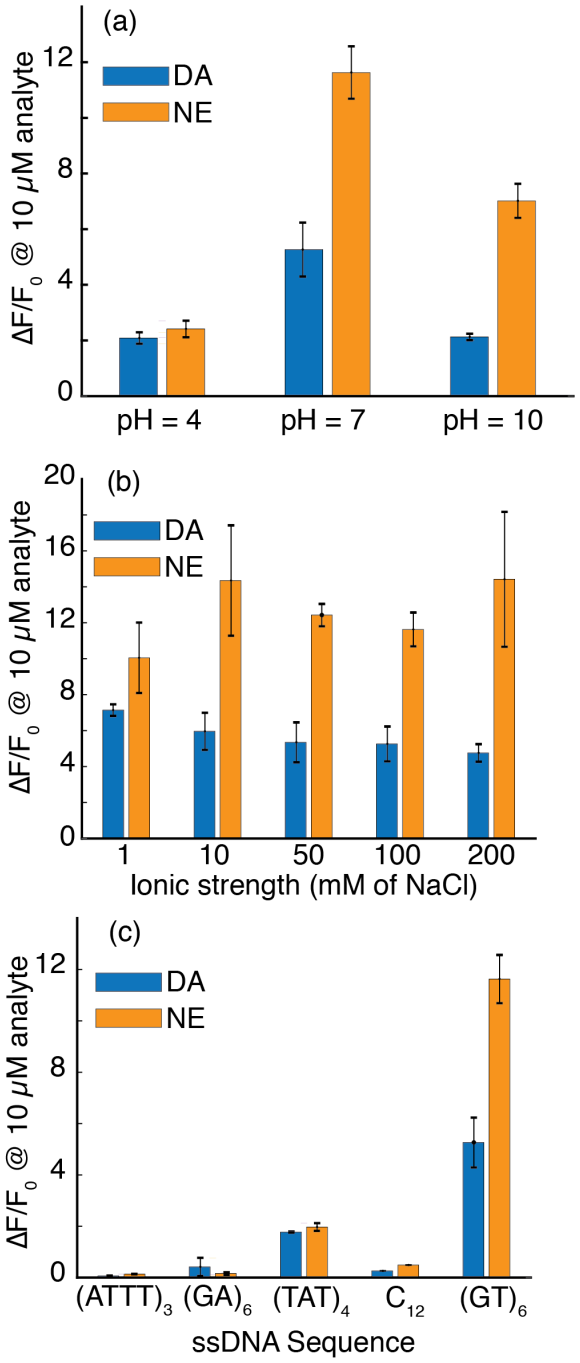

Figure 3.S4 Nanosensor stability over varying ionic strengths and pH. (**a**) Nanosensor response to dopamine and norepinephrine is observed for a wide range of solution pH, with maximal response occurring at physiological pH of 7. (**b**) Nanosensor response to dopamine and norepinephrine under NaCl ionic strength conditions that vary over two orders of magnitude. (**c**) Response to dopamine and norepinephrine is GT sequence specific. Experiments with other 12-mer constructs show marginal $\Delta F/F_0$ compared to $(GT)_6$. Error bars are standard deviation of N=3 technical replicates. All $\Delta F/F_0$ are reported for the peak intensity change at the center wavelength of (9,4) SWCNT chirality (~1127 nm) from the convoluted fluorescence spectra.

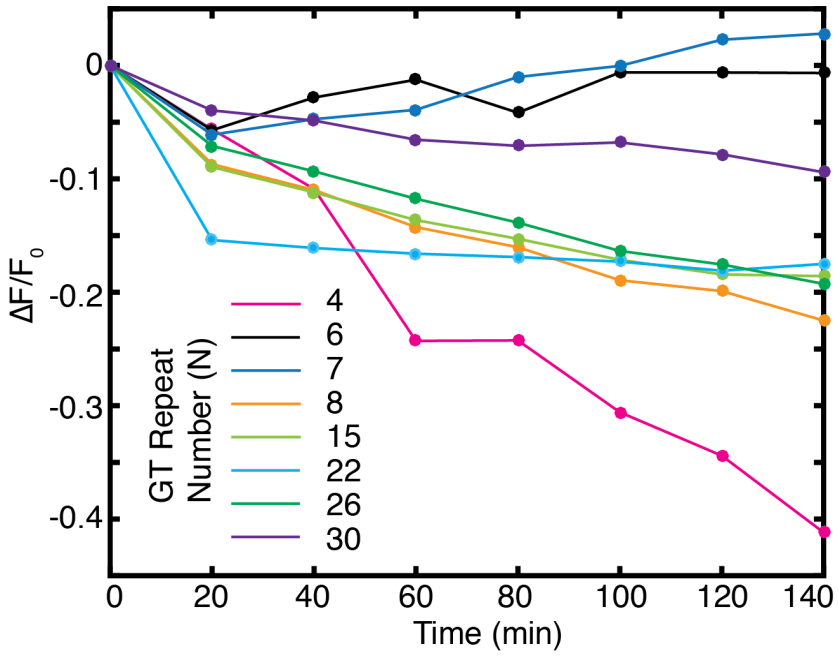

Figure 3.S5 Change in $(GT)_N$-SWCNT fluorescence intensity as a function of time. All suspensions were diluted to a SWCNT concentration of 5 mg/L in 100 mM NaCl and their fluorescence spectrum was monitored over two hours immediately following dilution.

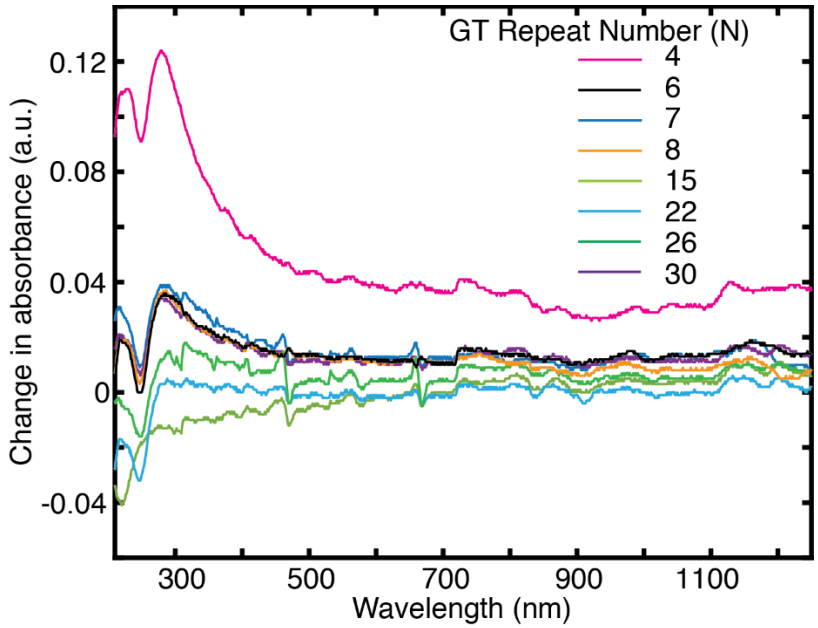

Figure 3.S6 DNA desorption from SWCNT over the course of 1 week. Change in absorbance for $(GT)_N$-SWCNT suspensions after 1 week of incubation, indicating the relative instability of the $(GT)_4$-SWCNT suspension compared to $(GT)_6$-SWCNT and longer. Absorption at 260 nm corresponds to desorbed ss(GT)N polymer. For more details, see Methods in Appendix I.

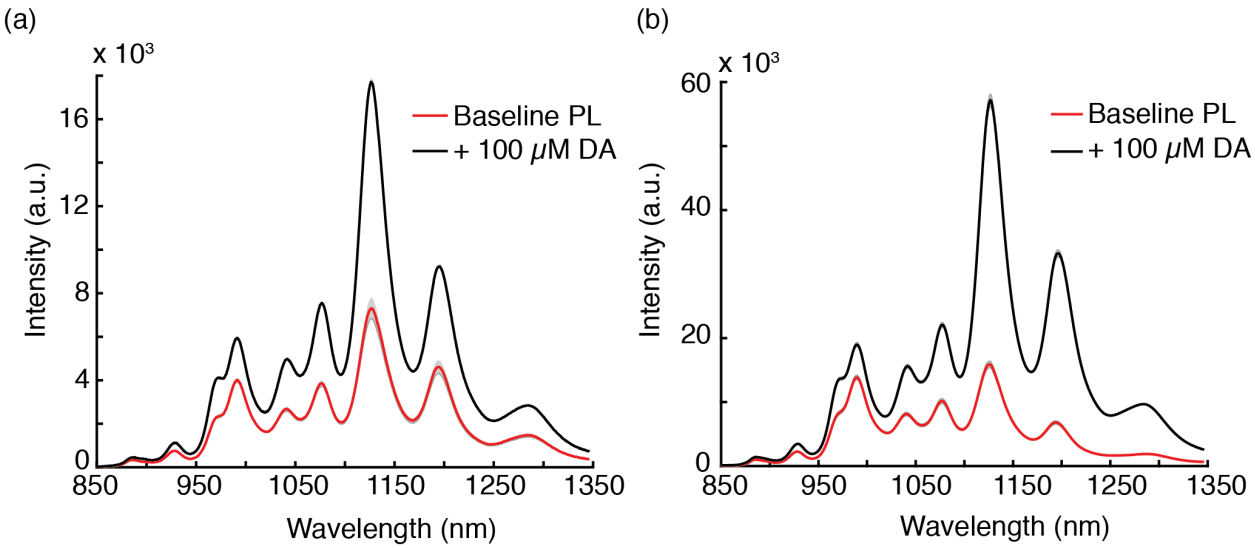

Figure 3.S7 (a) $(GT)_6$-SWCNT response to dopamine (DA) after 1-hr incubation in DMEM+10% FBS. $(GT)_6$-SWCNT was diluted and equilibrated in DMEM+10% FBS for 1 hr. before dopamine response measurements were taken. (**b**) Another set of dopamine response experiments were repeated with nanosensors equilibrated in artificial cerebrospinal fluid (ACSF). Data is presented as a mean trace and standard deviation (gray band) from N=3 measurements.

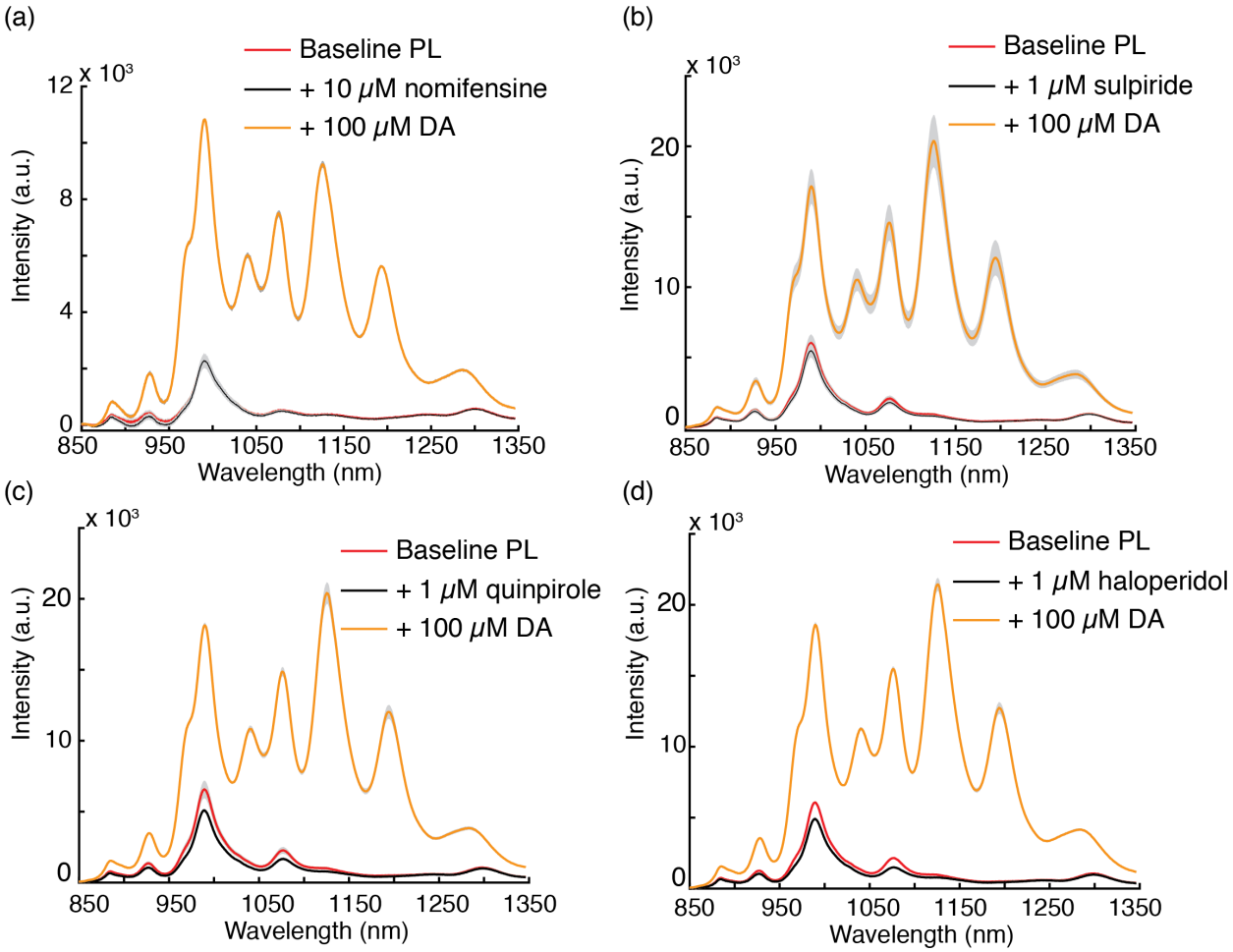

Figure 3.S8 Response of $(GT)_6$-SWCNT to various drugs. No response or negligible negative responses are observed for (**a**) 10 μM of nomifensine and 1 μM each of (**b**) sulpiride, (**c**) quinpirole and (**d**) haloperidol. After incubation in each drug, subsequent responses to 100 μM of dopamine are measured and show no attenuation (orange traces). All traces are presented as mean and standard deviation (gray band) from N=3 technical replicates.

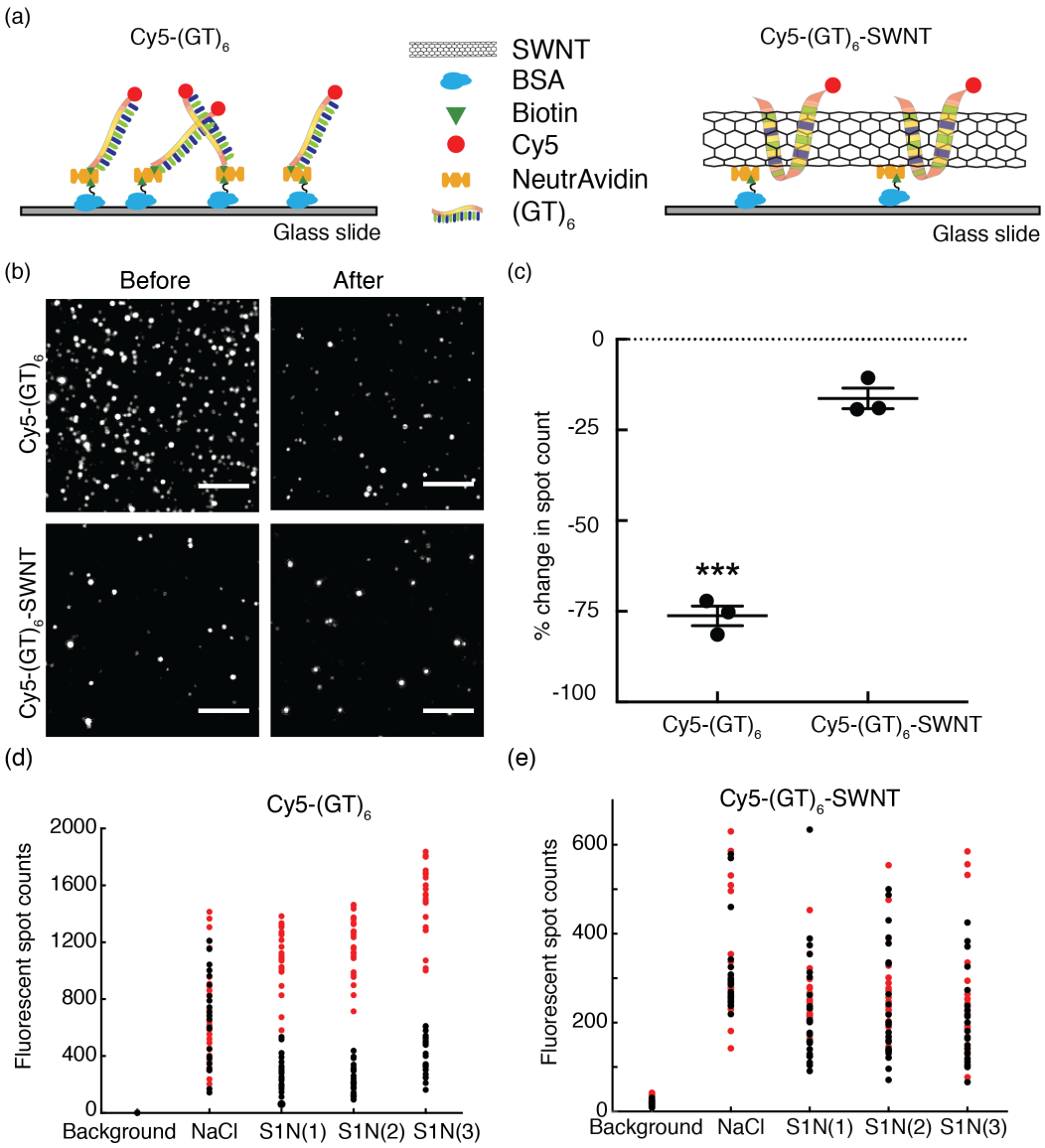

Figure 3.S9 Single molecule TIRF is used to evaluate degradation of ssDNA by S1 nuclease. (**a**) Cy5-$(GT)_6$ and Cy5-$(GT)_6$-SWCNT were surface immobilized on a glass slide (Methods in Appendix I). (**b**) A representative field of view in a channel with Cy5-$(GT)_6$ (top row) and Cy5-$(GT)_6$-SWCNT (bottom row) before and after 15-minute incubation in S1 nuclease. S1 nuclease mediated degradation of ssDNA diminishes Cy5 fluorescence. Scale bars = 5 μm. (**c**) Percentage change in Cy5 spot count shows $(GT)_6$ adsorbed on SWCNT are not degraded as effectively by S1 nuclease compared with free $(GT)_6$ ($p < 0.001$). (**d**) Scatter plot of spot counts in a control lane treated with 100 mM NaCl (Background) shows negligible non-specific fluorescence. Four channels in which Cy5-$(GT)_6$ are immobilized shows that treatment with 100 mM NaCl has no effect on spot counts (NaCl) and treatment with S1 nuclease (S1N(1), S1N(2), S1N(3)) diminishes spot counts. Each dot represents Cy5 counts from a field of view either before (red) incubation in buffer or nuclease or after (black) incubation in buffer or nuclease, and then (**e**) repeated with Cy5-$(GT)_6$-SWCNT as the substrate.

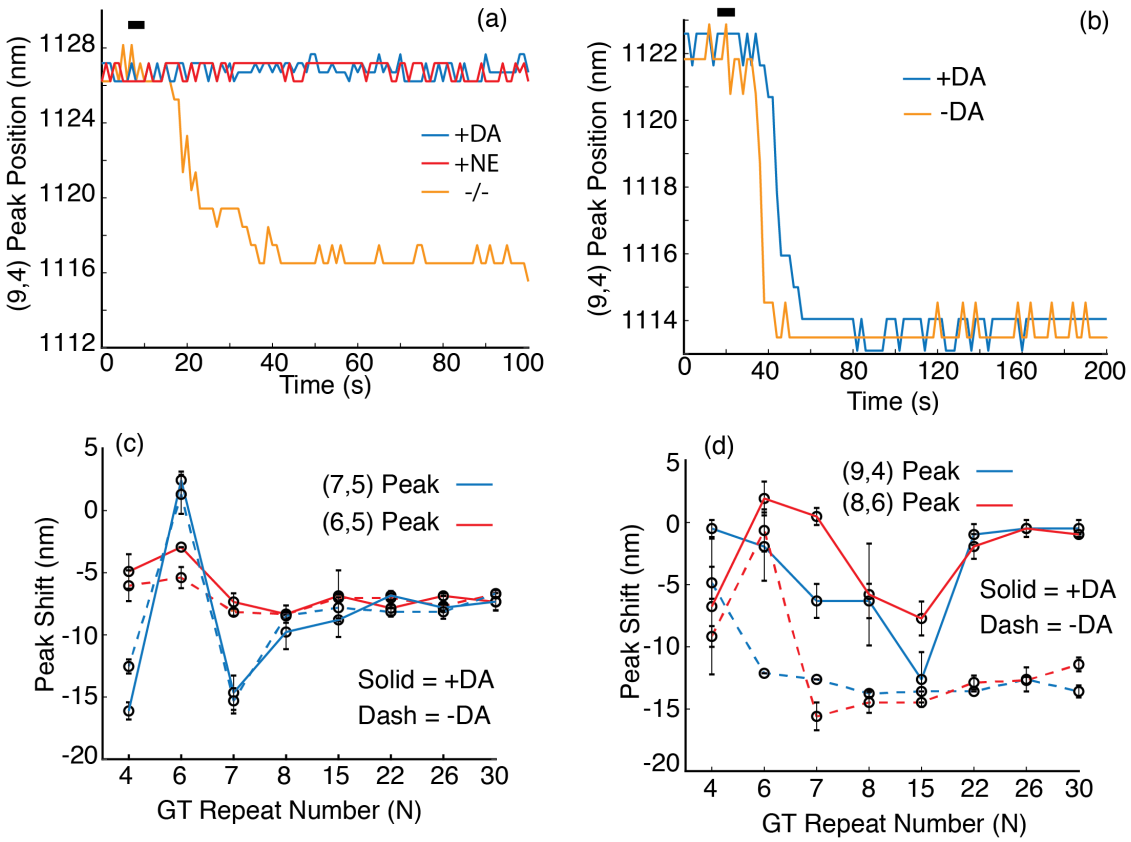

Figure 3.S10 Solvatochromic shifts induced by the addition SC surfactant to ssDNA-SWCNT constructs. (**a**) Shifts caused by 0.25 wt.% SC when no dopamine (DA) or norepinephrine (NE) is present (orange trace) is eliminated in the presence of 10 μM of DA (blue trace) and 10 μM of NE (red trace). Black bar indicates time of SC addition. (**b**) For C_{12}-SWCNT construct, incubation in 10 μM of DA does not eliminate shift caused by 0.25 wt.% SC (**c**) Peak shifts of the (6,5) and (7,5) chirality with DA (100 μM) (solid trace) and no DA (dash) show analyte induced corona stability is limited for smaller diameter SWCNTs, consistent with their diminished $\Delta F/F_0$ in response to DA. (**d**) On the other hand, bigger diameter peaks (9,4) and (8,6), which exhibit the strongest analyte mediated fluorescence modulation are strongly stabilized by the addition of DA. Peak shifts are computed by as the difference between steady-state (long time behavior) and initial peak positions. Final SC concentrations for (**c**) and (**d**) are 1 wt.%. Error bars are standard deviations from n=3 replicates.

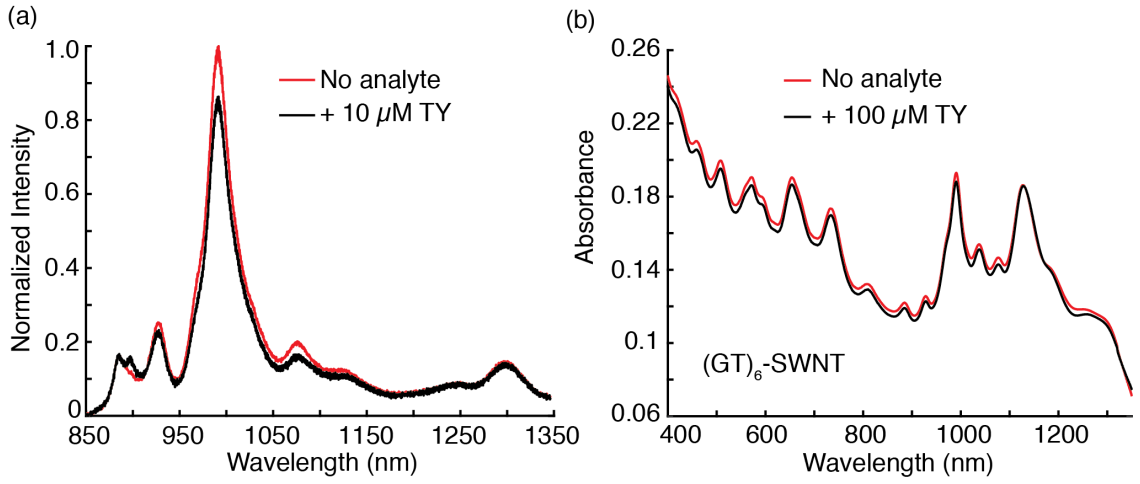

Figure 3.S11 (**a**) Fluorescence modulation of $(GT)_6$-SWCNT upon addition of p-tyramine (TY). Addition of 10 μM TY causes negligible fluorescence modulation of the $(GT)_6$-SWCNT construct. (**b**) Absorbance measurements before (red trace) and after (black trace) addition of 100 μM of TY. Negligible absorption modulations are observed in the E_{11} and E_{22} regions of the spectrum.

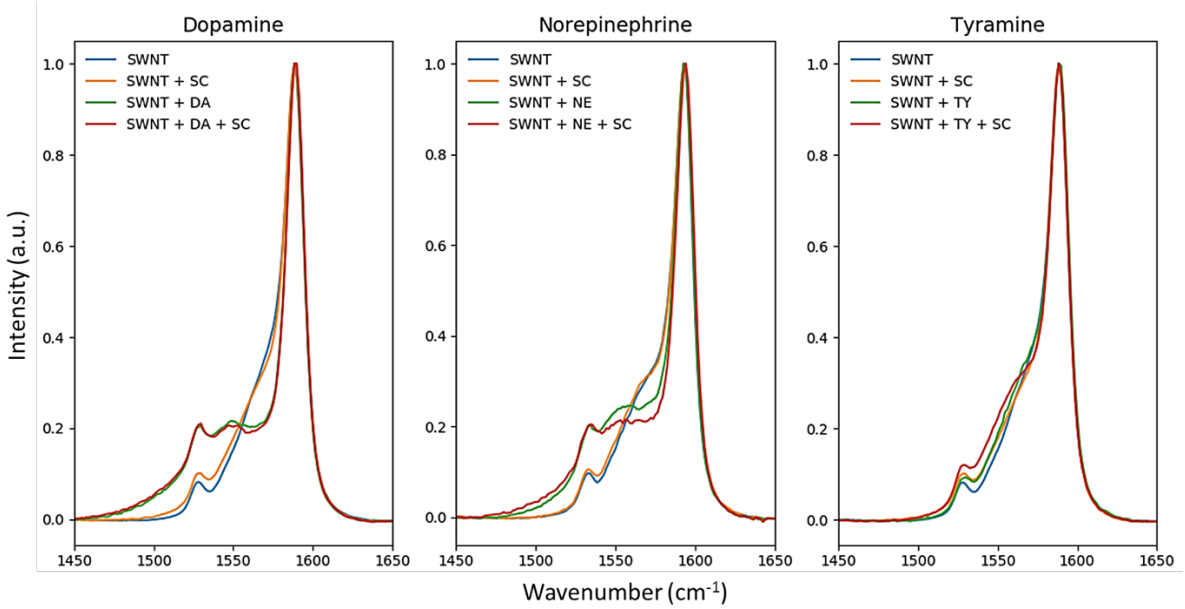

Figure 3.S12 Selective Raman peak broadening of $(GT)_6$-SWCNT by dopamine and norepinephrine. The effects on the Raman spectra for $(GT)_6$-SWCNT in the G-band region are shown for the addition three analytes. The blue spectra correspond to 20 mg/L of $(GT)_6$-SWCNT. Orange spectra contain 20 mg/L $(GT)_6$-SWCNT with sodium cholate (SC) added to 0.5 wt.%. Green spectra show $(GT)_6$-SWCNT with the respective analyte added to a final concentration of 100 μM after 1 minute of incubation. Both dopamine and norepinephrine produce a strong response in the G^- portion of the spectrum, which is absent from the tyramine measurements. The effect is maintained regardless of the subsequent addition of SC, suggesting the molecular recognition of dopamine and norepinephrine analytes disallows SC adsorption.

Chapter 4

Molecular Dynamics Simulations of $(GT)_N$ ssDNA Adsorbed on Single Wall Carbon Nanotubes

Portions of this chapter are reproduced with permission from Ref 51.[51] Copyright 2018. American Chemical Society.

In this chapter, we employed classical and quantum mechanical molecular dynamics simulations to rationalize key experimental observations from Chapter 3. Our calculations show that $(GT)_6$ ssDNA form ordered rings around (9,4) SWCNT, inducing periodic surface potentials that modulate exciton recombination lifetimes, thereby setting the photophysical behavior of the ssDNA-SWCNT hybrid structure. This ordered ring structure contrasts with helically adsorbed $(GT)_{15}$ ssDNA on (9,4) SWCNT. Further work elucidates how dopamine analyte binding modulates SWCNT fluorescence. We discuss the implications of our findings for SWCNT-based molecular imaging applications.

4.1 Introduction

Molecular dynamics (MD) simulations can provide key insights into complex systems that are otherwise difficult to probe experimentally. MD simulations generate atomic scale evolutions among a system of interacting particles by solving classical equations of motion and producing detailed movies of the whole system's evolution, either at atomic or domain-scale resolutions. MD simulations have previously been utilized to probe the energetic interactions of biomolecular complexes with single wall carbon nanotubes and have made considerable contributions in elucidating ssDNA conformations on the SWCNT surfaces.[86,87] In our work, we employed MD simulations to explore the self-assembly of $(GT)_6$ and $(GT)_{15}$ ssDNA on SWCNTs in order to gain insight into two key experimental observations we made from our work presented in Chapter 3. First, we sought to understand the photophysical processes that govern the relationship between fluorescence turn-on response and ssDNA sequence length, particularly with respect to the observed quenched baseline fluorescence of the $(GT)_6$-SWCNT hybrid. Second, we wanted to elucidate how molecular interactions between dopamine molecules and ssDNA-SWCNT hybrids generate perturbations that engender fluorescence modulation of the underlying SWCNT scaffold.

4.2 Results and Discussion

Towards this goal, we performed multiscale simulations of $(GT)_{(N=6,15)}$-(9,4)-SWCNT complexes to disclose mechanisms responsible for a strongly quenched baseline fluorescence and a large nanosensor response to neuromodulators observed in $(GT)_6$-SWCNT constructs, in contrast to $(GT)_{15}$-SWCNT. First, we equilibrated both $(GT)_6$-SWCNT and $(GT)_{15}$-SWCNT systems with atomistic molecular dynamics (MD) simulations. The $(GT)_{15}$ polymer, which was initially helically wrapped around the SWCNT consistent with

previous work,[86–90] remained in a helical conformation during a 200 ns MD simulation (Figure 4.1a). On the contrary, the $(GT)_6$ polymer on the (9,4) SWCNT rearranged from its initial helical conformation into a ring-like conformation in each of the five independent 200 ns trajectories performed, regardless of the handedness of the SWCNT simulated (Figure 4.1b, Figure 4.S8b, Figure 4.S9). The indifference to SWCNT handedness is in agreement with previous studies that show that recognition of chiral nanotubes by aromatic systems (graphene ribbons) can only be achieved at low temperatures (200 K) due to small energy differences of different adsorbed states.[91]

We further examined the adsorption of multiple – instead of singular – $(GT)_6$ polymers on the (9,4) SWCNT in a 250 ns long simulation. We observed helix-to-ring transitions in all $(GT)_6$ polymers (Figure 4.1b, Figure 4.S7b). The ring conformations of neighboring $(GT)_6$ ssDNAs become highly ordered throughout the simulation time course, as observed from the distinct sharp peaks positioned at approximately equal intervals of ~0.25 nm in the radial distribution function of DNA phosphate groups (Figure 4.S1). In contrast, $(GT)_6$ polymers adsorbed on the smaller diameter (6,5) SWCNT predominantly adopt a helical conformation in a 160 ns long simulation (Figure 4.S8a). Previous simulations of $(GT)_6$ polymers on (8,6)-SWCNT show that these polymers assume helical and elongated conformations along the SWCNT axis, in partial agreement with our results in Figure 4.1e.[92] However, the ring $(GT)_6$ motif is unique to this study. Differences between these studies may arise from differences in initialization, sampling times, the temperature range selected for the simulated systems, and the complexity of the system examined.[92]

To confirm that the ring-like conformation is a favorable adsorbed state of $(GT)_6$ on the (9,4) SWCNT, we calculated the free energy landscape of this ssDNA on the (9,4)-SWCNT surface at room temperature (T = 300 K) (Figure 4.1e), using replica exchange molecular dynamics (Methods in Appendix I).[90] The landscape reveals two distinct stable conformations for $(GT)_6$, a left-handed helix and a non-helical ring-like conformation, corresponding to free energy minima at (x,y) = (2.5 Å, -10 Å) and (3.2 Å, 6 Å), respectively, where x represents the root mean square deviations (RMSD) of the DNA structure with respect to the representative left-handed DNA helix, and y represents the distance along the long SWCNT axis of two selected atoms of the 3′- and 5′-end DNA nucleotides. These two conformations have approximately the same free energies, and as such they are expected to be equivalently sampled. Moreover, because the free energy barrier between each conformation is only ~1.2 kcal/mol, frequent interconversions between the two conformations is likely at room temperature for single or sparsely adsorbed polymers. However, in experimental suspensions, SWCNT surface is likely to be covered by multiple ssDNA polymers. In that case, the ring-like ssDNA conformations are likely to be more prevalent over the helical conformation due to steric hindrance, as the ring-like polymer packing structure provides better ssDNA surface packing on the SWCNT. We suggest that the ring-like ssDNA conformation is likely enhanced by the fact that the $(GT)_6$ contour length matches the circumference of the (9,4) SWCNT, affording ordered self-assembly of the oligonucleotides on the SWCNT surface. On the other hand, the polymer length-SWCNT circumference mismatch between $(GT)_6$ and the (6,5) SWCNT species renders the ring configuration less likely and favors a helical conformation (Figure 4.S8a). The free energy landscape in Figure 4.1e also reveals the existence of several local minima, whose associated structures are shown in Figure 4.S10. However, these local minima have higher free energies

than the two structures shown in Figure 4.1e and are likely to be sampled less frequently by the $(GT)_6$ polymer.

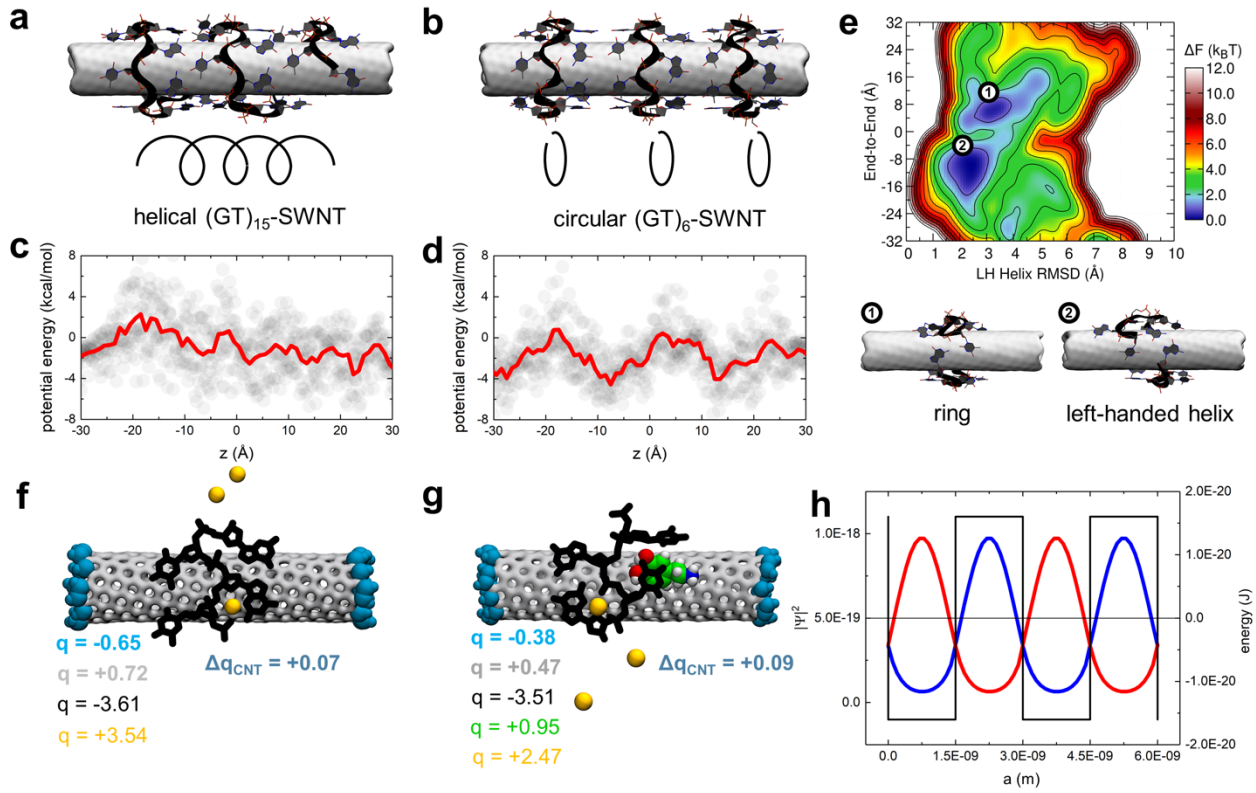

Figure 4.1 Computational modeling of ssDNA-SWCNT nanosensor complexes. (a) Representative conformation of $(GT)_{15}$-SWCNT. SWCNT is depicted as a gray surface, $(GT)_{15}$ and its backbone are shown in licorice and black ribbon representations, and ssDNA atoms are shown in gray (C), red (O), blue (N), and orange (P). **(b)** Representative conformation of $(GT)_6$-SWCNT, containing three $(GT)_6$ polymers. The color scheme is the same as in panel a. **(c)** Electrostatic potential energy profile at the SWCNT surface in the $(GT)_{15}$-SWCNT system as a function of SWCNT axial length. The profile is averaged over 2 ns and over the radial SWCNT dimension and includes the effects of the complete SWCNT environment present in MD simulations (ssDNA, water, and ions). **(d)** Electrostatic potential energy profile at the SWCNT surface for the $(GT)_6$-SWCNT system plotted as a function of SWCNT axial length. **(e)** Free energy landscape of $(GT)_6$-SWCNT at 300 K. The structures corresponding to two free energy minima are labeled by indices 1 and 2. **(f)** Net charges of molecular fragments in the $(GT)_2$-SWCNT system, evaluated in quantum mechanical calculations. **(g)** Net charges of molecular fragments in the $(GT)_2$-SWCNT system with an adsorbed dopamine molecule, evaluated in quantum mechanical calculations. The color scheme in panels f and g: black (DNA), silver (non-terminal SWCNT atoms), blue surface (terminal -CH groups capping the SWCNT), yellow (sodium ions), green, blue, red and white spheres (C, N, O and H atoms on dopamine). **(h)** Electron (red) and hole (blue) probability densities in a Kronig-Penney potential (Methods in Appendix I). Probability density values are labeled on the left axis, and the values associated with the potential energy well are labeled on the right axis.

Since the charged $(GT)_6$ and $(GT)_{15}$ polymers have different conformations on the (9,4) SWCNT, we reasoned that they should create electrostatic potentials of different profiles close to the SWCNT surface. To investigate this phenomenon, we calculated the average electrostatic potential at the SWCNT surface generated by all molecules in the system (ssDNA, water, and ions, including the Na^+ cations adsorbed over long timescales

within ssDNA pockets) (Figures 4.S2 and Figure 4.S3). $(GT)_{15}$ creates regions of negative and positive electrostatic potential under the polymer as a 'footprint', which extend ~4 nm in contiguous length and roughly follow the ssDNA helical pattern (Figure 4.2a, 4.2b). Negative potential pockets are primarily beneath guanine nucleotides, while positive pockets occur beneath thymine nucleotides. When averaged over the radial SWCNT dimension, as shown in Figure 4.1c, the electrostatic potential profile at the SWCNT surface under $(GT)_{15}$ is roughly constant across the entire helix, with random fluctuations. The electrostatic potential around SWCNT with adsorbed $(GT)_6$ rings also follows the polymer, which results in distinct ring-like regions of alternating positive and negative potentials along the SWCNT axis, where each contiguous electrostatic pocket is ~1.5 nm in length (Figure 4.2c, 4.2d). In contrast to $(GT)_{15}$-SWCNT, when averaged over the radial SWCNT dimension, these electrostatic potentials exhibit large periodic oscillations across multiple rings (Figure 4.1d). We posit that from the perspective of exciton confinement in the SWCNT quasi-1D structure, these periodic electrostatic potentials created by the (GT)6 rings effectively form a superlattice (Figure 4.1d).

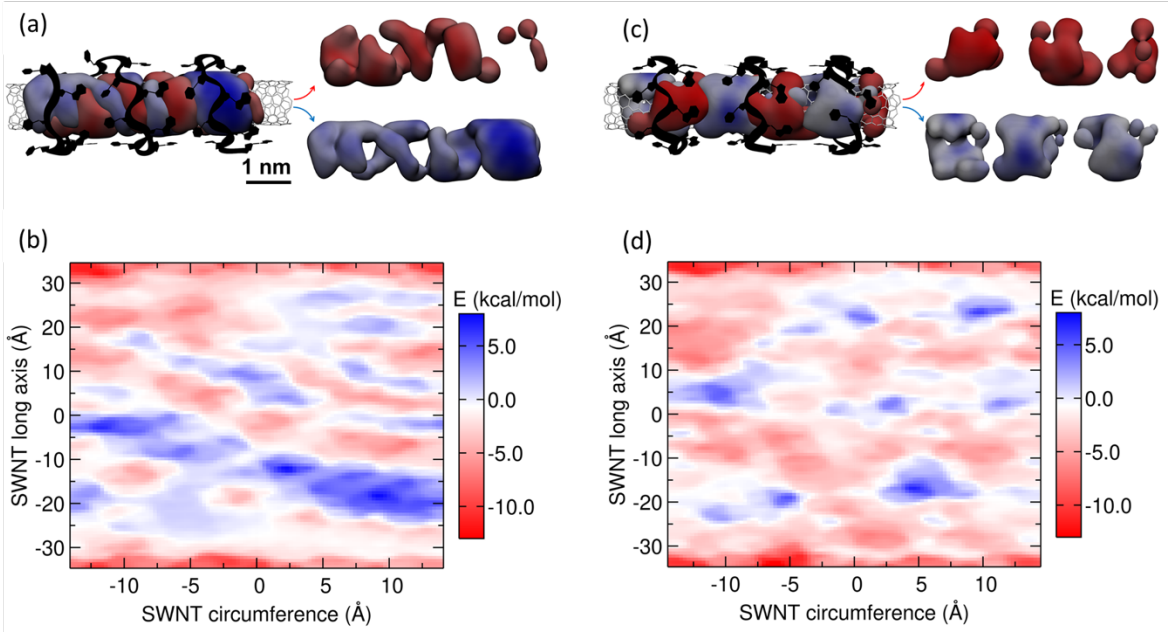

Figure 4.2 Electrostatic potential pattern at the SWCNT surface induced by adsorbed ssDNA moieties (**a**) The extended electrostatic potential pattern at the SWCNT surface of the $(GT)_{15}$-SWCNT system. Red and blue regions represent negative and positive potential domains, respectively. For clarity, isolated positive and negative regions are shown separately on the right. (**b**) Plot of the complete potential energy surface at the SWCNT for the system shown in panel a. (**c**) The localized potential pattern at the SWCNT surface of the $(GT)_6$-SWCNT system. The color scheme is as in panel a. (**d**) Plot of the potential energy surface at the SWCNT for the system shown in panel c.

Next, quantum mechanics/molecular dynamics (QM/MD) calculations were performed to better understand exciton relaxation in the (GT)6-(9,4)-SWCNT conjugates (Figure 4.S4). The SWCNT is polarized by the presence of the charged DNA polymer, with overall partial positive charges on the SWCNT surface covered with ssDNA, and partial

negative charges at the SWCNT ends (Figure 4.1f). This charge distribution can be seen as an effective doping of the SWCNT, affecting the exciton relaxation processes. In QM/MD calculations, we observed a relatively small charge transfer between ssDNA and SWCNT (Figure 4.1f, Table 4.S1). Dopamine adsorption on the DNA-wrapped SWCNT slightly decreased the SWCNT polarization (Figure 4.1g and Table 4.S2). However, this effect is only local, and if the molarity of adsorbed dopamine molecules is low, it is unlikely to effectively alter the polarizability of a large $(GT)_6$ -SWCNT complex (Figure 4.S5, Figure 4.S6). Conversely, adsorption of dopamine molecules is capable of locally perturbing the periodic electrostatic potential, which can influence SWCNT photoluminescence, as we discussed below.

These MD and QM/MD results provide insight into possible relaxation pathways of excitons in the $(GT)_N$-SWCNT complexes with and without adsorbed dopamine analyte molecules. We thus propose the following mechanisms to explain the strong turn-on response of $(GT)_6$-SWCNT nanosensors to dopamine: (i) SWCNT polarization induced by the adsorption of multiple $(GT)_6$ polymers can give rise to non-radiative exciton relaxation mechanisms, because effective doping activates phonon-assisted relaxation channels for SWCNT excitons, as has been suggested in previous studies. [93,94] (ii) At the same time, radiative exciton relaxation in a $(GT)_6$-(9,4)-SWCNT complex is expected to be significantly suppressed by the presence of closely-spaced periodic potentials of multiple $(GT)_6$ strands (Figure 4.1d, 4.2c). In positive and negative regions of this potential, the electron and hole wave function components tend to avoid each other (Figure 4.1h), which results in a significant cancelation of their overlap integral present in the oscillator strength. (iii) However, in the presence of adsorbed dopamine molecules, the cancellation of the overlap integral can be disturbed because dopamine induces a disordered superlattice (Figure 4.S7a). Therefore, radiative transitions can become active simultaneously with the non-radiative transitions, giving rise to a fluorescent turn-on nanosensor. Adsorbed dopamine molecules may result in marginal reduction in SWCNT polarization and reduce the effective doping caused by the adsorbed $(GT)_6$ rings. However, our work suggests that this mechanism is unlikely to contribute significantly to the turn-on response. We further attribute the SWCNT-diameter dependence of the strong turn-on response (Figure 3.1e, Figure 3.S2) to two phenomena: (i) doping-induced quenching of SWCNT photoluminescence becomes more efficient with increasing SWCNT diameter[93,94] and (ii) the ordered periodic superlattice formed by $(GT)_{4\text{-}8}$ is less likely to occur on smaller diameter SWCNTs (Figure 4.S8).

4.3 Conclusion

In Chapter 3, we reported $(GT)_6$-SWCNT as a strong turn-on optical reporter for the neuromodulators dopamine and norepinephrine, with a dynamic range compatible with applications for *in vivo* neurochemical investigations. In this chapter, we investigated the photophysical and molecular underpinnings of this strong and selective turn-on response computationally. We employed multi-scale molecular dynamics computational approaches to rationalize several experimental findings. We find that the self-assembly of $(GT)_6$ ssDNA on the SWCNT surface produces highly ordered ring structures, which effectively dopes the SWCNT through polarization and forms a superlattice from the perspective of a 1-D confined

SWCNT exciton. The effective doping activates exciton non-radiative transitions, while the periodic potential suppresses their radiative relaxation. The baseline SWCNT fluorescence, dimmed in this manner, is enhanced by an analyte that binds selectively to the SWCNT surface-adsorbed polymer and perturbs the superlattice to promote a competitive radiative relaxation. These insights and results have important implications for the development of nanosensors for specific biomolecular analytes of interest, for tuning the dynamic range of those already developed, and for orthogonal fields of research such as SWCNT purification by chiral index and photovoltaics.

4.4 Appendix I

Materials and Methods

Molecular dynamics simulations

Atomistic simulations were conducted to investigate ssDNA-SWCNT nanosensors with and without added dopamine analyte. In all simulations, conjugates of (9,4) SWCNT with $(GT)_{15}$ and $(GT)_6$ polymers were prepared. (9,4) SWCNT segments, 39 Å or 66.73 Å in length, were built in VMD.[95] Conjugates of $(GT)_6$ polymers with two other SWCNTs were also examined. An analogous (9,4) SWCNT segment of the opposite handedness, also 39 Å in length, was built by transforming the initially built (9,4) SWCNT into its mirror image. Separately, a (6,5) SWCNT, 53 Å in length, was built in VMD.[95] The initial configurations of $(GT)_{15}$ and $(GT)_6$ ssDNA polymers were built in Material Studio with nucleotides arranged to form helical conformations with radii several Ångstroms wider than the radius of the (9,4) SWCNT. The helical DNAs were positioned to wrap SWCNTs, with ssDNA bases not pre-adsorbed on the SWCNTs surfaces. The length of the SWCNT was selected to result in optimal SWCNT surface coverage by the adsorbed $(GT)_{15}$ ssDNA via base stacking, which prevents excessive lateral ssDNA diffusion on SWCNT. The prepared ssDNA-SWCNT conjugates were solvated with TIP3P water and neutralized with 0.1 M NaCl with solvate and ionize VMD plugins, respectively.[95] In simulations of DNA-SWCNT conjugates with dopamine, two dopamine molecules were placed ~10 Å away from SWCNTs into pre-relaxed systems prepared without dopamine. The final systems contained approximately 11,000 atoms.

The systems were described with CHARMM36 and CHARMM general force field (dopamine) parameters.[96–98] MD simulations were performed with NAMD2.11 package.[99] All simulations were conducted with Langevin dynamics (Langevin constant γLang = 1.0 ps^{-1}) in the NpT ensemble, where temperature and pressure remained constant at 310 K and 1 bar, respectively. The particle-mesh Ewald (PME) method was used to calculate Coulomb interaction energies, with periodic boundary conditions applied in all directions.[100] The time step was set to 2.0 fs. The evaluation of long range van der Waals and Coulombic interactions was performed every 1 and 2 time steps, respectively. After 1,000 steps of minimization, solvent molecules were equilibrated for 2 ns around the DNA and SWCNTs, which were restrained using harmonic forces with a spring constant of 1 kcal/(mol $Å^2$). Next, the systems were equilibrated in 250 ns production MD runs, with restraints applied only on the edge SWCNT atoms.

To analyze the electrostatic potential created by the surroundings at the SWCNT surface, we computed potential energy maps at SWCNT surfaces for several configurations

of DNA-wrapped SWCNTs. In each configuration, selected from equilibration MD trajectories, SWCNT and DNA atoms were restrained with a hard (1.0 kcal/mol/Å^2) and soft (0.1 kcal/mol/Å^2) harmonic restraint, respectively, and simulated for 1 ns. We evaluated the potential energy map at the SWCNT surface by averaging electrostatic potential energy contributions and Lennard-Jones contributions from 1 ns simulations of restrained systems. The electrostatic potential energy of each SWCNT atom was computed by setting its charge to q = −1e for the purpose of evaluating the electrostatic potential energy (in 1 ns simulations, each atom had the charge q = 0). The average potential energy of each carbon atom in its environment was evaluated with the NAMDEnergy plugin in VMD (each 1 ns trajectory resulted in 500 potential energy data points).[95]

Free energy calculations

The free energy landscape (Figure 4.1e) was obtained through replica exchange MD (REMD) simulation of a $(GT)_6$-SWCNT system solvated in 3.63 × 3.63 × 4.92 nm^3 box, containing 6,605 atoms. The box contained 1,881 water molecules, modeled using TIP3P model. In addition to Na^+ counterions neutralizing the system, 36 Na^+ and Cl^- ions were included to match the physiological salt concentration in the experimental system. Periodic boundary conditions were imposed in all dimensions, and PME method was used to calculate long-range electrostatics. Additionally, both ends of SWCNT were in contact with their periodic images. Energy minimization and 100 ps of heating (NVT) were performed to reach the starting temperature of 310 K. To perform REMD simulations in NVT ensemble, 54 replicas and a 290-727.4 K temperature range were chosen to maintain exchange acceptance ratios around 25% with 2 ps exchange time. The total REMD simulation time was 54 × 270 ns (per replica) = 14.58 μs. The simulation time step was 2 fs and trajectories were extracted every 2 ps. Therefore, 135,000 configurations per replica were collected. The last 80,000 (160 ns) configurations of room temperature replica were analyzed to obtain the free energy landscape.

To generate the free energy landscape shown in Figure 4.1e, two independent order parameters of the (GT)6 structure were calculated from the obtained system configurations: 1) end-to-end distance of DNA polymer (the z-distance between centers of mass of the first guanine and last thymine residues; z coordinate aligns with the long axis of the CNT); and 2) Root mean square deviation (RMSD) of phosphorous atoms of the DNA backbone, compared to the configuration these atoms have in the ideal left-handed helix of $(GT)_6$ wrapping SWCNT. The probability distribution function ($P(x, y)$) of these two order parameters were calculated and combined to generate free energy ($\Delta F(x, y)$) according to the formula:

$$\frac{\Delta F(x,y)}{k_B T} = -\ln\left(\frac{P(x,y)}{P_{max}}\right)$$

In above formula, P_{max} is the maximum value of $P(x, y)$. Figure 4.1e was obtained at 300 K by calculating two-dimensional free energy landscape according to the above formula, where x and y represent end-to-end distance and the RMSD of left-helix ssDNA wrapping CNT, respectively.

QM/MD simulations

Quantum mechanics/molecular dynamics (QM/MD) simulations were performed for systems containing SWCNT, $(GT)_2$ DNA, Na^+ counterions, with or without dopamine, all described quantum mechanically, and TIP3P water, described classically. The systems examined on the QM/MD level were extracted from the well-equilibrated classical MD simulation of the $(GT)_6$–SWCNT system with dopamine trapped in binding site 2 (Figure 4.S6). Since $(GT)_6$ can stably host Na^+ ions, separate simulations were performed for the systems with and without the hosted Na^+ ions. All extracted systems were solvated and equilibrated in 2 ns classical MD simulations, where all species, except water, were restrained with the harmonic restraint (1.0 kcal/mol/Å^2). The initial configurations of QM/MD simulations were obtained from the final configurations of the above classical MD simulations, in which the water box was cut into a sphere of 28 Å radius.

The QM/MD simulations were performed using TeraChem software (Terachem). The quantum parts of the system were described at the ωB97X/6-31G** level, with dispersion corrections (DFT-D2).[101,102] We used an X-matrix tolerance of 10^{-4}, and a wave function convergence threshold of 10^{-4}. The MD simulations were performed at T = 310 K, using the Langevin dynamics with a damping coefficient of γLang = 1 ps−1 and a time step of 1 fs. No periodic boundary conditions were used; the system was simulated within a water droplet (Figure 4.S4). Atomic charges of the quantum parts of the systems were calculated using the Mulliken population analysis.

Electron and hole wavefunctions in periodic square wells

To approximate the effect of periodic potentials along the SWCNT surface on the exciton relaxation, we examined the behavior of negatively (electrons) and positively (holes) charged particles' wavefunctions in periodic square wells, using the Kronig-Penney model. Figure 4.1h plots the probability densities of electrons and holes (squared wavefunctions). The periodic energy wells are centered at 0 J and their valleys and peaks occur at – 1.602 x 10^{-20} J and 1.602 x 10^{-20} J, respectively, to roughly match the periodic potential energies created at the SWCNT surface by the ring $(GT)_6$ ssDNAs. The wavefunction energies were chosen as – 0.641 x 10^{-20} J. The periodic square wells are 1.5 nm in length, also matching the periodic potential shape created by the ring DNAs.

4.5 Appendix II

Supporting Information

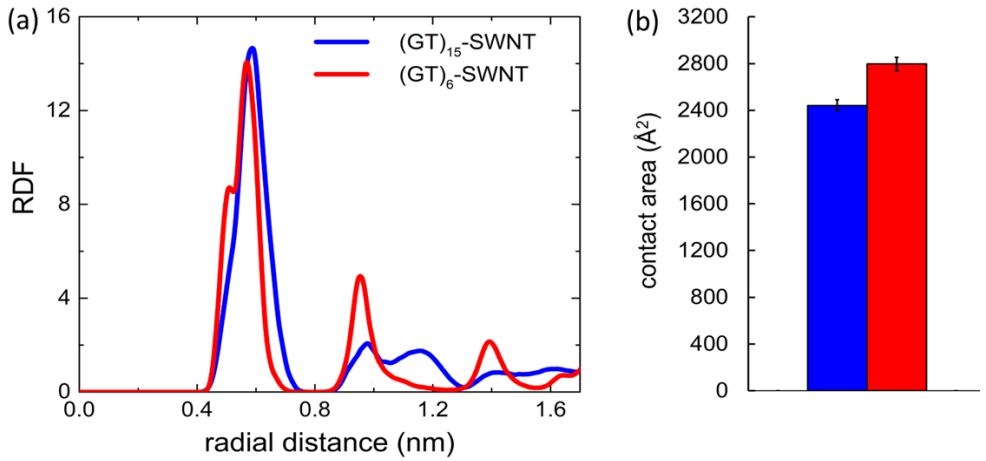

Figure 4.S1 DNA distribution and surface coverage on SWCNTs. (**a**) Radial distribution functions of phosphate groups (P-atom) of $(GT)_{15}$ and $(GT)_6$ DNAs on SWCNTs, calculated for the last 100 ns of simulations. (**b**) Contact areas between DNA strands and SWCNTs, averaged over the last 100 ns of simulations.

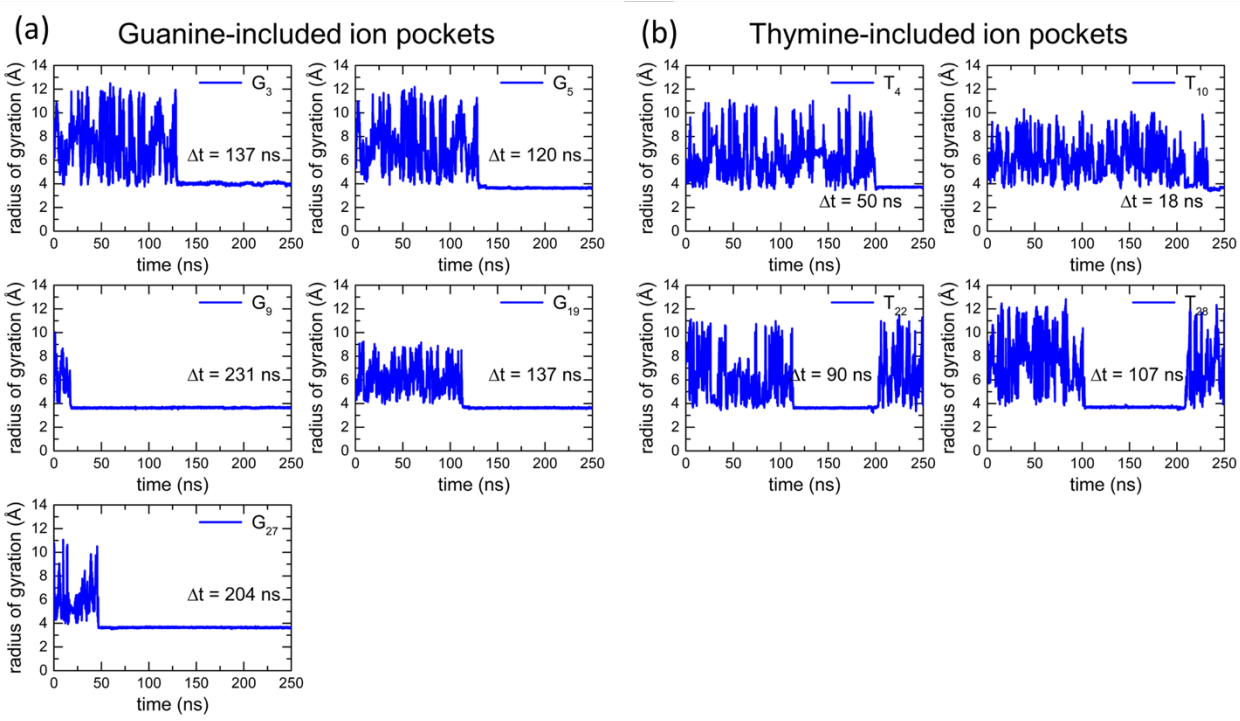

Figure 4.S2 Residence times of Na^+ ions hosted by $(GT)_{15}$ DNAs. (**a**) Residence times of Na^+ ions hosted by guanine (**a**) and thymine (**b**) nucleotides of $(GT)_{15}$ DNA on (9,4) SWCNT. The residence times were calculated based on radii of gyration of selected nucleotide atoms and trapped Na^+ ions.

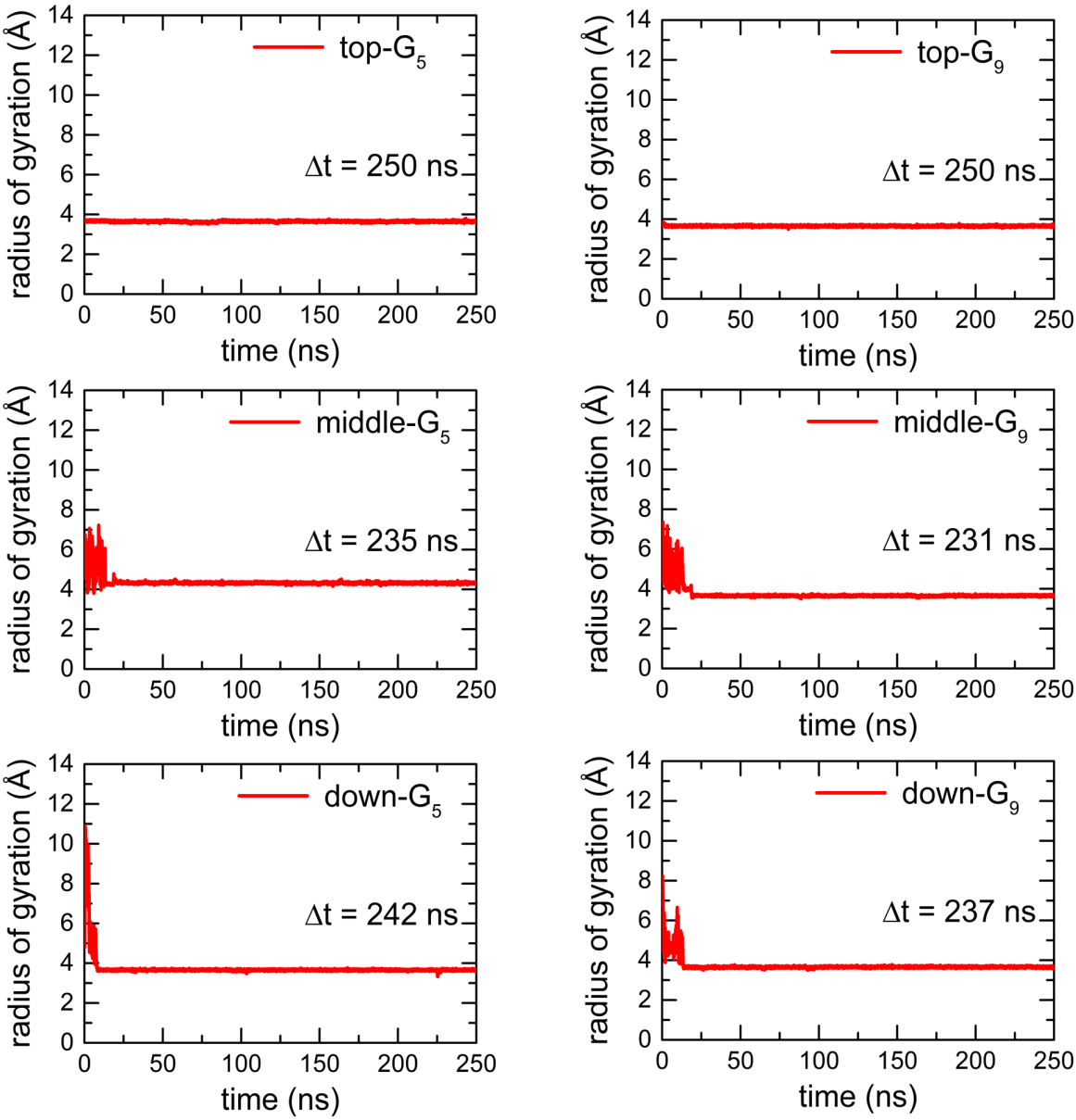

Figure 4.S3 Residence times of Na^+ ions hosted by $(GT)_6$ DNAs. Residence times of Na^+ ions hosted by guanine nucleotides of $(GT)_6$ DNA on (9,4) SWCNT. Guanine residues 5 and 9 of every single $(GT)_6$ strand on SWCNT hosted Na^+ ions (the system analyzed is shown in Figure 3, and top, middle and down refers to three $(GT)_6$ strands). The residence times were calculated as in Figure S9.

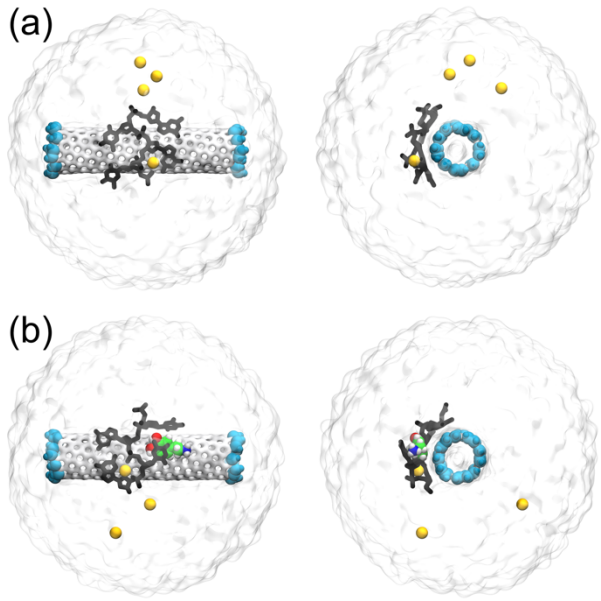

Figure 4.S4 Representative systems examined in QM/MD simulations. (**a**) $(GT)_2$–SWCNT system with one hosted Na^+ ion and three solution Na^+ ions. (**b**) Dopamine (binding site 2) in the $(GT)_2$–SWCNT system, containing three solution Na^+ ions. Classically described water in the system is shown as a transparent surface. The atoms in the system are shown in yellow (Na), silver (non-terminal SWCNT atoms), black (atoms of nucleotides), blue surface (terminal -CH groups capping the SWCNT), green (carbon atoms of dopamine), red (O), dark blue (N), orange (P) and white (H).

	systems	Middle-carbons	Edges-carbons	whole SWNT	Nucleic Acid	Na	Cl	Total
6-31g** basis set	SWNT	+0.35	-0.35	0	-	-	-	0
	SWNT-Na	+0.59	-0.59	0	-	+1	-	+1
	SWNT-Cl	+0.67	-0.67	0	-	-	-1	-1
	SWNT-Na-Cl	+0.81	-0.81	0	-	+1	-1	0
	SWNT-G-non-hosted	+0.77	-0.75	+0.02	-1.02	+1	-	0
	SWNT-G-hosted	+0.69	-0.66	+0.03	-0.76	+0.73	-	0
	SWNT-T-non-hosted	+0.293	-0.258	0.035	-1.035	+1	-	0
	SWNT-T-hosted	+1.05	-1.02	+0.03	-0.90	+0.87	-	0
	SWNT-GT2 (only one-hosted Na)	+0.724	-0.648	+0.076	-3.615 (4 phosphate groups)	3.539	-	0

Table 4.S1. Net charges of different parts of SWCNT, SWCNT-ion, and SWCNT-DNA systems, described in quantum mechanical calculations. The charge is reported in units of *e*, the unit charge. All systems had SWCNT, ions, and DNA described quantum mechanically, and the water described classically. The calculation details are described in the Methods in Appendix I.

6-31g** basis set	systems	Middle-carbons	Edges-carbons	whole SWNT	Nucleic Acid	DOP	Na	Total
	SWNT-GT2 (only one-hosted Na)	+0.724	-0.648	+0.076	-3.615	-	3.539	0
	SWNT-DOP	+0.28	-0.26	+0.02	-	+0.98	-	+1
	SWNT-DOP-GT2 (**sandwich site** and only one-hosted-Na)	+0.466	-0.383	+0.083	-3.506	+0.950	+2.473	0
	SWNT-no-DOP-GT2 (**Dopamine was removed** and only one-hosted-Na)	+0.596	-0.513	+0.083	-3.583	0	+3.500	0

Table 4.S2. Net charges of different parts of SWCNT-DNA systems with and without the dopamine molecule, described in quantum mechanical calculations. All the systems had SWCNT, ions, DNA, and dopamine (when present) described quantum mechanically, and the water described classically. The dopamine binding site examined is the binding site 2 of the $(GT)_6$-SWCNT system, shown in Figure. S6b.

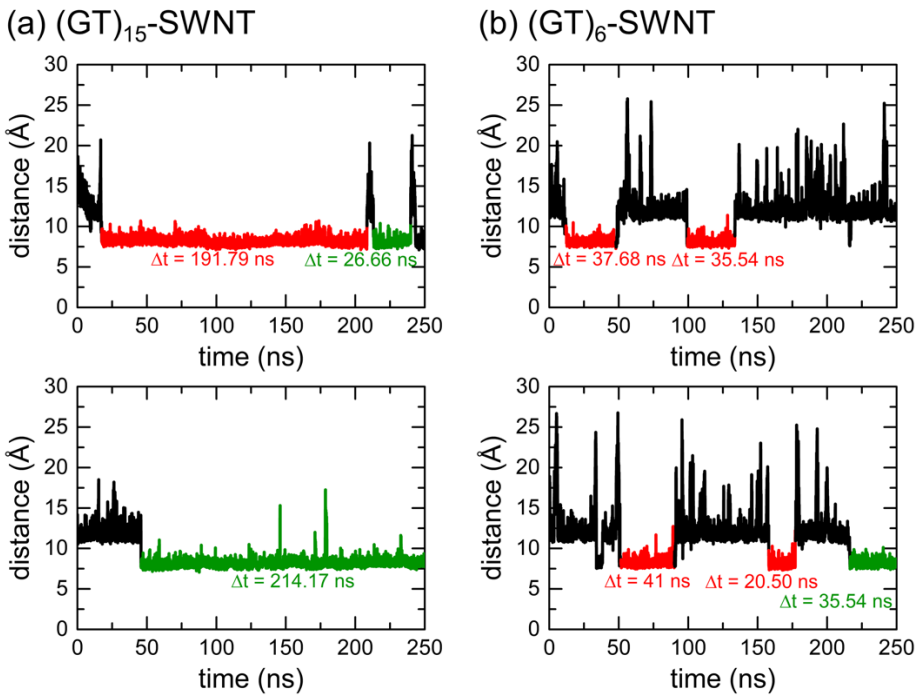

Figure 4.S5 Residence times of dopamine molecules in their binding sites. (**a**) Residence times of dopamine in $(GT)_{15}$-SWCNT systems in binding sites (red) 1 and 2 (green). (**b**) Residence times of dopamine in $(GT)_6$-SWCNT systems in binding sites 1 (red) and 2 (green). Residence times were calculated by tracking the radial distance between the dopamine ring center of mass and the central axis of SWCNT. Dopamine binds more stably to $(GT)_{15}$ than to $(GT)_6$.

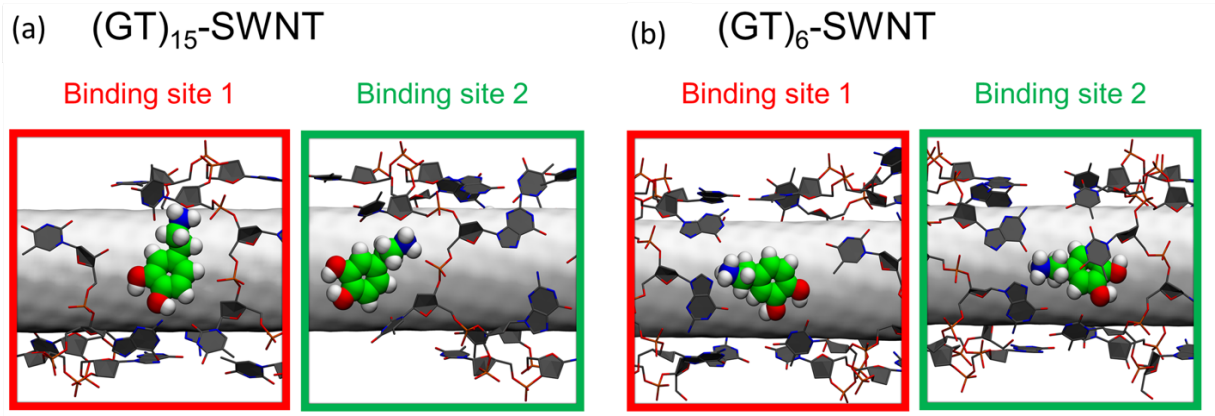

Figure 4.S6 Dopamine binding to DNA-SWCNT systems. Two representative binding poses of dopamine (**a**) in the $(GT)_{15}$-SWCNT system and (**b**) in the $(GT)_6$-SWCNT system. Atoms of dopamine are shown in green (C), red (O), blue (N), and white (H). Dopamine opens a space between consecutive bases of $(GT)_{15}$ and binds with its amine group to the DNA phosphate. The helical arrangement of nucleotides in $(GT)_{15}$ allows for the opening of consecutive bases and dopamine insertion. Conversely, the ring arrangement of $(GT)_6$ nucleotides prevents spreading of consecutive nucleotides (which would allow dopamine insertion), and dopamine primarily interacts with bases of neighboring $(GT)_6$ strands in a bridge-like binding mode.

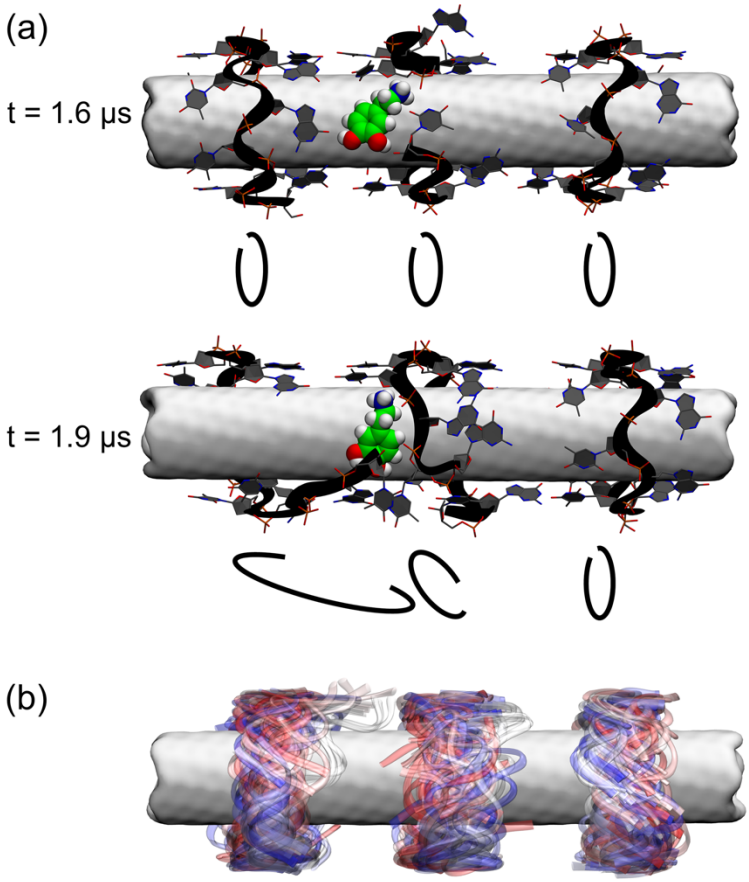

Figure 4.S7 Adsorption of dopamine to $(GT)_6$. (**a**) $(GT)_6$ ring structures become distorted due to dopamine adsorption. Two snapshots of dopamine adsorbed to $(GT)_6$-wrapped SWCNTs, after 1.6 μs and 1.9 μs of a classical MD simulation. $(GT)_6$ ring structures become distorted due to the presence of dopamine after 1.9 μs. (**b**) $(GT)_6$ polymers mainly preserve ring structures in a 4.6 μs long MD simulation. $(GT)_6$ rings occasionally convert to helical conformations, followed by returns to the ring conformations; the largest changes from ring conformations are observed when DNA strands interact directly with dopamine. The backbones of three $(GT)_6$ strands are shown over the course of a 4.6 μs long MD simulation; snapshots were selected every 50 ns. Blue, white, and red colors of the $(GT)_6$ backbone snapshots represent the beginning, the middle and the end of the trajectory.

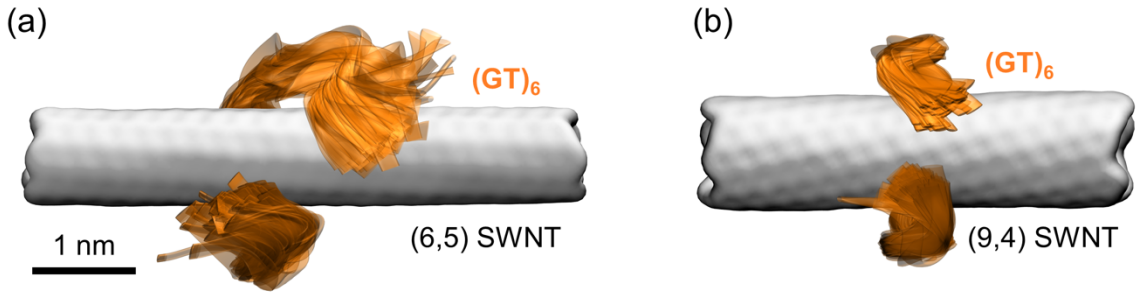

Figure 4.S8 MD simulations of $(GT)_6$ polymers complexed with SWCNTs of different diameter and handedness. (**a**) Conformations of a $(GT)_6$ polymer on a (6,5) SWCNT. The $(GT)_6$ strand predominantly adopts a helical conformation. (**b**) Conformations of a $(GT)_6$ strand on a (9,4) SWCNT of an opposite handedness than the (9,4) SWCNT explored in Figure 3. The $(GT)_6$ strand predominantly adopts ring-like conformations. SWCNTs are shown as gray surfaces, backbones of $(GT)_6$ strand are shown as orange ribbons. Backbones of $(GT)_6$ are aligned, and 80 conformations, assumed every 2 ns in MD simulations, are overlaid. The conformations shown represent the dynamics of $(GT)_6$ in 160 ns MD trajectories.

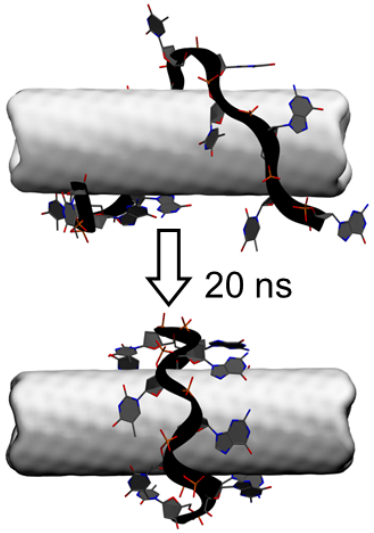

Figure 4.S9 $(GT)_6$ spontaneously assumes a ring-like conformation on a (9,4) SWCNT in five independent 200 ns long MD simulations.

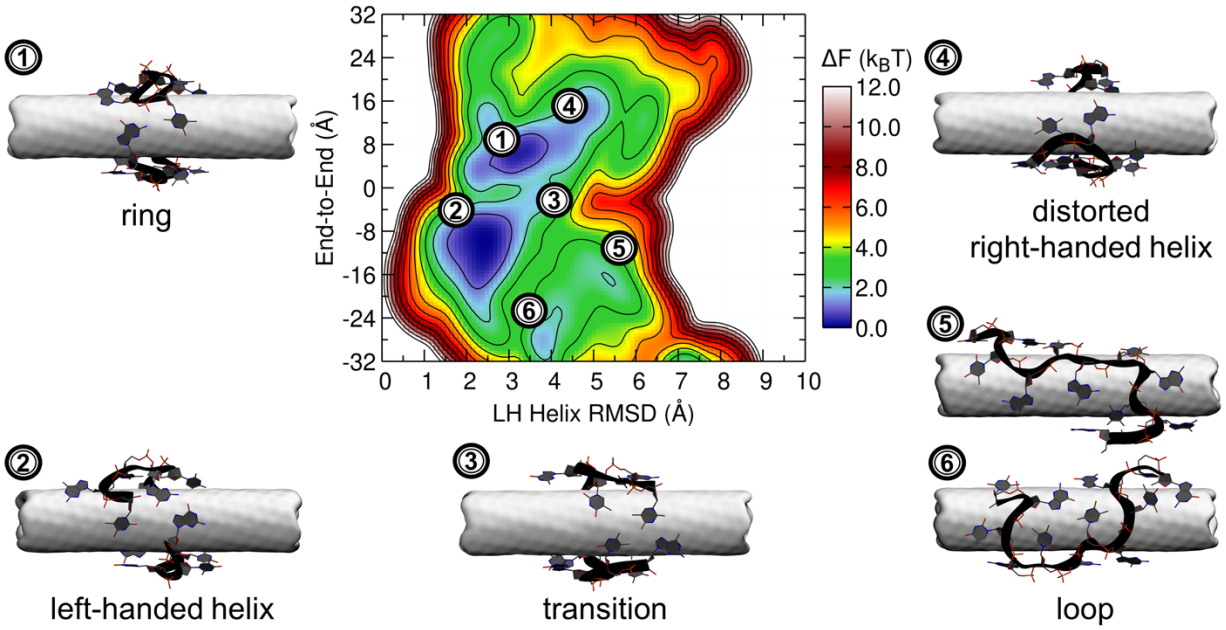

Figure 4.S10 Free energy landscape of $(GT)_6$-SWCNT at 300 K on the (9,4) SWCNT species. The conformations associated with various free energy minima and a transition state are labeled by indices 1-6. The state labeled by index 3 marks the transition state between free energy minima labeled by indices 1 and 2.

Chapter 5

Imaging Striatal Dopamine Release Using a Single Wall Carbon Nanotube-Based Fluorescent Catecholamine Indicator

Neuromodulation plays a critical role in brain function in both health and disease. New optical tools are needed that can image neuromodulation with high spatial and temporal resolution, which will add an important new dimension of information to neuroscience research. Here, we demonstrate the use of a catecholamine nanosensor with fluorescent emission in the 1000-1300 nm near-infrared window to measure dopamine transmission in brain tissue. These near-infrared catecholamine nanosensors (nIRCats) represent a broader class of nanosensors that can be synthesized from non-covalent conjugation of single wall carbon nanotubes (SWCNT) with single strand oligonucleotides. We show that nIRCats can be used to detect catecholamine efflux in brain tissue driven by both electrical stimulation or optogenetic stimulation. Spatial analysis of electrically-evoked signals revealed dynamic regions of interest approximately 2 microns in size in which transients scaled with simulation intensity. Optogenetic stimulation of dopaminergic terminals produced similar transients, whereas optogenetic stimulation of glutamatergic terminals showed no effect on nIRCat signal. Bath application of nomifensine prolonged nIRCat fluorescence signal, consistent with reuptake blockade of dopamine. We further show that the chemically synthetic molecular recognition elements of nIRCats permit measurement of dopamine dynamics in the presence of dopamine D2 receptor agonists and antagonists which revealed heterogeneity in D2 autoreceptor modulation of presynaptic dopamine release. These nIRCat nanosensors are advantageous because i) they do not require gene delivery or protein expression, ii) their near-infrared fluorescence facilitates imaging in optically scattering brain tissue and is compatible for use in conjunction with other optical neuroscience tool sets, iii) the broad availability of unique near-infrared colors have the potential for simultaneous detection of multiple neurochemical signals, and iv) they are compatible with pharmacology. Together, these data suggest nIRCats and other nanosensors of this class can serve as versatile new optical tools to report dynamics of extracellular neuromodulation in brain tissue.

5.1 Introduction

The catecholamines dopamine and norepinephrine are neuromodulators known to play an important role in learning and attention and are implicated in multiple brain disorders. [104–108] Dopamine, in particular, is thought to play a critical role in learning[109], motivation [110,111], and motor control [112], and aberrations in dopamine neurotransmission are implicated in a wide range of neurological and psychiatric disorders including Parkinson's disease [113], schizophrenia [114], and addiction. [115]

Modulatory neurotransmission is thought to occur on a broader spatial scale than classic neurotransmission, the latter of which is largely mediated by synaptic release of the amino acids glutamate and γ-aminobutyric acid (GABA) in the central nervous system. In synaptic glutamatergic and GABAergic neurotransmission, neurotransmitter concentrations briefly rise in the synaptic cleft to mediate local communication between the pre- and postsynaptic neurons through the rapid activation of ligand-gated ion channels.[116] In contrast, neuromodulators (catecholamines, neuropeptides) may diffuse beyond the synaptic cleft and act via extrasynaptically-expressed metabotropic receptors.[15,29,30,117–119] Thus, modulatory neurotransmitter activity extends beyond single synaptic partners and enables small numbers of neurons to modulate the activity of broader networks.[120] The absence of direct change in ionic flux across cell membranes, which is measurable using available tools like electrophysiology or genetically encoded voltage indicators (GEVIs), has necessitated the use of methods borrowed from analytical chemistry such as microdialysis and amperometry to study the dynamics of neuromodulation. However, the spatial limitations of fast-scan cyclic voltammetry and spatial and temporal limitations of microdialysis limited our ability to interpret how neuromodulators affect the plasticity or function of individual neurons and synapses.

To understand how neuromodulation sculpts brain activity, we sought to develop new tools that can optically report modulatory neurotransmitter concentrations in the brain extracellular space (ECS) in a manner that is compatible with pharmacology and other available tools to image neural structure and activity. To this end, we designed a synthetic optical probe that can report extracellular catecholamine dynamics with high spatial and temporal fidelity within a unique near-infrared spectral profile. Near-infrared (nIR) fluorescent, polymer-functionalized semiconducting single wall carbon nanotubes provide a versatile platform for optical probe synthesis to image a diverse set of biomolecular analytes [57,73,92]. In this work, we describe the design, characterization, and implementation of a nanoscale near-infrared non-genetically encoded fluorescent reporter that allows precise measurement of catecholamine dynamics in brain tissue. This technology makes use of a single wall carbon nanotube (SWCNT) non-covalently functionalized with single strand $(GT)_6$ oligonucleotides to form the near-infrared catecholamine nanosensor (nIRCat). nIRCats respond to dopamine with $\Delta F/F$ of up to 24-fold in the fluorescence emission window of 1000-1300 nm [51], a wavelength range that has shown utility for non-invasive through-skull imaging in mice. [63]

First, we show *in vitro* characterization of the nanosensor's specificity for the catecholamines dopamine and norepinephrine, and demonstrate its relative insensitivity to the neurotransmitters GABA, glutamate, and acetylcholine as well as the neuromodulators histamine, serotonin, tyramine and octopamine. Second, we demonstrate that nIRCats exhibit a fractional change in fluorescence that has the dynamic range and signal-to-noise ratio to report dopamine efflux in response to brief electrical or optogenetic stimulation of dopaminergic terminals. Next, we use optogenetic stimulation to demonstrate selectivity of the nIRCat nanosensor response to dopaminergic over glutamatergic terminal stimulation. In both stimulation contexts, we show that bath application of D2-type dopamine receptor antagonist sulpiride and agonist quinpirole modulates nIRCat signals in a manner consistent with predicted effects of presynaptic D2 autoreceptor manipulation. These latter experiments can resolve previously undetectable heterogeneity in D2 autoreceptor modulation of presynaptic dopamine release upon exposure to sulpiride or quinpirole.

Finally, we show that the presence of a dopamine reuptake inhibitor yields a prolonged nIRCat fluorescent signal indicating that the sensors report a change in the time course of dopamine diffusion and reuptake in striatal brain tissue. These data indicate that nIRCats provide a unique synthetic tool compatible with pharmacology to interrogate the release, diffusion, and reuptake of neuromodulators in neural tissue.

5.2 Results and Discussion

A near infrared dopamine and norepinephrine nanosensor

We report near-infrared fluorescent catecholamine nanosensors (nIRCats) that enable imaging of synaptic and extrasynaptic catecholamines and their release and re-uptake dynamics in the ECS of brain tissue. Using a previously established nanosensor generation platform, [46,60] synthetic bio-mimetic polymers were pinned onto the surface of intrinsically near-infrared fluorescent SWCNTs. The resulting non-covalent nanometer-scale conjugate produced the catecholamine-selective nIRCat (Figure 5.1a). In *in vitro* solution phase experiments (Methods in Appendix I), nIRCats exhibited a chirality-dependent maximal change in fluorescence ($\Delta F/F$) of up to 24 (Figure 5.1b, 5.1c) with a dynamic range spanning 4 orders of magnitude, reporting detectable fluorescence changes from 10 nM to 100 μM dopamine concentration (Figure 5.S1a). nIRCats were also sensitive to norepinephrine with a maximal response of $\Delta F/F$=35 and a similar dynamic range. We further found that nIRCats had a ~3-fold higher affinity for dopamine over norepinephrine (Figure 5.S1a). nIRCats were insensitive to GABA, glutamate, and acetylcholine (Figure 5.1c) and could report fluctuations in dopamine concentration in the presence of ascorbic acid, which is present in cerebrospinal fluid (Figure 5.S1b). nIRCats were also insensitive to octopamine and tyramine, biogenic amines that act as neurotransmitters within invertebrates (Figure 5.1c, 5.S1 c and 5.S1d), and differ from dopamine by a single hydroxyl group in the case of tyramine, or the placement of a single hydroxyl group in the case of octopamine (Figure 5.S1c, 5.S1d). Single-molecule imaging revealed that nIRCat signal in response to repeated perfusions of 10 μM dopamine was reversible, an important feature for measuring neuromodulator transients (Figure 5.S2). In previous work, we performed stochastic simulations that suggest nIRCats have sufficient sensitivity to detect physiologically relevant fluctuations in dopamine concentration in brain tissue arising from the activity of a single dopaminergic terminal, which can briefly exceed concentrations of 1 μM from the release site in a distance-dependent manner. [5]

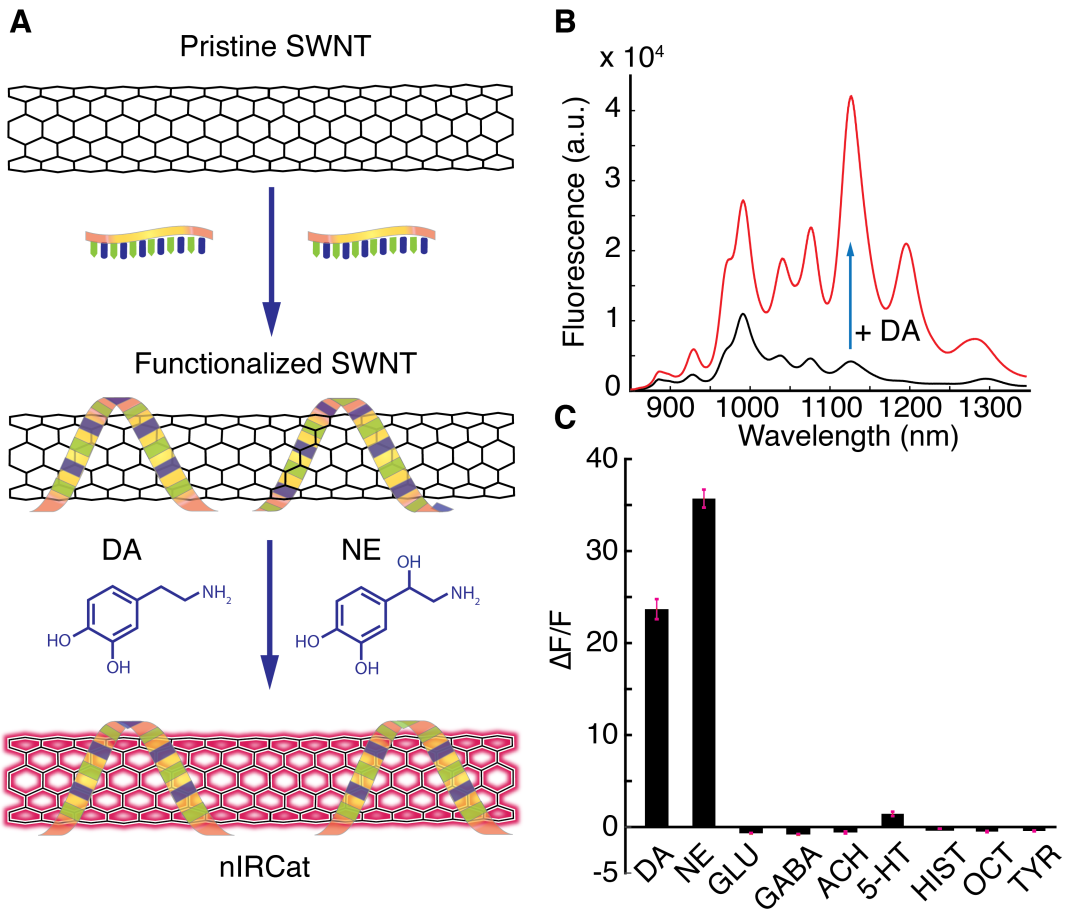

Figure 5.1 Synthesis and testing of near-infrared catecholamine nanosensors (nIRCats). (**a**) Schematic of optical catecholamine reporters, nIRCats. Pristine SWCNT are functionalized with $(GT)_6$ oligonucleotides to generate turn-on optical reporters for dopamine (DA) and norepinephrine (NE) (**b**) Fluorescence spectra of nIRCats before (black) and after (red) addition of 10 μM of dopamine in an *in vitro* preparation in phosphate buffered saline (without tissue). Multiple emission peaks correspond to unique SWCNT chiralities contained within the multi-chirality mixture. (**c**) Nanosensor optical response to 100 μM dopamine (DA), norepinephrine (NE), glutamate (GLU), γ-aminobutyric acid (GABA), acetylcholine (ACH), serotonin (5-HT), histamine (HIST), octopamine (OCT) and tyramine (TYR) (data from *in vitro* testing). Black bars represent averages from n=3 independent measurements and error bars are calculated as standard deviations of the n=3 measurements.

Imaging of electrical stimulation-evoked dopamine release in striatal brain tissue

To determine the efficacy of nIRCats for imaging dopamine in brain tissue, we used brain slices from the dorsal striatum of the mouse. Given that the dorsal striatum is densely innervated by dopaminergic projections from the substantia nigra pars compacta (SNc) but lacks innervation from neurons that release norepinephrine (NE) [121], we leveraged nIRCats capacity to serve as a dopamine sensor in the striatum. The majority of neurons within the striatum are GABAergic medium spiny neurons (MSNs) with a minority fraction of interneuron populations that include GABAergic and cholinergic interneurons.[8] Glutamatergic inputs from the cortex and thalamus are the major drivers of MSN activity and dopaminergic terminals in close proximity to these inputs are thought to play an important role in modulating the activity of MSNs and plasticity at striatal synapses.[122] Due to the

composition of local axons, intrastriatal electrical stimulation is predicted to drive the release of a mix of neurotransmitter including GABA, glutamate, acetylcholine, and dopamine, but negligible amounts of other catecholamines like norepinephrine.

Coronal mouse brain slices were prepared as described previously.[123] Slices were subsequently incubated with artificial cerebrospinal fluid (ACSF) containing 2 mg/L nIRCats for 15 minutes to enable sensors to diffuse into the brain tissue (Figure 5.S3a). Slices were subsequently rinsed to remove excess nIRCats and incubated in standard ACSF for another 15 minutes before imaging. Imaging of nIRCat fluorescence modulation in dorsal striatum was accomplished with a custom-built visible and near-infrared microscope to enable serial imaging of both visible (400 nm – 750 nm) and near-infrared (750 nm – 1700 nm) wavelengths on the same detector (Figure 5.S3b). The loading protocol enabled even and widespread labeling of the coronal slices containing the dorsal striatum (Figure 5.S3c). Using this method, Godin *et al.* [47] have found SWCNTS localize in extracellular space. For the imaging procedure, a 785 nm laser for excitation of nIRCats or mercury bulb for generating brightfield images were directed onto the back focal plane of an epifluorescence upright microscope, and imaging channels were selected using a sliding mirror. Serially, either brightfield or near-infrared images were collected on a Ninox Vis-SWIR 640 broadband camera (Raptor Photonics) with appropriate dichroic filters (Methods in Appendix I) and a 60X water dipping objective (Nikon) providing an imaging field of 178 μm by 142 μm, likely containing hundreds of dopaminergic terminals.

To investigate striatal neuromodulator release with temporal control of tissue stimulation, we used a bipolar stimulating electrode to evoke terminal release within the dorsomedial striatum of the mouse (stimulus protocol: 3 millisecond wide single square pulses over 5 biological replicates). We found a single pulse could elicit a nIRCat signal transient (Figure 5.2a), and that increasing the strength of the stimulus led to larger evoked changes in nIRCat $\Delta F/F$ signal, $(\Delta F/F)_{max}$ 0.1 mA = 0.047 ± 0.025; 0.3 mA = 0.122 ± 0.026; and 0.5 mA = 0.2 ± 0.033; mean ± s. d., n=5 for all measurements, p=0.008 between 0.1 mA vs. 0.3 mA, p=0.008 between 0.3 mA vs. 0.5 mA) (Figure 5.2b). Similar responses were additionally obtained in an *ex vivo* slice of a previously wild-caught species of mouse (*Mus spicilegus*) (Figure 5.S4a, 5.S4b). We included this species in order to illustrate the potential of this tool for use in species not typically found in laboratories, and in which surgical or genetic manipulation may be a barrier to measurement.

To further test if evoked nIRCat signals in the mouse tracked striatal dopamine release and reuptake kinetics, we investigated the effect of nomifensine, a dopamine reuptake inhibitor that slows the clearance of dopamine from the ECS by competitively binding to dopamine transporters (DATs). Addition of 10 μM nomifensine to the bath yielded nIRCat signal with higher peak fluorescence modulation ($(\Delta F/F)_{max}$ = 0.108 ± 0.029 vs. 0.189 ± 0.023; mean ± s. d., n=3, p=0.0178) and a prolonged fluorescent signal compared to signals obtained in ACSF from the same field of view (decay time constant, τ=2.43 ± 0.24 s vs. 10.95 ± 1.15 s; mean ± s. d., n=3, p=0.0002) (Figure 5.2a top vs. bottom row, Figure 5.2c). Application of 0 mM extracellular Ca^{2+} ACSF abolished detectable nIRCat responses (P < 0.0001 relative to 2.5 mM Ca^{2+} ACSF), whereas 4 mM Ca^{2+} significantly enhanced evoked ΔF/F transients (p < 0.0001) (Figure 5.2d), confirming that nIRCat signals reflect a calcium dependent process.

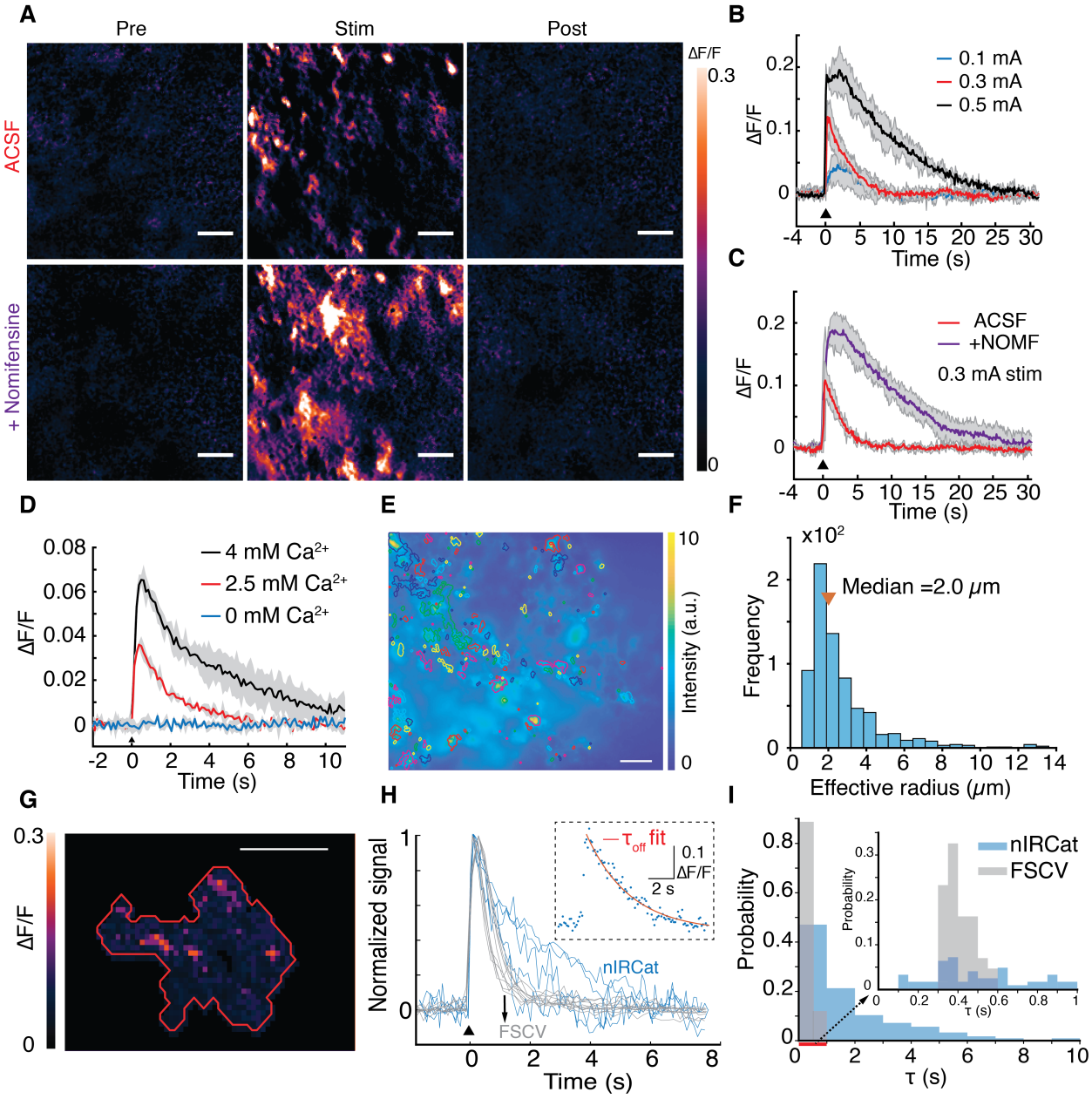

Figure 5.2 Imaging and spatiotemporal analysis of dopamine release evoked by electrical stimulation in striatal tissue. (**a**) Repeat images of the same field of view and *ΔF/F* of nIRCat signal after electrical stimulation of 0.3 mA in standard ACSF (top row) and in ACSF plus 10 μM nomifensine (bottom row, +Nomifensine). Three example still frames are presented: "Pre" is before electrical stimulation is applied, "Stim" represents frame corresponding to peak *ΔF/F* following stimulation, and "Post" is a frame after nIRCat fluorescence has returned to baseline. Scale bars = 10 μm. (**b**) Nanosensor fluorescence modulation scaled with single pulse electrical stimulation amplitudes. Field of view mean traces and standard deviation bands are presented for three stimulation amplitudes of 0.1 mA, 0.3 mA, and 0.5 mA (**c**) Time traces of *ΔF/F* for 0.3 mA single pulse stimulation in standard ACSF (red) and in ACSF plus 10 μM nomifensine (purple, +NOMF). Mean traces with standard deviation bands are presented. (**d**) nIRCat ΔF/F responses are abolished in 0 mM Ca^{2+} ACSF and vary with extracellular [Ca^{2+}]. (**e**) A single frame from a time series gathered in the dorsomedial striatum showing the entire field of view, overlaid with ROIs identified using per-pixel *ΔF/F* stack projections of nIRCat fluorescence modulation (Methods in Appendix I). Color bar represents nIRCat labeling fluorescence

intensity. Scale bar = 20 μm. (**f**) Frequency histogram of ROI sizes depicted in (**e**), exhibiting a log-normal distribution with median ROI size of 2 μm. (**g**) A higher magnification view of an ROI with an effective radius of 5 μm. Maximum *ΔF/F* projection of the ROI shows presence of smaller fluorescence hotspots within the ROI. Scale bar = 5 μm. (**h**) Overlay of representative normalized FSCV (gray) and nIRCat (blue) traces showing that nIRCat ROI signals exhibit heterogeneity in decay kinetics. Inset: An example of nIRCat experimental data (blue dots) fitted to first order decay kinetics (red line) to compute decay time constants (τ). (**i**) Normalized frequency histogram of τ's computed from FSCV and nIRCat individual ROI time traces. Data from n= 4 fields of view representing n=2 biological replicates were pooled. Medians of each distribution: nIRCats τ = 1.1 s and FSCV τ = 0.4 s.

To identify nIRCat fluorescence change hotspots (i.e., regions of high *ΔF/F*), we analyzed our video-rate acquisitions using a custom-built program that accounted for background fluorescence and identified regions with fluctuations in fluorescence intensity in the post-stimulation epoch (Methods in Appendix I). We defined nIRCat *ΔF/F* hotspots as regions of interest (ROIs) based on a per-pixel stack projection of maximal *ΔF/F* in the imaging time series. Using data from single pulse electrical stimulation experiments, we used custom software that identified ROIs whose sizes varied from 1 μm to 15 μm, with a log-normal distribution and a median ROI size of 2 μm (Figure 5.2e, 5.2f). Repeat stimulations with the same stimulation amplitude in fields of view of the dorsomedial striatum across biological replicates generated similar size distributions (Figure 5.S5 a). We found that *ΔF/F* hotspots do not necessarily correspond to high nIRCat labeling of the brain tissue, suggesting that the hotspots are a consequence of variation in dopamine release and not nanosensor loading in the tissue (Figure 5.S5 b - f). Closer examination of several larger ROIs (> 5μm) suggested these may be comprised of smaller hot-spots in close proximity (Figure 5.2g and Figure 5.S5b, 5.S5c).

For further examination of the temporal resolution of nIRCats, we compared the temporal profile of evoked transients measured with nIRCats to transients measured with fast scan cyclic voltammetry (FSCV). FSCV is a technique that has been widely used to measure temporal catecholamine dynamics both *in vivo* and *in vitro* in the striatum and other brain areas [124–126]. FSCV and nIRCat experiments were conducted on separate experimental rigs with the same solutions, temperature settings, electrodes, and stimulation parameters. Evoked transients measured with FSCV (Figure 5.S5g) and nIRCat fluorescence emission showed comparable temporal profiles in the rising phase (latency to peak: FSCV = 0.25 ± 0.0 s vs. nIRCat = 0.40 ± 0.18 s; mean ± s. d., n=4 fields of view from 2 biological replicates, p=0.23). Meanwhile, nIRCat signals exhibited a wider diversity of decay kinetics (τ: FSCV = 0.51 ± 0.08 s vs. nIRCats = 2.43 ± 0.24 s; mean ± s. d. n=4 fields of view from 2 biological replicates, p=0.0002). A subset of ROIs exhibited decay time constants that overlapped with, or were faster than, those of FSCV signals (Figure 5.2h, 5.2i).

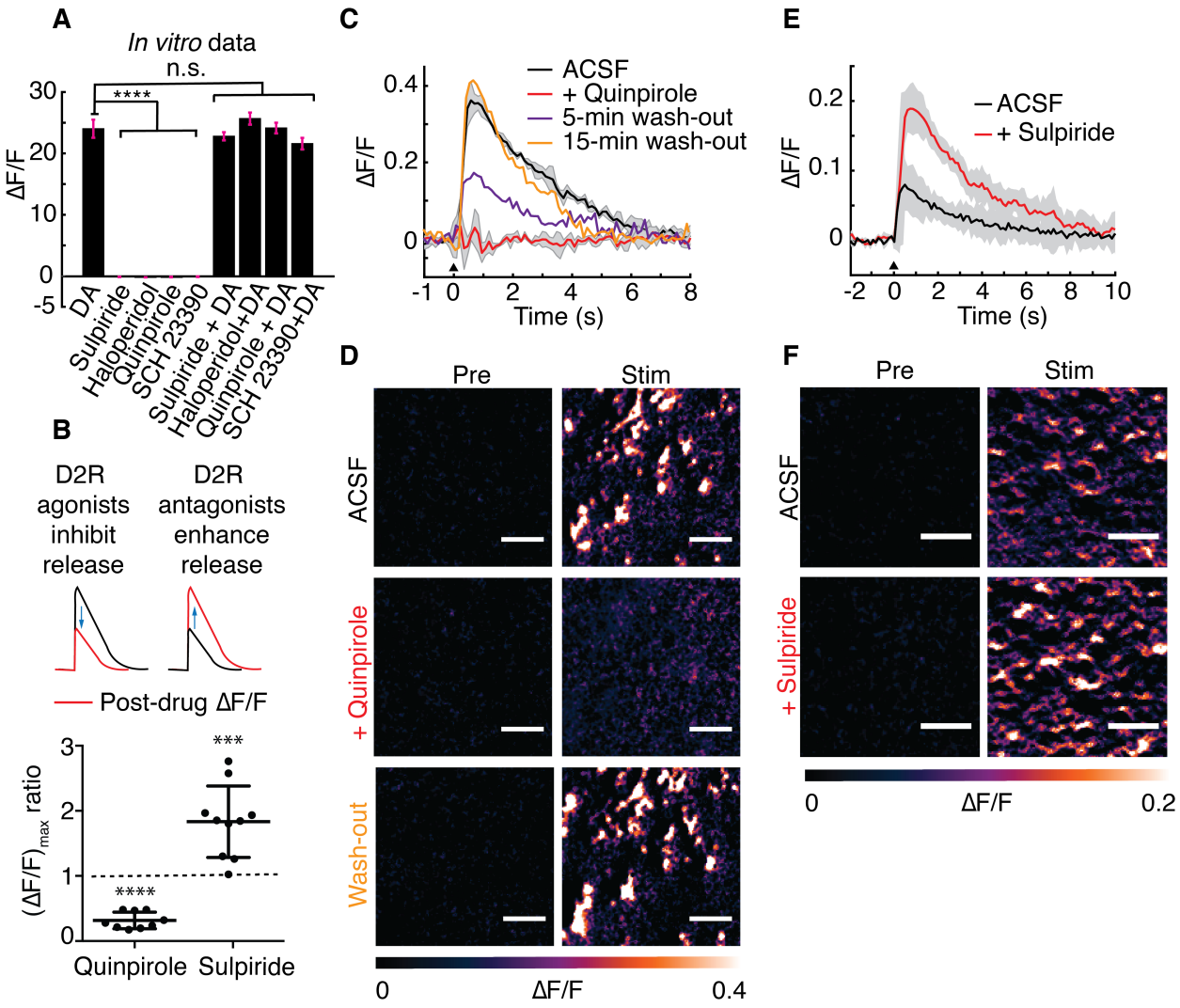

Figure 5.3 Imaging dopamine release in the presence of dopamine receptor agonists and antagonists. (**a**) *In vitro* solution phase maximal *ΔF/*F (amplitude change at ~1128 nm) of nIRCat in presence of 100 μM dopamine (DA), the dopamine receptor drugs sulpiride, haloperidol (DRD2 antagonists), quinpirole (DRD2 agonist), and SCH 23390 (DRD1 antagonist), and dopamine receptor drugs + DA. Addition of 1 μM drug quantities did not induce nIRCat fluorescence modulation in the absence of DA ($p < 0.0001$ compared to DA *ΔF/F*). Subsequent addition of DA to drug-incubated nIRCat solutions produced *ΔF/F* responses indistinguishable from DA-only responses. Error bars represent standard deviations from n=3 measurements (**b**) Top: a schematic of the effect of D2R agonist and antagonist drugs on dopamine release. Quinpirole suppressed nIRCat fluorescence modulation ($p<0.0001$), whereas sulpiride facilitated nIRCat fluorescence ($p=0.001$) in n=3 biological replicates. Individual data points represent $(\Delta F/F)_{max}$ ratio of the average trace collected in same field of view (post-drug application/pre-drug application). (**c, d**) In brain slice, quinpirole (1 μM) suppressed nIRCat fluorescence modulation in response to a single electrical pulse (0.5 mA, 3 ms) (red trace) compared to pre-drug ACSF (black trace) but recovered following drug wash-out (purple and orange traces). (**e, f**) Sulpiride (1 μM) enhanced nIRCat fluorescence modulation in response to single electrical pulse stimulation, yielding brighter nIRCat ΔF/F hotspots compared to drug-free ACSF. Scale bars = 10 μm. All error bands (**c, e**) represent standard deviation from the mean trace.

We next evaluated the ability of nIRCats to detect dopamine in the presence of dopamine receptor drugs. First using *in vitro* solution phase experiments (without biological

tissue), we found that nIRCat fluorescence intensity was not modulated by exposure to 1 µM concentration of D2R antagonists sulpiride, haloperidol, the D2R agonist quinpirole, or the D1R antagonist SCH-23390 (Figure 5.3a). Furthermore, with these *in vitro* solution phase experiments, we showed that dopamine-induced nIRCat fluorescence signals were not altered in the presence of these same dopamine receptor drugs. These data confirmed that nIRCats retained their functionality in the presence of drugs that serve as dopamine agonists and antagonists (Figure 5.3a).

We next moved to brain slice where presynaptic dopamine autoreceptors are known to play a critical role in regulating dopamine release. In the dorsal striatum of acute slices from n=3 biological replicates, we found that a dopamine D2R agonist suppressed nIRCat transients while a D2R antagonist enhanced them (Figure 5.3b). Application of quinpirole (1 µM) suppressed nIRCat fluorescent transients in response to single electrical pulse stimulation which recovered following 15-minute drug wash-out (Figure 5.3c, 5.3d). Conversely, application of sulpiride (1 µM) significantly increased nIRCat *ΔF/F* (Figure 5.3e, 5.3f). Importantly, the effects of these agonists and antagonists were present in *ex vivo* brain tissue while they were absent in *in vitro* solution phase experiments above. Our results are therefore consistent with powerful inhibition of presynaptic dopamine release by the D2R agonist quinpirole and facilitation of presynaptic dopamine release by the D2R antagonist sulpiride.

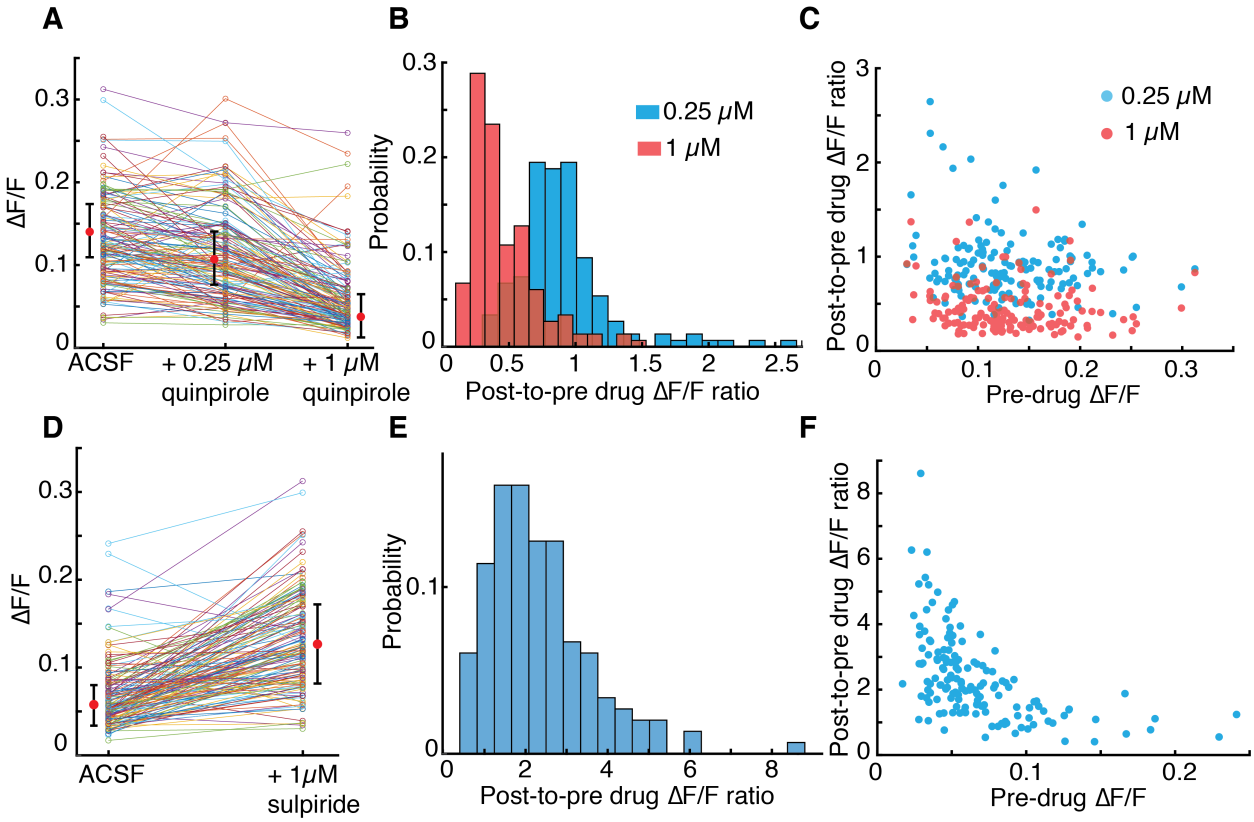

Figure 5.4 Effects of quinpirole and sulpiride on nIRCat response at the level of ROIs (4 microns or smaller). (**a**) *ΔF/F* of ROIs in ACSF and in ACSF with 0.25 µM and 1 µM of quinpirole. Each *ΔF/F* data point corresponding to an ROI is an average from n=3 stimulation repeats. (**b**) Distribution of nIRCat response attenuation upon addition of 0.25 µM (blue) or 1µM (red) quinpirole for ROIs in (a). (**c**) Scatter plot of response

to drug vs. pre-drug *ΔF/F* amplitude for data in (a). (**d**) ΔF/F of ROIs in ACSF and following addition of 1 μM of sulpiride. Each *ΔF/F* data point corresponding to an ROI is an average from n=3 stimulation repeats. (**e**) Distribution of post-to-pre drug *ΔF/F* ratio for data in (d). (**f**) Scatter plot of response to drug vs. pre-drug *ΔF/F* amplitude for data in (**d**). For (**a**) and (**d**), means and error bars (standard deviation) are presented next to each distribution.

Optical recording capability and nanoscale size of nIRCats enables investigation of dopamine dynamics and pharmacological manipulation with higher spatial resolution than can be achieved using other tools. Therefore, we next examined the effects of quinpirole and sulpiride on individual ROIs (Methods in Appendix I). We also used an intermediate dose to provide greater information about differential dose response. We again used electrical stimulation in the dorsal striatum to drive dopamine release and compared the effect of quinpirole before and after bath application of the drug. We focused on ROIs 4 microns or smaller to capture the majority of ROIs while excluding the long tail of larger ROIs that are likely to contain many dopaminergic synapses (Figure 5.2 f, 5.2g). Averaging all active ROIs 4 microns or smaller, a high (1 μM) concentration of quinpirole yielded post-drug to pre-drug *ΔF/F* amplitude ratio of 0.48 ± 0.35 (Figure 5.4a, 5.4b). A lower concentration of quinpirole (0.25 μM) resulted in an amplitude ratio of 0.91 ± 0.36 (mean ± s. d. of n=150 ROIs identified within the field of view) (Figure 5.4a, 5.4b). We repeated the experiment and analysis with bath application of sulpiride (1 μM) and observed a sulpiride-induced amplitude ratio of 2.34 ± 1.3 (mean ± s. d. of n=150 ROIs within field of view) (Figure 5.4d, 5.4e).

Analyses of individual ROIs (all smaller that 4 μm) revealed heterogeneity in ROI responses upon bath application of either quinpirole or sulpiride. Notably, application of quinpirole preferentially suppressed ROIs that exhibited higher *ΔF/F* before application of the drug (Pearson correlation of r = -0.21, p = 0.01 for 0.25 μM data and r = -0.17, p = 0.03 for 1 μM data in Figure 5.4c). Additional quinpirole wash-on results are presented in Figure 5.S6 a-c and Figure 5.S9. Conversely, our analysis showed that application of sulpiride enhanced nIRCat response in ROIs that had lower *ΔF/F* before application of the drug (Figure 5.4f, Pearson correlation of r = -0.53, p < 0.0001) (see additional data in Figure 5.S6 d-f). Our work uncovers a statistically significant correlation between an ROI's pre-drug *ΔF/F* amplitude and its post-drug response. It is possible that the observed heterogeneity in ROI responses maps onto variation in D2 autoreceptor expression and/or function (37, 39), but further characterization will be necessary to confirm this hypothesis.

Imaging of optogenetically-evoked dopamine release in striatal tissue

To further confirm striatal nIRCat nanosenor signals were indeed reporting dopamine release, we compared channelrhodopsin (ChR2) stimulation of cortical glutamatergic and nigrostriatal dopaminergic terminals in the dorsal striatum. Acute striatal brain slices were prepared from mice virally transfected to express the light sensitive cation channel ChR2 in either glutamatergic terminals of the striatum (targeted by viral injection in the frontal cortices, ChR2-GLU) (Figure 5.5a, Figure 5.S7a, 5.S7b) or dopaminergic terminals (targeted by viral injection in the midbrain in DAT-cre mice; ChR2-DA) (Figure 5.5c, Figure 5.S7 c). Upon optical stimulation of ChR2-DA terminals with a 473 nm laser (5 pulses at 25 Hz, 1 mW/mm^2) in the dorsal striatum, we observed significant fluorescence modulation of

nIRCat signal (Figure 5.5d). In contrast, when optogenetic stimulation was targeted at cortical glutamatergic terminals in the striatum, fluorescent nIRCat signals did not rise above baseline fluctuation. Notably, we could confirm in control experiment that optogenetic stimulation of cortical glutamatergic terminals was able to evoke excitatory postsynaptic currents (EPSCs) in striatal MSNs (Figure 5.5b inset, Figure 5.S7d, 5.S7e).

Returning to ChR2-DA stimulation, we next varied the number of stimulation pulses (5 ms pulse duration, 25 Hz, 1 mW/mm^2) and observed scaling in nIRCat $\Delta F/F$ amplitude from 1 pulse to 10 pulses (p=0.005), and trend level differences between 1 pulse and 5 pulses (p=0.0645) and 5 pulses and 10 pulses (p=0.086) (Figure 5.5e). When we varied the pulse frequency while holding the number of pulses constant at 5, we observed scaling with significant differences detectable between 1 Hz and 10 Hz (p=0.036). The amplitude difference between 10 Hz and 25 Hz did not reach significance (p=0.179) (Figure 5.5f). In single pulse experiments in which we varied pulse width, nIRCat fluorescence responses scaled with pulse duration. This effect was significant when comparing 2 ms to 5 ms (p=0.002) but the difference from 5 ms to 10 ms did not reach significance (p=0.055) (Figure 5.5g).

Finally, we tested the effect of dopaminergic pharmacological agents on optogenetically evoked dopamine release (ChR2-DA). Bath application of quinpirole (1 μM) powerfully suppressed nIRCat fluorescence ($p < 0.0001$), and this effect was reversed after drug washout (Figure 5.5h). Consistent with results from electrical stimulations, optogenetic stimulations also showed that quinpirole suppressed the most active ROIs preferentially (Figure 5.S8). Nomifensine (10 μM) enhanced nIRCat signal decay time, consistent with the predicted slowing of dopamine clearance from the ECS (Figure 5.S9).

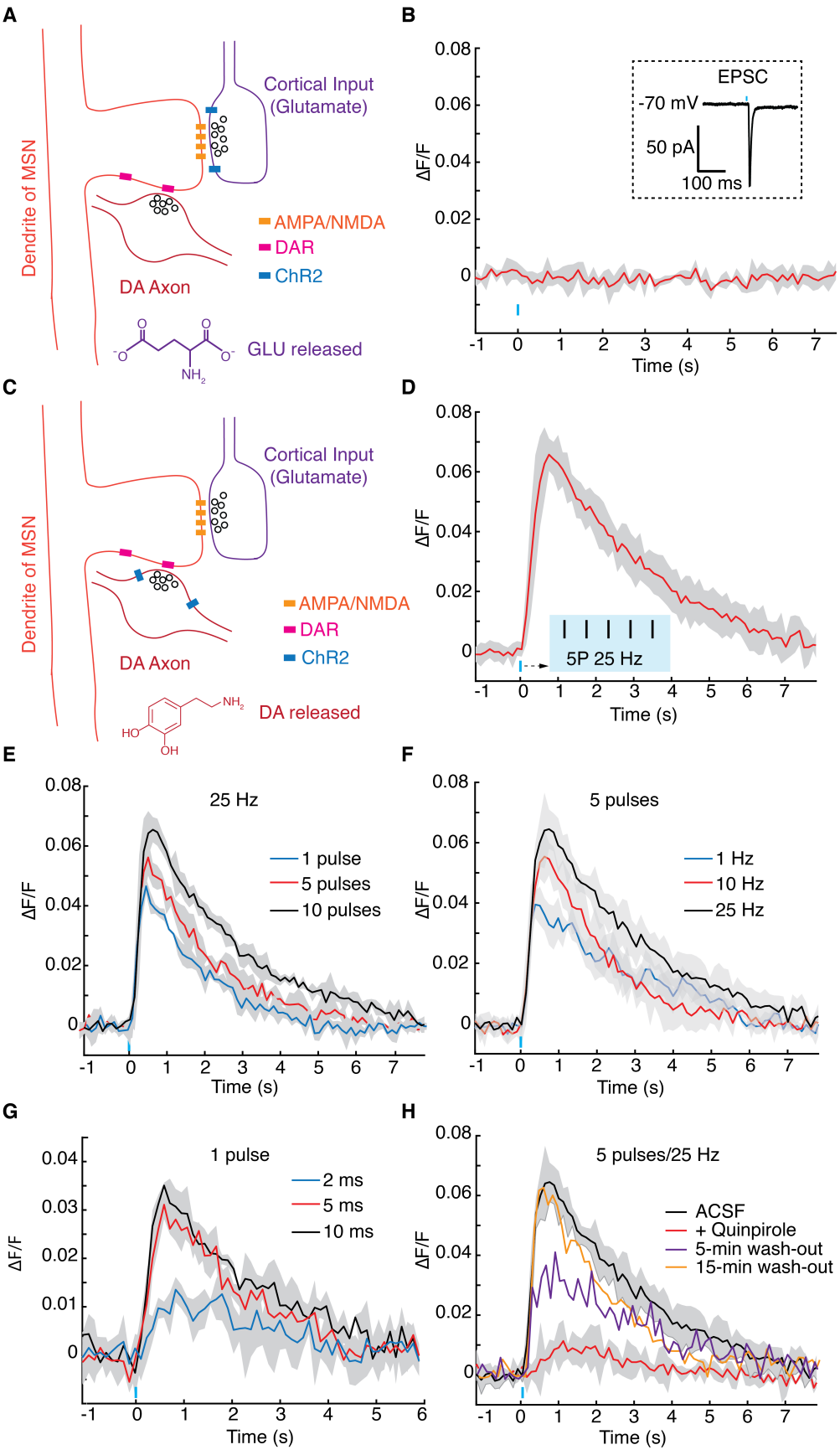
A
Dendrite of MSN
Cortical Input
(Glutamate)
AMPA/NMDA
DAR
ChR2
DA Axon
GLU released
B
EPSC
-70 mV
50 pA
100 ms
ΔF/F
Time (s)
C
Dendrite of MSN
Cortical Input
(Glutamate)
AMPA/NMDA
DAR
ChR2
DA Axon
DA released
D
5P 25 Hz
ΔF/F
Time (s)
E
25 Hz
1 pulse
5 pulses
10 pulses
ΔF/F
Time (s)
F
5 pulses
1 Hz
10 Hz
25 Hz
ΔF/F
Time (s)
G
1 pulse
2 ms
5 ms
10 ms
ΔF/F
Time (s)
H
5 pulses/25 Hz
ACSF
+ Quinpirole
5-min wash-out
15-min wash-out
ΔF/F
Time (s)

Figure 5.5 nIRCat detection of striatal dopamine release evoked by optogenetic stimulation (**a**) Schematic of ChR2 expression in cortical glutamatergic terminals synapsing in the dorsal striatum. (**b**) No nIRCat fluorescence modulation was observed after stimulation of glutamatergic terminals. Inset: glutamate release was confirmed by excitatory postsynaptic current on medium spiny neuron. (**c**) Schematic of ChR2 expression in nigrostriatal dopaminergic terminals of the dorsal striatum. (**d**) Stimulation of dopaminergic terminals resulted in nIRCat fluorescence modulation. Stimulation protocol in (b) and (d) was 5 pulses at 25 Hz and power flux of 1 mW/mm^2 and each pulse had a duration of 5ms. (**e**) nIRCat *ΔF/F* in response to increasing number of pulses delivered at 25 Hz, 5 ms pulse duration. (**f**) nIRCat *ΔF/F* in response to increasing pulse frequency (1, 10, 25 Hz) of 5 pulses. Each pulse had a duration of 5 ms. (**g**) nIRCat *ΔF/F* in response to single pulses of 2 ms, 5 ms and 10 ms duration. (**h**) Bath application of 1 μM of quinpirole suppresses dopamine release and results in depressed nIRCat *ΔF/F*. Drug wash-out rescues dopamine release and nIRCat *ΔF/F*. All error bands represent standard deviation from the mean trace.

5.3 Conclusion

To understand how neuromodulation alters the plasticity and activity of distinct populations of neurons, there is need for new optical tools that can measure the extracellular dynamics of neuromodulator release and reuptake at spatiotemporal resolution commensurate with methods used to record neural activity (e.g. electrophysiology and calcium imaging). Here, we demonstrated the feasibility of using of a non-genetically encoded fluorescent sensor, nIRCat, to enable optical detection of catecholamine release and reuptake with sub-second temporal and with micrometer spatial resolution. We used electrical and optogenetic methods in striatal brain tissue to demonstrate that nIRCat fluorescent signals faithfully report evoked dopamine release and pharmacologically induced changes in dopamine dynamics.

We focused nIRCat imaging experiments within the dorsal striatum, a region that receives dense dopaminergic innervation and negligible norepinephrine innervation. [121] Therefore, while nIRCats are not selective for dopamine over norepinephrine, nIRCats effectively function as a dopamine sensor within the context of the striatum. Given that striatal dopamine regulates fundamental processes including motor function, motivation and learning, nIRCats represent an important addition to the neuroscience investigative toolkit. Furthermore, of the biogenic amines present in invertebrate species (dopamine, tyramine, octopamine, serotonin, histamine), we demonstrated *in vitro* that nIRCats are exclusively sensitive to dopamine. Hence for invertebrate species such as drosophila, we predict that nIRCats may serve as selective and highly sensitive dopamine sensors throughout the brain.

While other tools are emerging to optically report dopamine fluctuations via cell-surface engineered proteins,[3,4] nIRCats are likely to fulfill a niche amongst currently available methods for detecting dopamine neurotransmission due to their unique near-infrared fluorescence, the fact that they do not rely on genetic delivery and expression, their relative ease of deployment, and their functionality in the presence of pharmacological dopamine receptor ligands. This is in contrast to receptor-based fluorescent sensors which currently cannot report on endogenous dopamine dynamics in the presence of ligands to the engineered receptor but do exhibit selectivity for dopamine over norepinephrine.[3,4] Furthermore, the synthetic nature of nIRCats eliminates concern about potential GPCR-mediated residual signaling that may be present in protein-based optical probes. nIRCats also offer spatial advantages over FSCV, and our initial experiments suggest that the

temporal resolution of the nIRCat signal can be comparable to that of FSCV. nIRCat fluorescence decay profiles exhibit a wider temporal range than that observed from FSCV data and included a significant number of ROIs that showed seconds-long time constants in addition to time constants faster than those measured by FSCV. It is debatable if these results capture the unique spatial properties of specific striatal ROIs or are related to tool differences alone. nIRCats, unlike FSCV probes, should sample catecholamine concentration at a single point in space, such that each distributed nIRCat construct can act as a probe within the ECS and therefore yield a "higher resolution" picture of neuromodulator dynamics. Future experiments will investigate how the heterogeneity of nIRCat signals (amplitude, kinetics, and modulation by drugs) relates to structural and functional properties at dopamine terminals and within the ECS. We predict that new optical tools for measuring dopamine dynamics with high spatial resolution will be enable new insights into the regulation of dopamine release and reuptake at the level of individual synapses.[20,127,128]

Furthermore, we see potential for future expansion of a larger family of SWCNT based near-infrared nanosensors (nIRNS) similar to nIRCats for multiple neurochemical imaging applications. Several lines of evidence illustrate their future potential. First, nIRNS are easily functionalized with a wide range of synthetic molecular recognition moieties, affording fine control of their surface functional elements and their interactions with the local chemical environment [57,67,79]. SWCNT fluorescence can be finely tuned to monochromatic emission in the near-infrared II (1000-1700 nm) window by controlling the SWCNT chirality.[129] This chirality-dependent fluorescence in the near-infrared II window provides further avenues for designing color-specific responses to multiple molecular analytes simultaneously, thereby affording synthesis of ratiometric and multiplexed analyte imaging platforms, as we have shown previously.[71] Second, SWCNT-based nanosensors rely on near-infrared fluorescence, which greatly reduces the impact of tissue scattering in the emission window and therefore may enable through-cranium imaging.[63] nIRNS are compatible with multi-photon imaging with 1600 nm excitation[62] and as such could permit nanoscale imaging of intact neuronal structures pending parallel developments in all-infrared microscopy, as has been shown with visible wavelength-emitting fluorophores.[130] Third, nIRNS exhibit robust non-photobleaching photostability, allowing their use in long-term imaging experiments.[131] Fourth, because nIRNS are not genetically-encoded, they could enable use in species where gene delivery and protein expression is intractable, time consuming, or undesirable. Finally, the nanosecond-scale binding kinetics and nanoscale dimensions of nIRNS are likely to enable generation of other neuromodulator nanosensors with improved temporal and spatial resolution. In sum, nIRCats are versatile catecholamine probes amenable to multiplexing with existing tools for concurrent investigation of dopaminergic neuromodulation with other core mechanisms of brain function.

5.4 Appendix I

Materials and Methods

Nanosensor synthesis

$(GT)_6$ oligonucleotides were purchased from Integrated DNA Technologies (IDT, Standard Desalting). HiPCo SWCNT were purchased from NanoIntegris (Batch # HR27-104). $(GT)_6$-SWCNT colloidal suspension (nIRCat) was prepared by mixing 1 mg of $(GT)_6$ and 1 mg of SWCNT in 1 mL of a 100 mM NaCl solution. The solution was bath sonicated (Branson Ultrasonic 1800) for 10 minutes and probe-tip sonicated for 10 minutes at 5 W power (Cole Parmer Ultrasonic Processor, 3 mm tip diameter) in an ice-bath. The sonicated solution was incubated at room temperature for 30 minutes. The product was subsequently centrifuged at 16,000 g (Eppendorf 5418) for 90 minutes to remove unsuspended SWCNT bundles and amorphous carbon, and the supernatant was recovered for characterization and use. Each nanosensor suspension was stored at 4°C until use.

Nanosensor characterization

To characterize nIRCats post-synthesis, the full visible and near-infrared absorption spectrum was taken for each nanosensor batch (UV-VIS-NIR spectrophotometer, Shimadzu UV-3600 Plus) or UV-VIS (ThermoFisher Scientific Genesys 20). SWCNT concentrations of as-made nanosensor batches were determined using absorbance at 632 nm (UV-VIS) with an extinction coefficient of $\varepsilon = 0.036\ (mg/L)^{-1}\ cm^{-1}$. Full spectrum absorbance measurements were made with UV-VIS-NIR after dilution to 5 mg/L SWCNT concentration in 100 mM NaCl. For fluorescence spectroscopy, each sensor batch was diluted to a working concentration of 5 mg/L in 100 mM NaCl, and aliquots of 198 µL were placed in each well of a 96-well plate (Corning). Fluorescence measurements were obtained with a 20 X objective on an inverted Zeiss microscope (Axio Observer.D1) coupled to a Princeton Instruments spectrograph (SCT 320) and liquid nitrogen cooled Princeton Instruments InGaAs linear array detector (PyLoN-IR). A 721nm laser (OptoEngine LLC) was used as the excitation light source for all characterization experiments.

Neurotransmitter analyte library and dopamine receptor drug screening

For neurotransmitter response screens, we collected the near-infrared fluorescence spectrum from 198 µL aliquots of nanosensor (5 mg/L SWCNT concentration) before and after addition of 2 µL of 10 mM solutions of each analyte neurotransmitter (for a 100 µM final analyte concentration in each well of a 96-well plate). All neurotransmitter analytes were purchased from Sigma-Aldrich. Neurotransmitter analytes were incubated for 5 minutes before taking post-analyte fluorescence measurements. Responses were calculated for the integrated fluorescence count as $\Delta F/F_0 = (F-F_0)/F_0$, where F_0 is total fluorescence before analyte addition and F is total fluorescence after analyte addition or for peak fluorescence change corresponding to the (9,4) SWCNT chirality (~1128 nm center wavelength). All measurements were made in triplicate. Reported results are mean and standard deviations of the triplicate measurements. All nIRCat nanosensor batches were tested for catecholamine responses prior to use for tissue catecholamine imaging. Dopamine receptor drugs were purchased from Tocris (quinpirole and sulpiride), abcam (SCH 23390) and Sigma-Aldrich (haloperidol). nIRCat fluorescence modulation to dopamine receptor drugs were measured after addition of 1 µM drug quantities (final concentration in well) in each well. Post-drug fluorescence spectra were taken after 5-minute drug incubation. To measure nIRCat response to dopamine in the presence of drugs, dopamine aliquots were

added to each drug-incubated well to obtain 100 μM dopamine, and post-dopamine fluorescence spectra were taken after an additional 5-minute incubation period.

Nanosensor reversibility testing

A #1.5 glass coverslip was functionalized with (3-Aminopropyl) triethoxysilane (APTES, Sigma Aldrich) by soaking in 10% APTES in ethanol for 5 min. The coverslip was then rinsed with DI water and left to dry. The coverslip was then fixed onto an ibidi sticky-Slide VI 0.4 forming 6 microfluidic channels. First, 100 μL of PBS was pipetted through a channel. Next, the channel was filled 50 μL of a 5 mg/L solution of nIRCats and left to incubate at room temperature for 5 min. The channel was rinsed using three 50 μL PBS washes, keeping the channel filled with solution at all times. The surface immobilized nIRCats in PBS were imaged on an epifluorescence microscope with 721 nm excitation and a Ninox VIS-SWIR 640 camera (Raptor). One end of the flow channel was connected to a syringe pump (Harvard Appartus) using Luer lock fittings. Prior to the start of image acquisition, the opposite flow reservoir was filled with PBS and the pump was set to refill mode at a volumetric flow rate of 40 μL min^{-1}. Once the liquid in the reservoir was depleted, 40 μL of 10 μM dopamine in PBS was added. The process was repeated using alternating additions of 80 μL of PBS washes and 40 μL of dopamine solution.

Acute slice preparation and nanosensor labeling

Mice were C57 Bl/6 strain, 60 days old, and both male and female mice were used. Mice were group housed after weaning at P21 and kept with nesting material on a 12:12 light cycle. All animal procedures were approved by the UC Berkeley Animal Care and Use Committee (ACUC). Acute brain slices were prepared using established protocols.123 Briefly, mice were deeply anesthetized via intraperitoneal injection of ketamine/xylazine cocktail and transcardial perfusion was performed using ice-cold cutting buffer (119 mM NaCl, 26.2 mM NaHCO3, 2.5 mM KCl, 1mM NaH2PO4, 3.5 mM MgCl2, 10 mM Glucose, 0 mM CaCl2), after which the brain was rapidly extracted. The cerebellum and other connective tissues were trimmed using a razor blade and the brain was mounted onto the cutting stage of a vibratome (Leica VT 1200S). Coronal slices (300 μm in thickness) including the dorsal striatum were prepared. Slices were incubated at 37°C for 60 minutes in oxygen saturated ACSF (119 mM NaCl, 26.2 mM NaHCO3, 2.5 mM KCl, 1mM NaH2PO4, 1.3 mM MgCl2, 10 mM Glucose, 2 mM CaCl2) before use. Slices were then transferred to room temperature for 30 minutes before starting imaging experiments and were maintained at room temperature for the remainder of experimentation.

For nanosensor labeling, slices were transferred into a small volume brain slice incubation chamber (Scientific Systems Design, Inc., AutoMate Scientific) and kept under oxygen saturated ACSF (total 5 mL volume). 100 μL of 100 mg/L nIRCat nanosensor was added to the 5mL volume and the slice was incubated in this solution for 15 minutes. The slice was subsequently recovered and rinsed in oxygen saturated ACSF to wash off nIRCats that did not localize into the brain tissue. The rinsing step was performed by transferring the slice through 3 wells of a 24 well plate (5 seconds in each well) followed by transfer to the recording chamber with ACSF perfusion for a 15-minute equilibration period before starting the imaging experimentation. All imaging experiments were performed at 32°C.

Acute slice preparation for FSCV recording

Acute slices were prepared as described previously. Extracellular dopamine concentration evoked by local electrical stimulation was monitored with FSCV at carbon-fiber microelectrodes (CFMs) using Millar voltammeter. CFMs were ~ 7 μm in diameter encased in glass capillary pulled to form a seal with the fiber and cut to final tip length of 70-120 μm. The CFM was positioned ~100 μm below the tissue surface at a 45-degree angle. A triangular waveform was applied to the CFM scanning from -0.7 V to +1.3 V and back, against Ag/AgCl reference electrode at a rate of 800 V/s. Evoked dopamine transients were sampled at 8 Hz, and data were acquired at 50 kHz using AxoScope 10.5 (Molecular Devices). Oxidation currents evoked by electrical stimulation were converted to dopamine concentration from post-experimental calibrations. Recorded FSCV signals were identified as dopamine by comparing oxidation (+0.6 V) and reduction (-0.2 V) potential peaks from experimental voltammograms with currents recorded during calibration with 2 μM dopamine dissolved in ACSF. For stimulation, a bipolar stimulation electrode (FHC CBAEC75) was positioned on top of the brain slice and approximately 100 μm away from the CFM. Following 30-minute slice equilibration in the recording chamber, dopamine release was evoked using a square pulse (0.3 mA pulse amplitude, 3 ms pulse duration) controlled by Isoflex stimulus isolator (A.M.P.I) and delivered out of phase with the voltammetric scans. Stimulation was repeated 3 times. To compare FSCV and nIRcat data, each signal was normalized against its peak value ([DA]max or (ΔF/F)max) and co-aligned at stimulation time. Latency to peak were computed as tpeak - tstim where tpeak is the time at which peak signal is attained and tstim is time of stimulation. Decay time constants (τ) were computed from model fits to a first order decay process.

Microscope construction and slice imaging

Ex vivo slice imaging was performed with a modified upright epifluorescent microscope (Olympus, Sutter Instruments) mounted onto a motorized stage. Nanosensor excitation was supplied by a 785 nm, CW, DPSS laser with adjustable output power to a maximum of 300 mW and a near TEM00, top hat beam profile (OptoEngine LLC). The beam was expanded using a Keplerian beam expander comprised of two plano-convex lenses (Thorlabs, *f*=25 mm, *f*=75 mm, AR coating B) to a final beam diameter of approximately 1 cm. The beam was passed through a custom fluorescence filter cube (excitation: 800 nm shortpass (FESH0800), dichroic: 900 longpass (DMLP990R), emission: 900 longpass (FELH0900), Thorlabs) to a 60X Apo objective (1.0 NA, 2.8 mm WD, water dipping, high NIR transmission, Nikon CFI Apo 60XW NIR). Emission photons collected from the sample were passed through the filter cube and were focused onto a two-dimensional InGaAs array detector (500-600 nm: 40% quantum efficiency (QE); 1000-1500 nm: >85% QE; Ninox 640, Raptor Photonics) and recorded using Micro-Manager Open Source Microscopy Software.[132] Laser power was adjusted to maximize collected photons and fill the pixel bit depth on the detector but did not exceed 70 mW at the objective back focal plane. YFP fluorescence was imaged by switching the filter cube (U-N41017XL Olympus) and using a mercury-vapor lamp (Olympus) for excitation.

Electrical and optical stimulation-evoked dopamine imaging with near-infrared microscopy

For electrical stimulation experiments, a bipolar stimulation electrode was positioned in field of view within the dorsomedial striatum identified using a 4X objective (Olympus xFluor 4x/340). Using 60X objective, the stimulation electrode was brought into contact with top surface of the brain slice and an imaging field of view was chosen at a nominal distance of 150 μm from the stimulation electrode within the dorsomedial striatum. All stimulation experiments were recorded at video frame rates of 9 frames per second (nominal) and single pulse electrical stimulations were applied after 200 frames of baseline were acquired. Each video acquisition lasted 600 frames. Stimulation amplitudes were staggered and each stimulation amplitude was repeated three times within a field of view. Slices were allowed to recover for 5 minutes between each stimulation with the excitation laser path shuttered. For optogenetic stimulation, a fiber-coupled 473 nm blue laser (OptoEngine LLC DPSS) was positioned in close proximity to the brain slice using a micromanipulator. Expression of ChR2 was confirmed via visible fluorescence imaging and an imaging field of view was chosen in dorsomedial striatum with robust expression level. Stimulation pulses (5 pulses, 5 ms duration per pulse, delivered at 25 Hz, 1 mW/mm^2) were delivered after acquiring 200 baseline frames and the video acquisition lasted 600 frames at nominal 9 frames per second. Drugs were bath applied to the imaging chamber through ACSF perfusion. ACSF with 10 μM of nomifensine or 1 μM of each DRD drug was used. When the effect of a drug needed to be evaluated, stimulation/imaging experiments were carried out with drug-free ACSF in an imaging field of view to collect drug-free data. Normal ACSF was then switched to ACSF prepared with the drug of interest and applied for 10 minutes before stimulation/imaging experiments resumed.

Viral transfection of mice for optogenetic stimulation

Adult male and female mice (>P60) were used for all surgeries. Bilateral viral injections were performed using previously described procedures [133] at the following stereotaxic coordinates: dorsomedial prefrontal cortex (dmPFC): 1.94 mm from Bregma, 0.34 mm lateral from midline, and 0.70 mm vertical from cortical surface; substantia nigra pars compacta (SNc): -3.08 mm from Bregma, 1.25 mm lateral from midline, and 4.0 mm vertical from cortical surface. For glutamatergic corticostriatal axon stimulation experiments, mice were injected with 0.5 μL of CAG-ChR2-EYFP virus bilaterally into dmPFC. For nigrostriatal dopaminergic axon stimulation experiments, DAT-Cre mice were injected with 0.5 μL DIO-ChR2-EYFP virus bilaterally. For all optogenetic experiments, we waited at least three weeks from viral injection to experimental stimulation to allow for sufficient ChR2 gene expression.

To confirm that dopamine neurons were transfected with ChR2 in animals used for optogenetic dopamine stimulation experiments, we perfused DAT-Cre mice that had been injected into the SNc with Cre-dependent ChR2-EYFP virus with 4% paraformaldehyde in PBS and post-fixed brains overnight. Coronal sections that included the injection site (SNc) and imaging site (dorsal striatum) were cut at 50 μM and immunolabeled using antibody against tyrosine hydroxylase (TH) (rabbit anti-TH 1:1000, Millipore), the rate-limiting enzyme for catecholamine synthesis. Goat anti-rabbit Dylight 594 secondary antibody

(1:1000, Invitrogen) was used to visualize TH. Image acquisition was performed on a Zeiss Axio ScanZ.1 using a 5x objective.

Image processing and data analysis for nIRCat fluorescence response

Raw movie files were processed using a custom-built MATLAB program (available for download: https://github.com/jtdbod/Nanosensor-Brain-Imaging). Briefly, for each raw movie stack (600 frames), a per pixel $\Delta F/F$ defined as $(F-F_0)/F_0$ was calculated using the average intensity for the first 5% of frames as F_0, and F represents the dynamic fluorescence intensity at each pixel. Regions of interest (ROIs) were identified by calculating a median filter convolution and then performing thresholding using Otsu's method to identify ROIs with strong fluorescence modulation over background, followed by a morphological dilation operation. $\Delta F/F$ traces were then calculated for each generated ROI by averaging pixel values over the ROI. ROI sizes were computed using the measured pixel area and approximating each as a circle to calculate an equivalent radius.

To compare responses across stimulation amplitudes and bath application of nomifensine, mean results were obtained as follows: First, all identified ROIs from a field of imaging were averaged. Mean traces were further averaged over different fields of view within the same slice and across slices (1-2 field of view per slice, 1-2 slices per animal) and then averaged over experimental animals. Decay time constants (τ) were computed by fitting $\Delta F/F$ time traces to a first order decay process on an ROI basis or field of view average basis. Latency to peak were computed as t_{peak} - t_{stim} where t_{peak} is the time at which peak signal is attained and t_{stim} is time of stimulation. All statistical tests of significance (p-values) were computed and reported from unpaired, two-tailed t-test.

ROI level analysis of drug washes were computed by generating an ROI mask from one of the triplicate stimulations, and then computing $\Delta F/F$ traces using the same ROI mask for all experimental runs (before and after application of drug). Each raw movie file was corrected for translational and rotational drift using StackReg plug-in in FIJI and then processed using our custom MATLAB script. We removed all ROIs that were greater than 4 μm in size for subsequent analysis. For each ROI, post-to-pre drug ratios were computed as $(\Delta F/F)_{\text{max-post-drug}}$ / $(\Delta F/F)_{\text{max-pre-drug}}$. Here, we define $(\Delta F/F)_{\text{max}}$ as the amplitude of nIRCat response in the post-stimulation epoch. Mean values from triplicate stimulation were used to evaluate the ratio.

5.5 Appendix II

Supporting Information

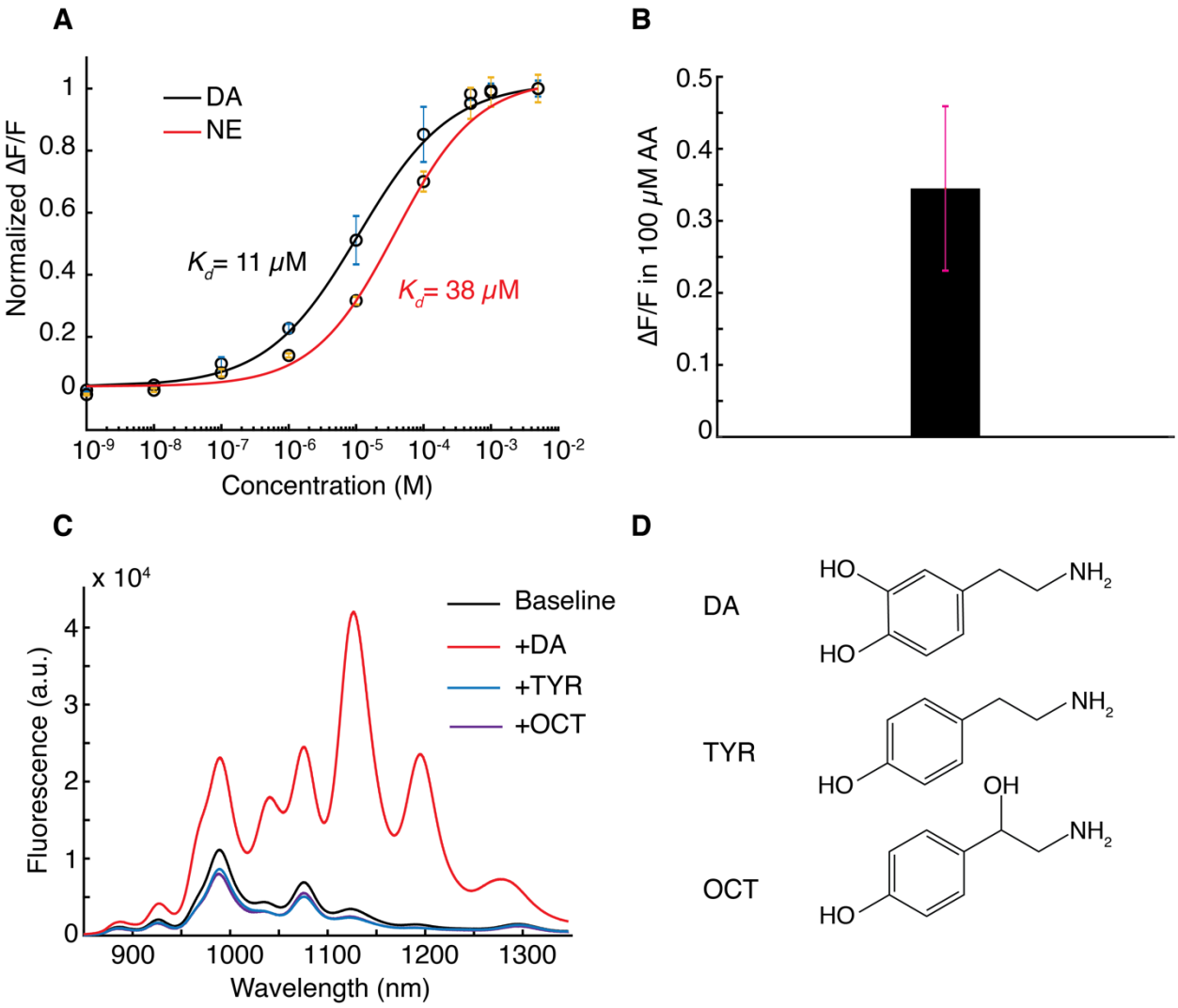

Figure 5.S1. nIRCats are compatible with concentrations and conditions expected in brain tissue. (**a**) *In vitro* (without tissue) normalized dose response curves of nIRCats for dopamine (DA) and norepinephrine (NE). Circles represent experimental measurements and solid lines represent Hill equation model fit to experimental data. Each measurement point is a mean of n=3 independent measurements with standard deviation error bars. ΔF/F is calculated from the normalized change in peak intensity at the center wavelength of the (9,4) chirality SWCNT (~1128 nm). (**b**) Response of nIRCats to 100 μM of DA after exposure to 100 μM of ascorbic acid (AA). ΔF/F is calculated from the change in peak intensity at the center wavelength of the (9,4) chirality SWCNT (~1128 nm). (**c**) Fluorescence spectra of nIRCats before (black) and after addition of 10 μM of dopamine (red, DA), tyramine (blue, TYR) and octopamine (purple, OCT) in an *in vitro* preparation in phosphate buffered saline (without tissue). (**d**) Molecular structures of dopamine (DA), tyramine (TYR) and octopamine (OCT).

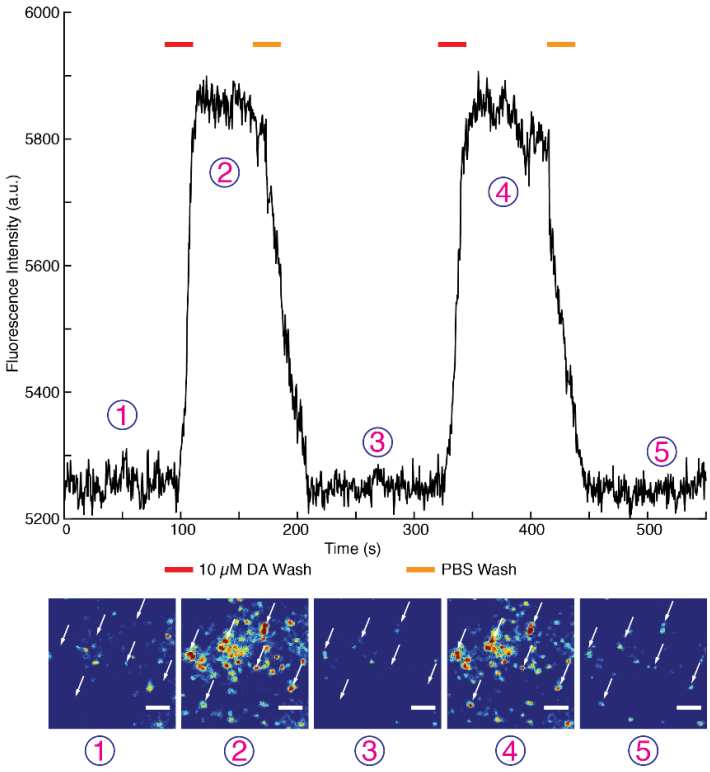

Figure 5.S2. Surface immobilized single nIRCats are reversible upon repeat exposure to dopamine. nIRCats are immobilized in a microfluidic device and imaged with a 100 X objective (Zeiss Plan Apochromat 1.4 NA ; Methods). After acquiring baseline nIRCat fluorescence (1), exposure to 10 μM dopamine (red bar) results in a nIRCat fluorescence turn-on response (2). The response is preserved while dopamine remains in the imaging chamber but is reversed when dopamine is replaced by phosphate buffered saline (PBS wash; yellow bar) and baseline nIRCat fluorescence is recovered (3). The experiment is repeated in (4) and (5). Bottom row shows diffraction-limited images of surface-immobilized nIRCats suggesting individual nanosensors undergo reversible turn-on response. The data trace presented is averaged fluorescence from all nIRCats in the field of view. Scale bars = 5 μm.

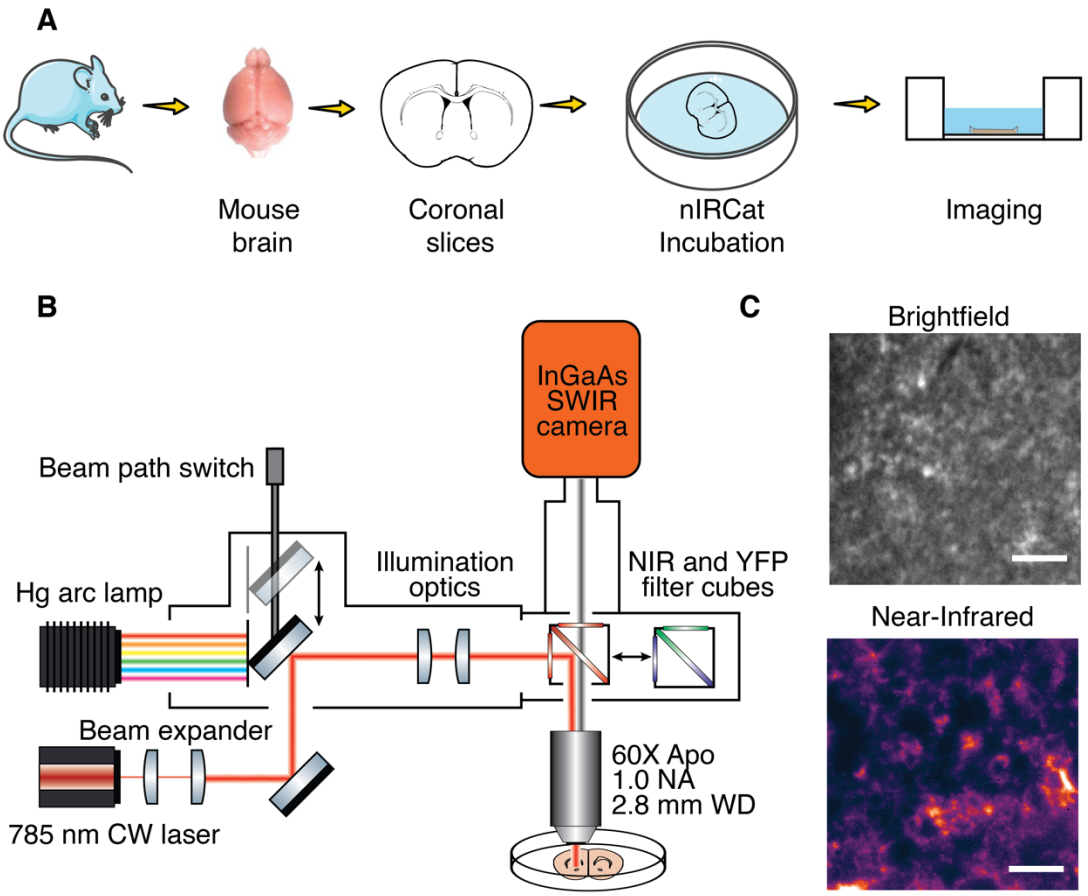

Figure 5.S3 Brain slice nIRCat loading protocol and schematic of visible and near-infrared fluorescence microscopy for imaging nIRCats in brain tissue. (**a**) Experimental schematic depicting preparation of acute brain slices and subsequent incubation in 2 mg/L nIRCat solution to load the nanosensors into brain tissue. (**b**) Schematic of visible/near-infrared microscope. A 785 nm CW laser is beam-expanded and co-aligned with a mercury vapor lamp and directed into the objective with dichroic filter cubes. Emitted photons are filtered through a 900 nm long-bass filter and are relayed onto the sensor of a broadband InGaAs camera that is sensitive to both visible and near-infrared wavelengths. (**c**) Dorsomedial striatum from mouse acute slice imaged in brightfield (top) and near-infrared (bottom) after tissue nanosensor loading. Scale bars = 10 μm.

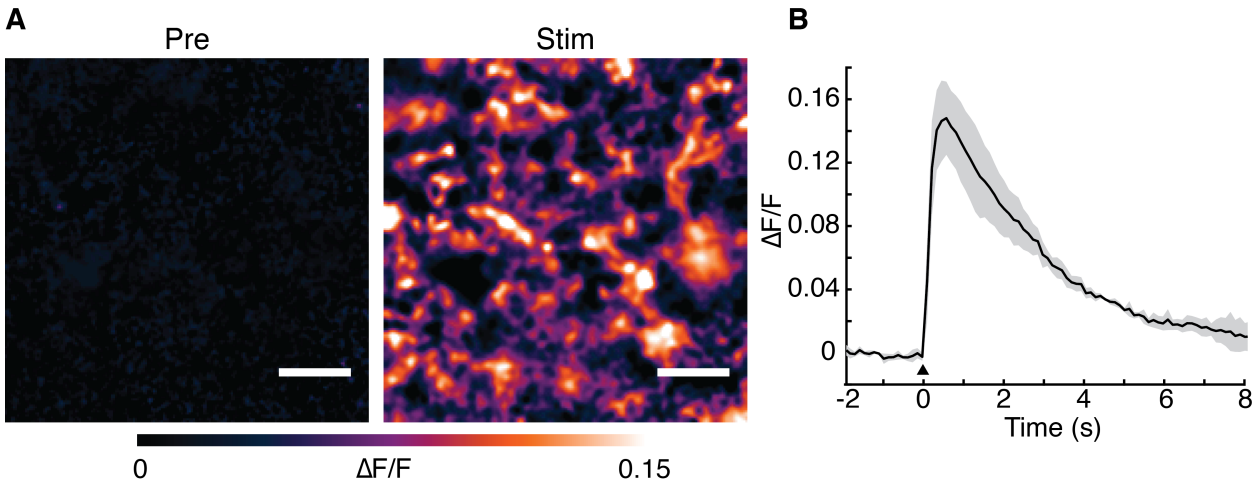

Figure 5.S4 nIRCat imaging in Mus spicilegus brain tissue (**a**) nIRCat ΔF/F average trace in response to single electrical pulse (3 ms, 0.3 mA) in the dorsolateral striatum. Pre-stimulation ("Pre") nIRCat ΔF/F image and nIRCat ΔF/F response after stimulation ("Stim") show nIRCat fluorescence modulation. Scale bars = 10 μm. (**b**) ΔF/F time trace from triplicate stimulation run. Mean trace and standard deviation bands around the mean are shown.

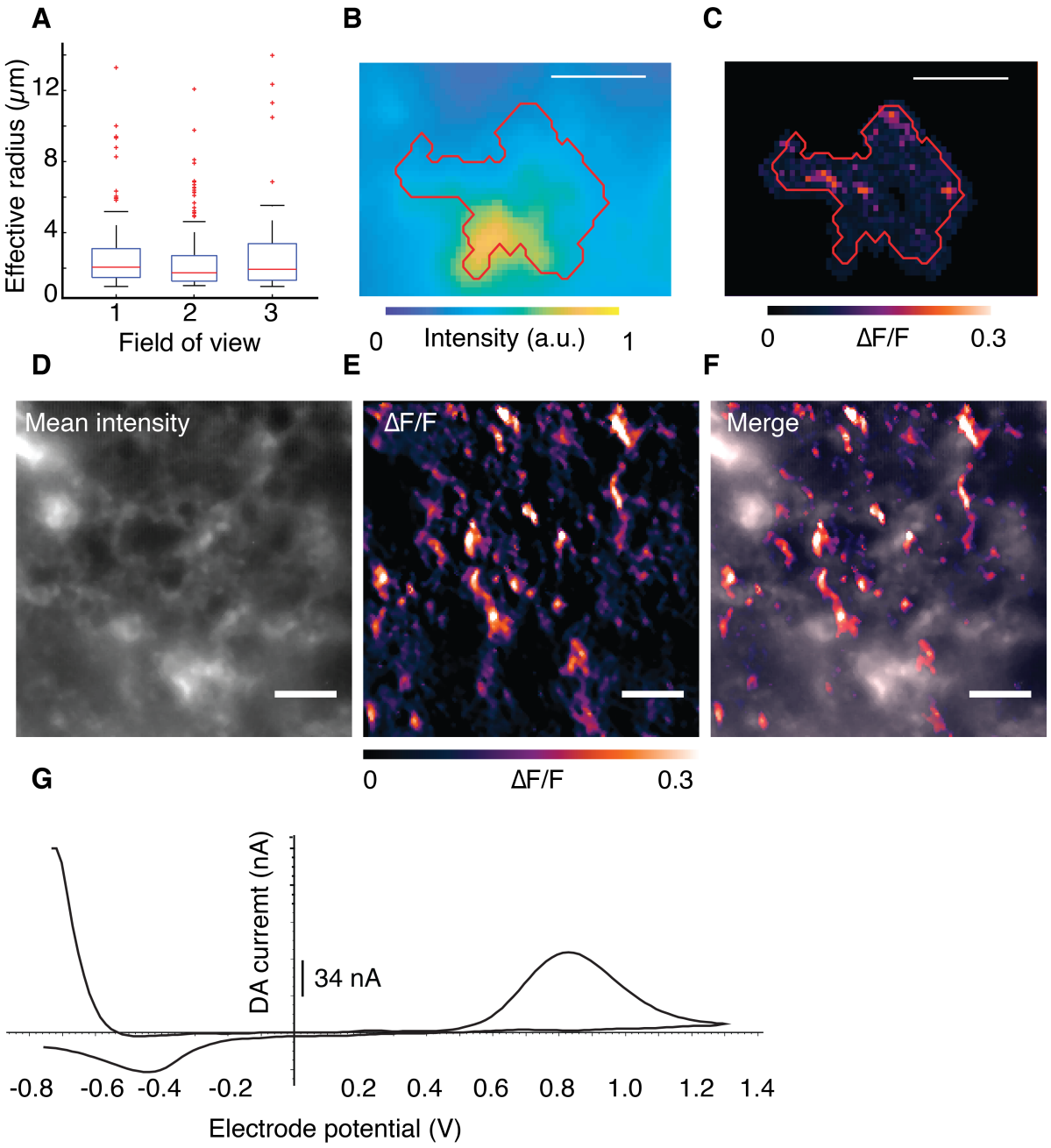

Figure 5.S5 Intensity of nIRCat labeling at baseline does not predict site of ΔF/F hotspots. (**a**) ROI size distribution from three different fields of view (representing n = 3 biological replicates) in the dorsal striatum, each stimulated separately by 0.3 mA stimulation. In each of these fields of view, ROIs showed similar median size and size distribution even when compared across biological replicates. Box plot definitions: red-line = median, edges of box: 25th and 75th percentiles, top and bottom lines: minimum and maximum values of non-outlier data, red points: outlier data. (**b**) Mean intensity projection at a region of interest and its maximum ΔF/F projection shown in (**c**) show labeling intensity does not predict ΔF/F hot spots. Scale bars in (b) and (c) = 5 μm. (**d**) Bulk loading of nIRCats into striatal tissue yields heterogeneous nanosensor distribution in tissue at baseline. Mean intensity projection of nIRCat tissue labeling in a representative dorsal striatal section after bulk loading and during baseline imaging. (**e**) ΔF/F in nIRCat signal in the same field of view as (D), 0.5 sec after 0.3 mA single pulse electrical stimulation. (**f**) Overlay of mean intensity projection of nIRCat labeling at baseline

and evoked change in ΔF/F reveals that areas with higher nIRCat labeling at baseline do not predict hotspots in evoked ΔF/F. Scale bars in (d-f) = 10 μm. (**g**) Representative voltammogram of FSCV measurements made in this study confirms evoked signal is dopamine.

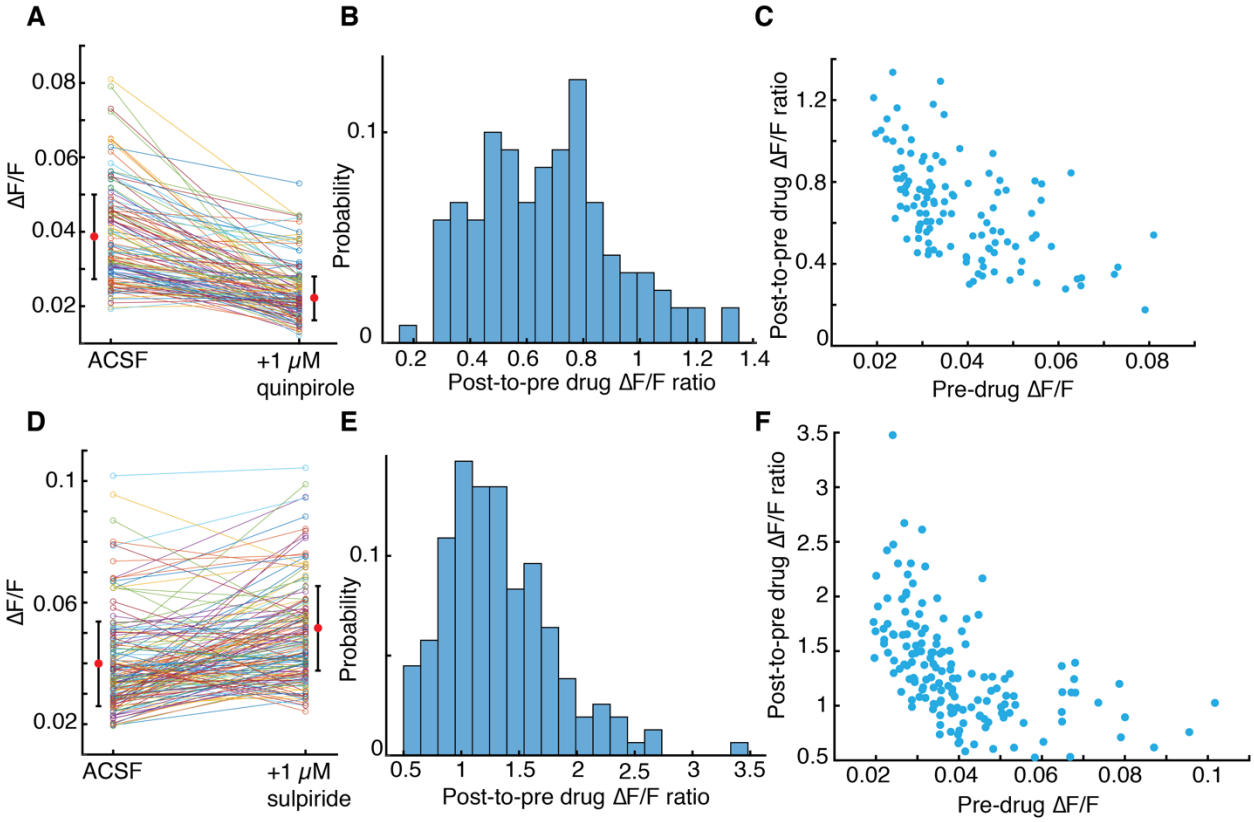

Figure 5.S6 Variability in effect of quinpirole and sulpiride on nIRCat response on spatially segregated ROIs within a field of view. (**a**) ΔF/F of ROIs in ACSF and in ACSF with 1 μM of quinpirole. Each ΔF/F data point corresponding to an ROI is an average from n=3 repeat stimulations. (**b**) Distribution of post-to-pre drug ratio for data in (**a**) with mean = 0.67 ± 0.24 (n=120 ROIs identified within the field of view) (**c**) Scatter plot of ROIs in (**a**) shows a negative correlation between the pre-drug ΔF/F amplitude of an ROI and its post-to-pre drug ΔF/F amplitude ratio (r = -0.57, p < 0.0001). (**d**) ΔF/F of ROIs in ACSF and in ACSF with 1 μM of sulpiride. Each ΔF/F data point corresponding to an ROI is an average from n=3 repeat stimulations. (**e**) Distribution of post-to-pre drug ratio for data in (**d**) with mean = 1.38 ± 0.49 (n=165 ROIs identified within the field of view). (**f**) Scatter plot for ROIs in (**d**) shows a negative correlation between the pre-drug ΔF/F amplitude of an ROI and its post-to-pre drug ΔF/F amplitude ratio (r = -0.53, p < 0.0001). All ROIs in (A-F) had sizes in the range of 1 – 4 μm.

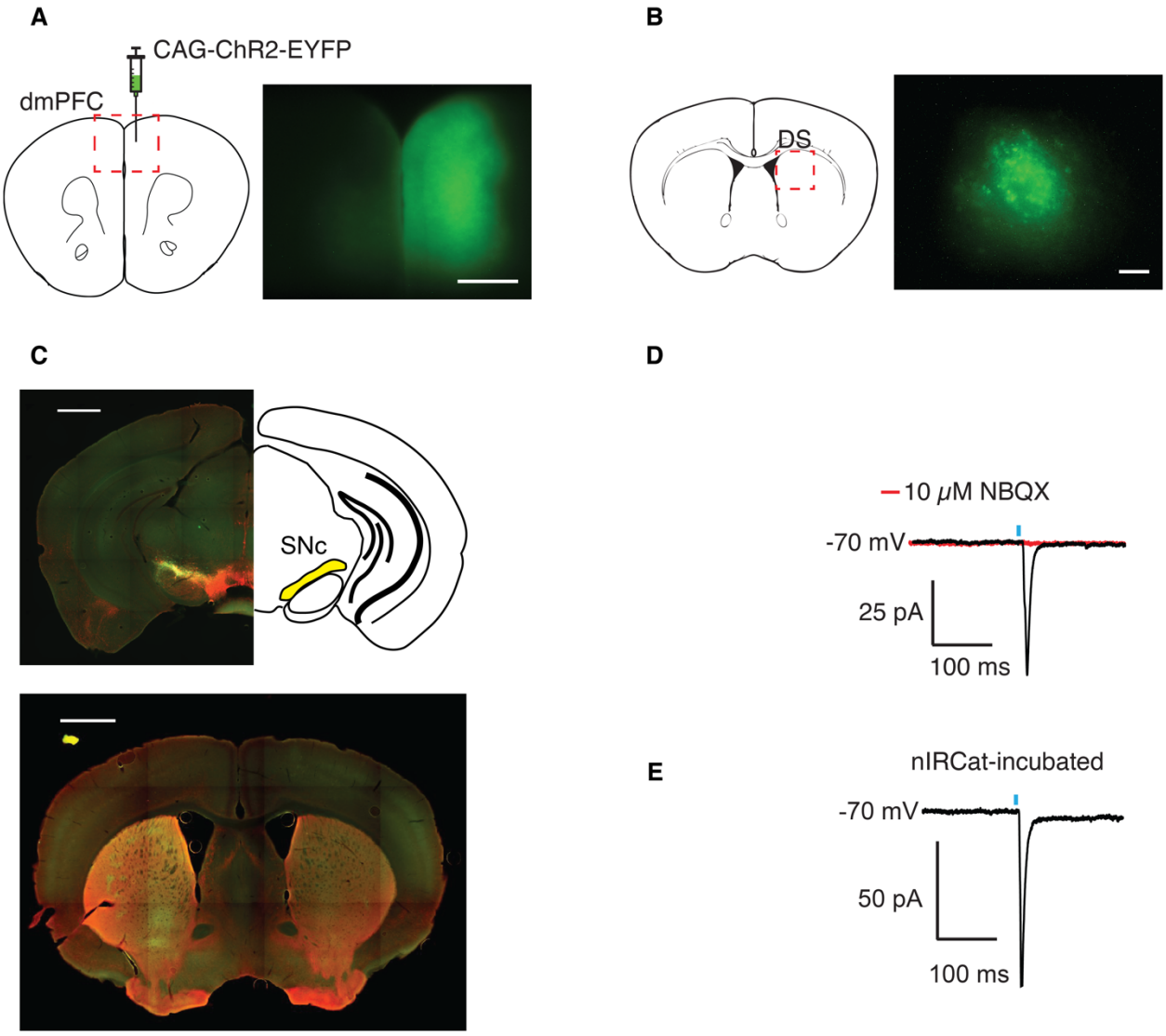

Figure 5.S7 Data which confirm targeting of optogenetic stimulation of dopaminergic and glutamatergic inputs to the striatum (**a**) Left: Schematic of AAV-CAG-ChR2-EYFP injection into dorsal medial prefrontal cortex (dmPFC). Right: Fluorescence image collected confirming ChR2-EYFP expression at injection site. Scale bar = 500 μM. (**b**) Left**:** Schematic of imaging site of corticostriatal axon terminals in DS. Right: ChR2-EYFP+ corticostriatal terminals present in the DS collected in nIR/visible imaging rig prior to imaging experiment (nIRCat imaging data in Figure 5b). Scale bar = 20 μM. (**c**) Top: Fluorescence image of tyrosine hydroxylase (TH) positive dopamine neurons in the substantia nigra pars compact (SNc) and dopamine terminals in the dorsal striatum (DS). AAV-DIO-CHR2-EYFP injection into SNc of DAT-Cre mouse shows successful viral delivery as evidenced by colocalization of CHR2-EYFP and anti-TH RFP. Bottom: Projections from the SNc into the DS confirms expression of ChR2 in dopaminergic terminals and TH staining confirms dopaminergic identity. Scale bars = 1 mm. (**d**) Sample trace of 473 nm light pulse (2 ms) evoked excitatory postsynaptic current (EPSC) recorded in medium spiny neuron in DS. Application of 10 μM NBQX abolishes current, confirming that it is AMPAR-mediated/glutamatergic. (**e**) Sample trace of 473 nm light pulse (2 ms) evoked EPSC recorded in medium spiny neuron from striatal slice pre-incubated in 2 mg/L nIRCat, indicating that nIRCat does not interfere with opto-evoked glutamate release.

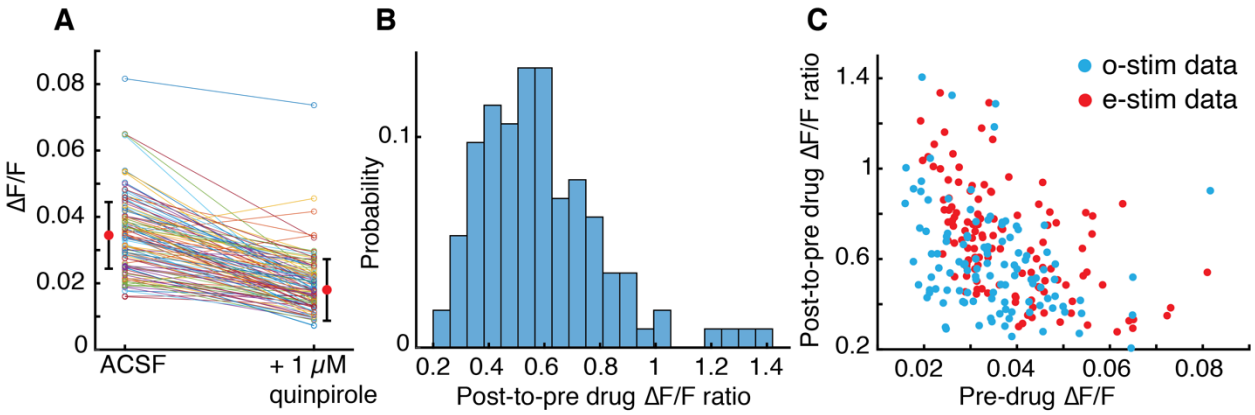

Figure 5.S8 Effect of quinpirole on ChR2 evoked nIRCat response at the level of ROIs. (**a**) ΔF/F of ROIs in ACSF and in ACSF with 1 μM of quinpirole. Each ΔF/F data point corresponding to an ROI is an average from n=3 repeat stimulations with 5 light pulses at 25 Hz. (**b**) Distribution of post-to-pre drug ratio for data in (a) with mean = 0.59 ± 0.22 (n=113 ROIs identified within the field of view). (**c**) Scatter plot for ROIs in (**A**) shows a negative correlation between the pre-drug ΔF/F amplitude of an ROI and its post-to-pre drug ΔF/F amplitude ratio (r = -0.32, p < 0.001) (blue dots). The electrical stimulation data from figure S5C is reproduced here for comparison (red dots). All ROIs in (**a-c**) had sizes in the range of 1 – 4 μm.

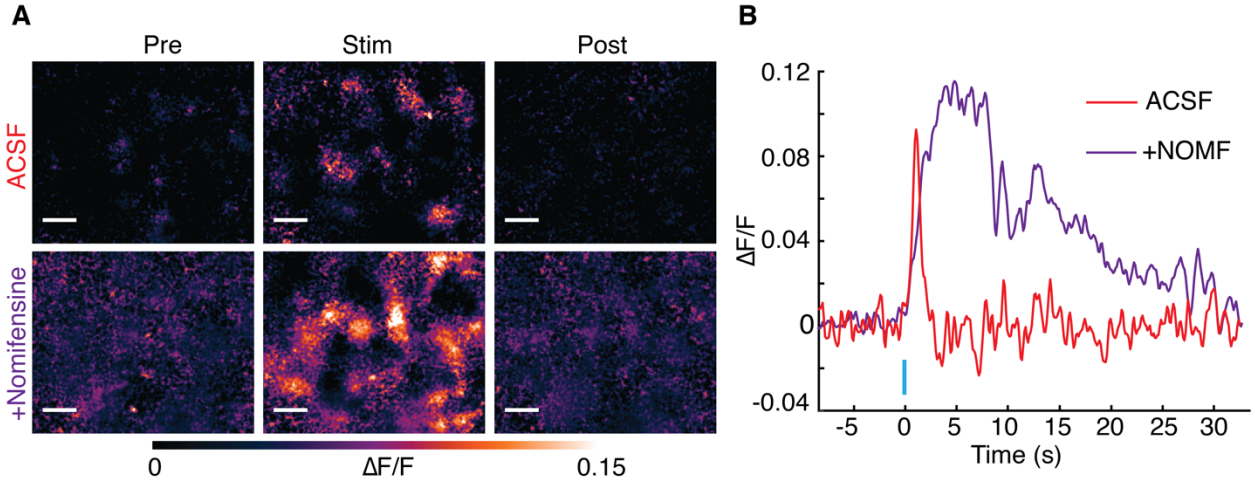

Figure 5.S9. Nomifensine extends nIRCat response to ChR2 stimulation of dopaminergic terminals in the dorsal striatum. (**a**) Top: Representative "Pre", "Stim", and "Post" snapshots from movie stack represent nIRCat fluorescence modulation before, during, and after blue light stimulation (5 pulses, 25 Hz, 1 mW/mm^2) in standard ACSF. Bottom: After 10 min incubation in 10 μM of nomifensine, the ChR2 evoked response shows brighter and broader nIRCat fluorescence modulation. (**b**) Representative traces of nIRCat response averaged over the field of view from (**a**) in ACSF and ACSF with nomifensine (+NOMF). Decay time constants are τ_{ACSF} = 0.8 s and $\tau_{Nomifensine}$ = 11.7 s. These data show that nomifensine can prolong nIRCat signal decay. Scale bars = 10 μm.

Chapter 6

6.1 Summary

This dissertation described a comprehensive computational and experimental approach for developing and implementing an optical probe for the catecholamines dopamine and norepinephrine, based on a synthetic fluorescent scaffold that possesses favorable photophysical attributes for imaging in biological specimens.

In the first part of this dissertation, theoretical approaches were utilized to gain insight into the spatiotemporal dynamics of dopamine in brain tissue. This early work was important in outlining the optimal binding kinetics for probes targeted to dopamine, which had hitherto been insufficiently understood. Among the findings from this study was the counterintuitive conclusion that high affinity probes (with K_d < 10 nM) are unfavorable because they are likely to saturate at basal striatal dopamine levels, which arise from tonic dopaminergic activity and pervade neural tissue at rest. Our simulation quantified this basal dopamine level and showed that high affinity probes are likely to exhibit diminished dynamic range upon implementation because of sensor pre-saturation. Furthermore, high affinity leads to delayed clearance profiles following transient events, which could be detrimental to probe's temporal resolution. We identified probes with affinity (K_d)on the order of 1μM as optimal indicators for measuring dopaminergic dynamics in the dorsomedial striatum, which accurately recapitulated the underlying biological signal. Moreover, with this simulation work, we elucidated the spatial extent of dopamine spillover from single release sites, which enabled exploration of probe placement with respect to release sites. Learnings from this work provided critical guidance for subsequent experimental portions of this dissertation, which encompassed probe synthesis, validation and implementation.

Single wall carbon nanotubes (SWCNT) were chosen as novel scaffolds for optical probe synthesis because of their favorable photophysics. Previous work had demonstrated that supramolecular complexes that assemble on the surface of SWCNT can self-organize into structural motifs that can bind small molecule analytes and modulate the fluorescence of the underlying SWCNT scaffold. However, much of the existing literature focused on *in vitro* solution phase experiments and applied the probes in simple biological systems under highly controlled conditions. In contrast, this dissertation introduced a comprehensive approach for developing and implementing SWCNT-based optical probes for use in realistic biological preparations. Towards this goal, several concurrent advances were made. Using our computational study, we showed quantitatively that neurochemical signals are highly transient and occur in confined spatiotemporal domains. In other words, chemical communication between neurons occurs in "temporal bursts" in "spatially localized" domains. In order to capture these events for dopamine, we developed a probe with a moderate affinity that minimized the risk of sensor saturation ($K_d \approx 10$ μM) but nonetheless underwent ultrastrong fluorescence modulation (up to 20-fold increase for 100 μM dopamine). This afforded imaging "temporally confined" signals at video frame rates with decent signal-to-noise ratio (SNR > 5 for most imaging experiments). To ensure that we can capture neurochemical bursts appropriately in the spatial domain, we developed a sensor loading strategy that generated *ex vivo* mice brain slices with relatively uniform probe

labeling. With this labeling strategy, we recorded dynamical information about endogenous dopamine at putative release sites in the dorsomedial striatum of *ex vivo* mice brain tissue.

The SWCNT-based technology presented in this dissertation captured electrically and optogenetically evoked releases of dopamine in the dorsomedial striatum, revealing hotspots of activity that exhibited a log-normal distribution in size, ranging from 2 – 10 μm for mice brain tissue. Moreover, the synthetic nature of the molecular recognition platform afforded compatibility with dopamine-receptor targeting antipsychotics and psychoactive drugs and permitted studies of how such receptor-targeting drugs modulate evoked dopamine release. This assay revealed presynaptic correlates of pharmacodynamics at the level of putative dopamine release sites, which had heretofore been impossible to explore with existing tools. Our results suggest that this technology may uniquely support similar explorations of processes that regulate dopamine neuromodulation at the level of individual synapses, and exploration of the effects of receptor agonists and antagonists that are commonly used as psychiatric drugs as well as those that lead to substance use disorder. We conclude that SWCNTs can serve as versatile synthetic optical tools to monitor interneuronal chemical signaling in the brain extracellular space at spatial and temporal scales pertinent with the encoded information.

References

1. Beyene, A. G., Delevich, K., Yang, S. J. & Landry, M. P. New Optical Probes Bring Dopamine to Light. *Biochemistry* (2018). doi:10.1021/acs.biochem.8b00883
2. Marvin, J. S., Borghuis, B.G., Tian, L., Cichon, J. Looger, L.L. An optimized fluorescent probe for visualizing glutamate neurotransmission. *Nat. Methods* **10,** 162–170 (2013).
3. Patriarchi, T., Cho, R.J., Merten, K., Howe, M.W., Tian, L. Ultrafast neuronal imaging of dopamine dynamics with designed genetically encoded sensors. *Science (80-.).* (2018). doi:10.1126/science.aat4422
4. Sun, F., Zeng, J., Jing, M., Zhou, J., Feng, J., Li, Y. A Genetically Encoded Fluorescent Sensor Enables Rapid and Specific Detection of Dopamine in Flies, Fish, and Mice. *Cell* (2018). doi:10.1016/j.cell.2018.06.042
5. Beyene, A. G., McFarlane, I. R., Pinals, R. L. & Landry, M. P. Stochastic Simulation of Dopamine Neuromodulation for Implementation of Fluorescent Neurochemical Probes in the Striatal Extracellular Space. *ACS Chem. Neurosci.* (2017). doi:10.1021/acschemneuro.7b00193
6. Yung, K. K., Bolam, J.P., Smith, A.D., Hersch, S.M., Ciliax, B.J., Levey, A.I. Immunocytochemical localization of D 1 and D 2 dopamine receptors in the basal ganglia of the rat: Light and electron microscopy. *Neuroscience* (1995). doi:10.1016/0306-4522(94)00536-E
7. Bolam, J. P., Hanley, J. J., Booth, P. A. C. & Bevan, M. D. Synaptic organisation of the basal ganglia. *Journal of Anatomy* (2000). doi:10.1017/S0021878299005944
8. Gerfen, C. R. Synaptic organization of the striatum. *J. Electron Microsc. Tech.* (1988). doi:10.1002/jemt.1060100305
9. Davie, C. A. A review of Parkinson's disease. *British Medical Bulletin* (2008). doi:10.1093/bmb/ldn013
10. Cabib, S. & Puglisi-Allegra, S. Stress, depression and the mesolimbic dopamine system. *Psychopharmacology* (1996). doi:10.1007/s002130050142
11. Grace, A. A. Phasic versus tonic dopamine release and the modulation of dopamine system responsivity: A hypothesis for the etiology of schizophrenia. *Neuroscience* (1991). doi:10.1016/0306-4522(91)90196-U
12. Li, D., Sham, P. C., Owen, M. J. & He, L. Meta-analysis shows significant association between dopamine system genes and attention deficit hyperactivity disorder (ADHD). *Hum. Mol. Genet.* (2006). doi:10.1093/hmg/ddl152
13. Kalivas, P. W. & Volkow, N. D. The neural basis of addiction: A pathology of motivation and choice. *American Journal of Psychiatry* (2005). doi:10.1176/appi.ajp.162.8.1403
14. Weinberger, D. R. Implications of Normal Brain Development for the Pathogenesis of Schizophrenia. *Arch. Gen. Psychiatry* (1987). doi:10.1001/archpsyc.1987.01800190080012
15. Agnati, L. F., Zoli, M., Strömberg, I. & Fuxe, K. Intercellular communication in the brain: Wiring versus volume transmission. *Neuroscience* (1995). doi:10.1016/0306-4522(95)00308-6

16. Alivisatos, A. P., Andrews, A.M, Boyden, E.S., Chun, M., Church, G.M., Deisseroth, K. Nanotools for neuroscience and brain activity mapping. *ACS Nano* (2013). doi:10.1021/nn4012847
17. Garris, P. A. Advancing neurochemical monitoring. *Nature Methods* (2010). doi:10.1038/nmeth0210-106
18. Muller, A., Joseph, V., Slesinger, P. A. & Kleinfeld, D. Cell-based reporters reveal in vivo dynamics of dopamine and norepinephrine release in murine cortex. *Nat. Methods* **11,** 1245–1252 (2014).
19. Gubernator, N. G. Zhang, H., Staal, R.G., Mosharov, E.V., Pereira, D.B., Sulzer, D., Sames, D. Fluorescent false neurotransmitters visualize dopamine release from individual presynaptic terminals. *Science (80-.).* (2009). doi:10.1126/science.1172278
20. Pereira, D. B., Schmitz Y., Meszaros, J., Mechant, P., Sames, D., Sulzer, D. Fluorescent false neurotransmitter reveals functionally silent dopamine vesicle clusters in the striatum. *Nat. Neurosci.* (2016). doi:10.1038/nn.4252
21. Sames, D., Dunn, M., Karpowicz, R. J. & Sulzer, D. Visualizing neurotransmitter secretion at individual synapses. *ACS Chemical Neuroscience* (2013). doi:10.1021/cn4000956
22. Lin, M. Z. & Schnitzer, M. J. Genetically encoded indicators of neuronal activity. *Nature Neuroscience* (2016). doi:10.1038/nn.4359
23. Bando, Y., Sakamoto, M., Kim, S., Ayzenshtat, I. & Yuste, R. Comparative Evaluation of Genetically Encoded Voltage Indicators. *Cell Rep.* (2019). doi:10.1016/j.celrep.2018.12.088
24. Freund, T. F., Powell, J. F. & Smith, A. D. Tyrosine hydroxylase-immunoreactive boutons in synaptic contact with identified striatonigral neurons, with particular reference to dendritic spines. *Neuroscience* (1984). doi:10.1016/0306-4522(84)90294-X
25. Arluison, M., Dietl, M. & Thibault, J. Ultrastructural morphology of dopaminergic nerve terminals and synapses in the striatum of the rat using tyrosine hydroxylase immunocytochemistry: A topographical study. *Brain Res. Bull.* (1984). doi:10.1016/0361-9230(84)90128-X
26. Doucet, G., Descarries, L. & Garcia, S. Quantification of the dopamine innervation in adult rat neostriatum. *Neuroscience* (1986). doi:10.1016/0306-4522(86)90272-1
27. Oorschot, D. E. Total number of neurons in the neostriatal, pallidal, subthalamic, and substantia nigral nuclei of the rat basal ganglia: A stereological study using the cavalieri and optical disector methods. *J. Comp. Neurol.* (1996). doi:10.1002/(SICI)1096-9861(19960318)366:4<580::AID-CNE3>3.0.CO;2-0
28. Iversen, L., Iversen, S., Dunnett, S. & Bjorklund, A. *Dopamine Handbook*. *Dopamine Handbook* (2010). doi:10.1093/acprof:oso/9780195373035.001.0001
29. Rice, M. E. & Cragg, S. J. Dopamine spillover after quantal release: Rethinking dopamine transmission in the nigrostriatal pathway. *Brain Research Reviews* (2008). doi:10.1016/j.brainresrev.2008.02.004
30. Dreyer, J. K., Herrik, K. F., Berg, R. W. & Hounsgaard, J. D. Influence of Phasic and Tonic Dopamine Release on Receptor Activation. *J. Neurosci.* (2010). doi:10.1523/JNEUROSCI.1894-10.2010
31. Nicholson, C. Diffusion and related transport mechanisms in brain tissue. *Reports Prog. Phys.* (2001). doi:10.1088/0034-4885/64/7/202

32. Arbuthnott, G. W. & Wickens, J. Space, time and dopamine. *Trends in Neurosciences* (2007). doi:10.1016/j.tins.2006.12.003
33. Stevens, C. F. Neurotransmitter release at central synapses. *Neuron* (2003). doi:10.1016/S0896-6273(03)00643-3
34. Rosenmund, C. & Stevens, C. F. Definition of the readily releasable pool of vesicles at hippocampal synapses. *Neuron* (1996). doi:10.1016/S0896-6273(00)80146-4
35. Nicholson, C. Interaction between diffusion and Michaelis-Menten uptake of dopamine after iontophoresis in striatum. *Biophys. J.* (1995). doi:10.1016/S0006-3495(95)80348-6
36. Rice, M. E. & Nicholson, C. Diffusion characteristics and extracellular volume fraction during normoxia and hypoxia in slices of rat neostriatum. *J. Neurophysiol.* (1991). doi:10.1152/jn.1991.65.2.264
37. Ross, S. B. Synaptic Concentration of Dopamine in the Mouse Striatum in Relationship to the Kinetic Properties of the Dopamine Receptors and Uptake Mechanism. *J. Neurochem.* (1991). doi:10.1111/j.1471-4159.1991.tb02557.x
38. Richfield, E. K., Penney, J. B. & Young, A. B. Anatomical and affinity state comparisons between dopamine D1 and D2 receptors in the rat central nervous system. *Neuroscience* (1989). doi:10.1016/0306-4522(89)90168-1
39. Syková, E. & Nicholson, C. Diffusion in brain extracellular space. *Physiological Reviews* (2008). doi:10.1152/physrev.00027.2007
40. Jones, S. R., Garris, P. A. & Wightman, R. M. Different effects of cocaine and nomifensine on dopamine uptake in the caudate-putamen and nucleus accumbens. *J. Pharmacol. Exp. Ther.* (1995).
41. Grace, A. A. & Bunney, B. S. The control of firing pattern in nigral dopamine neurons: Single spike firing. *J. Neurosci.* (1984). doi:10.1523/jneurosci.04-11-02866.1984
42. Grace, A. A. & Bunney, B. S. The control of firing pattern in nigral dopamine neurons: Burst firing. *J. Neurosci.* (1984). doi:10.1523/jneurosci.04-11-02877.1984
43. Hyland, B. I., Reynolds, J. N. J., Hay, J., Perk, C. G. & Miller, R. Firing modes of midbrain dopamine cells in the freely moving rat. *Neuroscience* (2002). doi:10.1016/S0306-4522(02)00267-1
44. Schultz, W. Predictive reward signal of dopamine neurons. *Journal of Neurophysiology* (1998). doi:10.1152/jn.1998.80.1.1
45. Venton, B. J. Zhang, H., Garris, P.A., Phillips, P.E., Sulzer, D., Wightman, R.M. Real-time decoding of dopamine concentration changes in the caudate-putamen during tonic and phasic firing. *J. Neurochem.* (2003). doi:10.1046/j.1471-4159.2003.02109.x
46. Kruss, S., Landry, M.P., Vander Ende, E., Lima, B.M.A., Reuel, N.F., Strano, M. Neurotransmitter detection using corona phase molecular recognition on fluorescent single-walled carbon nanotube sensors. *J. Am. Chem. Soc.* (2014). doi:10.1021/ja410433b
47. Godin, A. G. Varela, J.A., Gai, Z., Danne, N., Lounis, B., Groc, L., Cognet, L. Single-nanotube tracking reveals the nanoscale organization of the extracellular space in the live brain. *Nat. Nanotechnol.* (2017). doi:10.1038/nnano.2016.248
48. Ngo, K. T., Varner, E. L., Michael, A. C. & Weber, S. G. Monitoring Dopamine Responses to Potassium Ion and Nomifensine by in Vivo Microdialysis with Online Liquid Chromatography at One-Minute Resolution. *ACS Chem. Neurosci.* (2017). doi:10.1021/acschemneuro.6b00383

49. Gu, H., Varner, E. L., Groskreutz, S. R., Michael, A. C. & Weber, S. G. In Vivo Monitoring of Dopamine by Microdialysis with 1 min Temporal Resolution Using Online Capillary Liquid Chromatography with Electrochemical Detection. *Anal. Chem.* (2015). doi:10.1021/acs.analchem.5b00633
50. Berger, A. E., Ciment, M. & Rogers, J. C. W. NUMERICAL SOLUTION OF A DIFFUSION CONSUMPTION PROBLEM WITH A FREE BOUNDARY. *SIAM J. Numer. Anal.* (1975). doi:10.1137/0712049
51. Beyene, A. G., Alizadehmojarad, A.A., Dorlhiac, G., Goh, N., Streets, A.M., Kral, P., Vukovic, L., Landry, M.P. Ultralarge Modulation of Single Wall Carbon Nanotube Fluorescence Mediated by Neuromodulators Adsorbed on Arrays of Oligonucleotide Rings. *Nano Lett.* (2018). doi:10.1101/351627
52. Kang, S. J., Kocabas, C., Ozel, T., Shim, M., Pimparkar, N., Alam, M.A., Rotkin, S.V., Rogers, J.A. High-performance electronics using dense, perfectly aligned arrays of single-walled carbon nanotubes. *Nat. Nanotechnol.* (2007). doi:10.1038/nnano.2007.77
53. McEuen, P. L., Fuhrer, M. S. & Park, H. Single-walled carbon nanotube electronics. *Nanotechnology, IEEE Trans.* (2002). doi:10.1109/TNANO.2002.1005429
54. Baughman, R. H., Zakhidov, A. A. & De Heer, W. A. Carbon nanotubes - The route toward applications. *Science* (2002). doi:10.1126/science.1060928
55. LeMieux, M. C., Roberts, M., Barman, S., Jin, Y.W., Kim, J.M., Bao, Z. Self-sorted, aligned nanotube networks for thin-film transistors. *Science (80-.).* (2008). doi:10.1126/science.1156588
56. He, X., Hartmann, N.F., Ma, X., Kim, Y., Ihly, R., Htoon, H., Doorn, S.K. Tunable room-Temperature single-photon emission at telecom wavelengths from sp 3 defects in carbon nanotubes. *Nat. Photonics* (2017). doi:10.1038/nphoton.2017.119
57. Barone, P. W., Baik, S., Heller, D. A. & Strano, M. S. Near-infrared optical sensors based on single-walled carbon nanotubes. *Nat. Mater.* (2005). doi:10.1038/nmat1276
58. Satishkumar, B. C., Brown, L.O., Gao, Y., Wang, C.C., Doorn, S. Reversible fluorescence quenching in carbon nanotubes for biomolecular sensing. *Nat. Nanotechnol.* (2007). doi:10.1038/nnano.2007.261
59. Oliveira, S. F., Bisker, G., Bakh, N.A., Gibbs, S.L., Landry, M.P., Strano, M.S. Protein functionalized carbon nanomaterials for biomedical applications. *Carbon* (2015). doi:10.1016/j.carbon.2015.08.076
60. Zhang, J., Landry, M.P., Barone, P.W., Strano, M.S. Molecular recognition using corona phase complexes made of synthetic polymers adsorbed on carbon nanotubes. *Nat. Nanotechnol.* (2013). doi:10.1038/nnano.2013.236
61. Pu, K., Shuhendler, A.J., Jokerst, J.V., Bao, Z., Rao, J. Semiconducting polymer nanoparticles as photoacoustic molecular imaging probes in living mice. *Nat Nano* (2014). doi:10.1038/nnano.2013.302\rhttp://www.nature.com/nnano/journal/v9/n3/abs/nnano.2013.302.html#supplementary-information
62. Bonis-O'Donnell, J. T. D., Page, R.H., Beyene, A.G., Landry, M.P. Dual Near-Infrared Two-Photon Microscopy for Deep-Tissue Dopamine Nanosensor Imaging. *Adv. Funct. Mater.* (2017). doi:10.1002/adfm.201702112
63. Hong, G., Diao, S., Chang, J., Dai, H. Through-skull fluorescence imaging of the brain in a new near-infrared window. *Nat. Photonics* (2014). doi:10.1038/nphoton.2014.166

64. Král, P. & Wang, B. Material drag phenomena in nanotubes. *Chemical Reviews* (2013). doi:10.1021/cr200244h
65. Geng, J., Kim, K., Zhang, J., Escalada, A., Noy, A. Stochastic transport through carbon nanotubes in lipid bilayers and live cell membranes. *Nature* (2014). doi:10.1038/nature13817
66. Holt, J. K., Park, H.G., Wang, Y., Noy, A., Bakajin, O. Fast mass transport through sub-2-nanometer carbon nanotubes. *Science (80-.).* (2006). doi:10.1126/science.1126298
67. Cognet, L., Tsyboulski, D.A, Rocha, J.D.R, Tour, J.M., Weisman, R.B. Stepwise quenching of exciton fluorescence in carbon nanotubes by single-molecule reactions. *Science (80-.).* (2007). doi:10.1126/science.1141316
68. Dukovic, G., White, B., Zhou, Z., Wang, F., Brus, L.E. Reversible surface oxidation and efficient luminescence quenching in semiconductor single-wall carbon nanotubes. *J. Am. Chem. Soc.* (2004). doi:10.1021/ja046526r
69. Lee, A. J., Wang, X., Carlson, L.J., Zheng, M., Krauss, T.D. Bright fluorescence from individual single-walled carbon nanotubes. *Nano Lett.* (2011). doi:10.1021/nl200077t
70. Kim, J. H., Heller, D.A., Jin, H., Barone, P.W., Strano, M.S. The rational design of nitric oxide selectivity in single-walled carbon nanotube near-infrared fluorescence sensors for biological detection. *Nat. Chem.* (2009). doi:10.1038/nchem.332
71. Giraldo, J. P., Landry, M.P., Kwak, S.Y., Jain, R.M., Strano, M.S. A Ratiometric Sensor Using Single Chirality Near-Infrared Fluorescent Carbon Nanotubes: Application to In Vivo Monitoring. *Small* (2015). doi:10.1002/smll.201403276
72. Bisker, G., Park, H.D, Iverson, N.M., Ahn, J., Kruss, S., Strano, M.S. Protein-targeted corona phase molecular recognition. *Nat. Commun.* (2016). doi:10.1038/ncomms10241
73. Harvey, J. D. Jena, P.V., Baker, H.A., Mittal, J., Heller, D.A. A carbon nanotube reporter of microRNA hybridization events in vivo. *Nat. Biomed. Eng.* (2017). doi:10.1038/s41551-017-0041
74. Heller, D. A., Jin, H., Martinez, B.M., Patel, D., Ha, T., Silverman, S.K., Strano, M.S. Multimodal optical sensing and analyte specificity using single-walled carbon nanotubes. *Nat. Nanotechnol.* (2009). doi:10.1038/nnano.2008.369
75. Beyene, A. G., Demirer, G. S. & Landry, M. P. Nanoparticle-Templated Molecular Recognition Platforms for Detection of Biological Analytes. *Curr. Protoc. Chem. Biol.* (2016). doi:10.1002/cpch.10
76. Park, J., Takmakov, P. & Wightman, R. M. In vivo comparison of norepinephrine and dopamine release in rat brain by simultaneous measurements with fast-scan cyclic voltammetry. *J. Neurochem.* (2011). doi:10.1111/j.1471-4159.2011.07494.x
77. Sulzer, D., Cragg, S. J. & Rice, M. E. Striatal dopamine neurotransmission: Regulation of release and uptake. *Basal Ganglia* (2016). doi:10.1016/j.baga.2016.02.001
78. Landry, M. P., Vukovic, L., Kruss, S., Strano, M.S. Comparative Dynamics and Sequence Dependence of DNA and RNA Binding to Single Walled Carbon Nanotubes. *J. Phys. Chem. C* (2015). doi:10.1021/jp511448e
79. Heller, D., Jeng, E.S., Yeung, T.K., Martinez, B.M., Strano, M.S. Optical detection of DNA conformational polymorphism on single-walled carbon nanotubes. *Science* (2006). doi:10.1126/science.1120792
80. Salem, D. P., Gong, X., Lin, A.T., Koman, V.B., Dong, J., Strano, M.S. Ionic Strength-

Mediated Phase Transitions of Surface-Adsorbed DNA on Single-Walled Carbon Nanotubes. *J. Am. Chem. Soc.* (2017). doi:10.1021/jacs.7b09258
81. Bergler, F. F., Schöppler, F., Brunecker, F. K., Hailman, M. & Hertel, T. Fluorescence spectroscopy of gel-immobilized single-wall carbon nanotubes with microfluidic control of the surfactant environment. *J. Phys. Chem. C* (2013). doi:10.1021/jp403711e
82. Jena, P. V., Safaee, M. M., Heller, D. A. & Roxbury, D. DNA-Carbon Nanotube Complexation Affinity and Photoluminescence Modulation Are Independent. *ACS Appl. Mater. Interfaces* (2017). doi:10.1021/acsami.7b05678
83. Schöppler, F. *et al.* Molar Extinction Coefficient of Single-Wall Carbon Nanotubes. *J. Phys. Chem. C* (2011). doi:10.1021/jp205289h
84. Weiss, J. N. The Hill equation revisited: uses and misuses. *FASEB J.* (1997). doi:0892-6638/97/0011
85. Kurganov, B. I., Lobanov, A. V., Borisov, I. A. & Reshetilov, A. N. Criterion for Hill equation validity for description of biosensor calibration curves. *Anal. Chim. Acta* (2001). doi:10.1016/S0003-2670(00)01167-3
86. Johnson, R. R., Johnson, a T. C. & Klein, M. L. Probing the Structure of DNA− Carbon Nanotube Hybrids with Molecular Dynamics. *Nano Lett.* (2008). doi:10.1021/nl071909j
87. Manohar, S., Tang, T. & Jagota, A. Structure of homopolymer DNA-CNT hybrids. *J. Phys. Chem. C* (2007). doi:10.1021/jp071316x
88. Gigliotti, B., Sakizzie, B., Bethune, D. S., Shelby, R. M. & Cha, J. N. Sequence-independent helical wrapping of single-walled carbon nanotubes by long genomic DNA. *Nano Lett.* (2006). doi:10.1021/nl0518775
89. Dukovic, G., Balaz, M., Doak, P., Berova, N.D., Zheng, M., McLean, R.S., Brus, L.E. Racemic single-walled carbon nanotubes exhibit circular dichroism when wrapped with DNA. *J. Am. Chem. Soc.* (2006). doi:10.1021/ja062095w
90. Johnson, R. R., Kohlmeyer, A., Johnson, a T. C. & Klein, M. L. Free energy landscape of a DNA-carbon nanotube hybrid using replica exchange molecular dynamics. *Nano Lett.* (2009). doi:10.1021/nl802645d
91. Patra, N., Song, Y. & Král, P. Self-assembly of graphene nanostructures on nanotubes. *ACS Nano* (2011). doi:10.1021/nn102531h
92. Jena, P. V., Roxbury, D., Galassi, T.V., Heller, D.A. A Carbon Nanotube Optical Reporter Maps Endolysosomal Lipid Flux. *ACS Nano* (2017). doi:10.1021/acsnano.7b04743
93. Perebeinos, V. & Avouris, P. Phonon and electronic nonradiative decay mechanisms of excitons in carbon nanotubes. *Phys. Rev. Lett.* (2008). doi:10.1103/PhysRevLett.101.057401
94. Sau, J. D., Crochet, J. J., Doorn, S. K. & Cohen, M. L. Multiparticle exciton ionization in shallow doped carbon nanotubes. *J. Phys. Chem. Lett.* (2013). doi:10.1021/jz400049c
95. Humphrey, W., Dalke, A. & Schulten, K. VMD: Visual molecular dynamics. *J. Mol. Graph.* (1996). doi:10.1016/0263-7855(96)00018-5
96. Huang, J. & Mackerell, A. D. CHARMM36 all-atom additive protein force field: Validation based on comparison to NMR data. *J. Comput. Chem.* (2013). doi:10.1002/jcc.23354
97. Vanommeslaeghe, K., Hatcher, E., Acharya, C., Mackerell, A.D. CHARMM general force field: A force field for drug-like molecules compatible with the CHARMM all-atom

additive biological force fields. *J. Comput. Chem.* (2010). doi:10.1002/jcc.21367
98. Yu, W., He, X., Vanommeslaeghe, K. & MacKerell, A. D. Extension of the CHARMM general force field to sulfonyl-containing compounds and its utility in biomolecular simulations. *J. Comput. Chem.* (2012). doi:10.1002/jcc.23067
99. Phillips, J. C., Braun, R., Wang, W., Gumbart, J., Schulten, K.. Scalable molecular dynamics with NAMD. *Journal of Computational Chemistry* (2005). doi:10.1002/jcc.20289
100. Darden, T., York, D. & Pedersen, L. Particle mesh Ewald: An N·log(N) method for Ewald sums in large systems. *J. Chem. Phys.* (1993). doi:10.1063/1.464397
101. Grimme, S., Antony, J., Ehrlich, S. & Krieg, H. A consistent and accurate ab initio parametrization of density functional dispersion correction (DFT-D) for the 94 elements H-Pu. *J. Chem. Phys.* (2010). doi:10.1063/1.3382344
102. Grimme, S., Ehrlich, S. & Goerigk, L. Effect of the damping function in dispersion corrected density functional theory. *J. Comput. Chem.* (2011). doi:10.1002/jcc.21759
103. Beyene, A. G., Delevich, K., Del Bonis-O'Donnell, J.T., Wilbrecht, L., Landry, M.P. Imaging striatal dopamine release using a nongenetically encoded near infrared fluorescent catecholamine nanosensor. *Sci. Adv.* (2019). doi:10.1126/sciadv.aaw3108
104. Anderson, B. A., Kuwabara, H., Dean, F.W., Yantis, S. The role of dopamine in value-based attentional orienting. *Curr. Biol.* (2016). doi:10.1016/j.cub.2015.12.062
105. Solanto, M. V. Dopamine dysfunction in AD/HD: Integrating clinical and basic neuroscience research. in *Behavioural Brain Research* (2002). doi:10.1016/S0166-4328(01)00431-4
106. Cohen, J. & Uchida, N. Neuron-type specific signals for reward and punishment in the ventral tegmental area. *Nature* (2012). doi:10.1038/nature10754.Neuron-type
107. Eshel, N., Tian, J., Bukwich, M. & Uchida, N. Dopamine neurons share common response function for reward prediction error. *Nat. Neurosci.* (2016). doi:10.1038/nn.4239
108. Berke, J. D. What does dopamine mean? *Nature Neuroscience* (2018). doi:10.1038/s41593-018-0152-y
109. Steinberg, E. E., Keiflin, R., Boivin, J.R., Witten, I.B., Janak, P.H. A causal link between prediction errors, dopamine neurons and learning. *Nat. Neurosci.* (2013). doi:10.1038/nn.3413
110. Hamid, A. A., Pettibone, J.R., Mabrouk, O.S., Berke, J.D. Mesolimbic dopamine signals the value of work. *Nat. Neurosci.* (2015). doi:10.1038/nn.4173
111. Salamone, J. D. & Correa, M. The Mysterious Motivational Functions of Mesolimbic Dopamine. *Neuron* (2012). doi:10.1016/j.neuron.2012.10.021
112. Dudman, J. T. & Krakauer, J. W. The basal ganglia: From motor commands to the control of vigor. *Current Opinion in Neurobiology* (2016). doi:10.1016/j.conb.2016.02.005
113. Lotharius, J. & Brundin, P. Pathogenesis of parkinson's disease: Dopamine, vesicles and α-synuclein. *Nat. Rev. Neurosci.* (2002). doi:10.1038/nrn983
114. Weinstein, J. J. *et al.* Pathway-Specific Dopamine Abnormalities in Schizophrenia. *Biological Psychiatry* (2017). doi:10.1016/j.biopsych.2016.03.2104
115. Volkow, N. D., Fowler, J. S., Wang, G.-J. & Swanson, J. M. Dopamine in drug abuse and addiction: results from imaging studies and treatment implications. *Mol. Psychiatry*

(2004). doi:10.1038/sj.mp.4001507
116. Clements, J., Lester, R., Tong, G., Jahr, C. & Westbrook, G. The time course of glutamate in the synaptic cleft. *Science (80-.).* (1992). doi:10.1126/science.1359647
117. Greengard, P. The neurobiology of slow synaptic transmission. *Science (80-.).* (2001). doi:10.1126/science.294.5544.1024
118. Zoli, M., Torri, C., Ferrari, R., Jansson, A., Agnati, L.F.. The emergence of the volume transmission concept. in *Brain Research Reviews* (1998). doi:10.1016/S0165-0173(97)00048-9
119. Cragg, S. J. & Rice, M. E. DAncing past the DAT at a DA synapse. *Trends in Neurosciences* (2004). doi:10.1016/j.tins.2004.03.011
120. Marder, E. Neuromodulation of Neuronal Circuits: Back to the Future. *Neuron* (2012). doi:10.1016/j.neuron.2012.09.010
121. Berridge, C. W. & Waterhouse, B. D. The locus coeruleus-noradrenergic system: Modulation of behavioral state and state-dependent cognitive processes. *Brain Research Reviews* (2003). doi:10.1016/S0165-0173(03)00143-7
122. Tritsch, N. X. & Sabatini, B. L. Dopaminergic Modulation of Synaptic Transmission in Cortex and Striatum. *Neuron* (2012). doi:10.1016/j.neuron.2012.09.023
123. Piekarski, D. J., Boivin, J. R. & Wilbrecht, L. Ovarian Hormones Organize the Maturation of Inhibitory Neurotransmission in the Frontal Cortex at Puberty Onset in Female Mice. *Curr. Biol.* (2017). doi:10.1016/j.cub.2017.05.027
124. Robinson, D. L., Venton, B. J., Heien, M. L. A. V & Wightman, R. M. Detecting subsecond dopamine release with fast-scan cyclic voltammetry in vivo. in *Clinical Chemistry* (2003). doi:10.1373/49.10.1763
125. Heien, M. L. A. V., Johnson, M. A. & Wightman, R. M. Resolving neurotransmitters detected by fast-scan cyclic voltammetry. *Anal. Chem.* (2004). doi:10.1021/ac0491509
126. Garris, P. A. & Wightman, R. M. Regional Differences in Dopamine Release, Uptake, and Diffusion Measured by Fast-Scan Cyclic Voltammetry. *Neuromethods: Voltammetric Methods in Brain Systems* (1995). doi:10.1385/0-89603-312-0:179
127. Mohebi, A., Pettibone, J.R., Hamid, A.A., Berke, J.D. Dissociable dopamine dynamics for learning and motivation. *Nature* (2019). doi:10.1038/s41586-019-1235-y
128. Liu, C., Kershberg, L., Wang, J., Schneeberger, S. & Kaeser, P. S. Dopamine Secretion Is Mediated by Sparse Active Zone-like Release Sites. *Cell* **172,** 706–718.e15 (2018).
129. Roxbury, D., Jena, P.V., Williams, R.M., Heller, D.A. Hyperspectral Microscopy of Near-Infrared Fluorescence Enables 17-Chirality Carbon Nanotube Imaging. *Sci. Rep.* (2015). doi:10.1038/srep14167
130. Ding, J. B., Takasaki, K. T. & Sabatini, B. L. Supraresolution Imaging in Brain Slices using Stimulated-Emission Depletion Two-Photon Laser Scanning Microscopy. *Neuron* (2009). doi:10.1016/j.neuron.2009.07.011
131. Wang, F., Dukovic, G., Brus, L. E. & Heinz, T. F. The optical resonances in carbon nanotubes arise from excitons. *Science (80-.).* (2005). doi:10.1126/science.1110265
132. Edelstein, A. D., Tsuchida, M.A., Vale, R.D., Stuurman, N. Advanced methods of microscope control using μManager software. *J. Biol. Methods* (2014). doi:10.14440/jbm.2014.36
133. Vandenberg, A., Piekarski, D. J., Caporale, N., Munoz-Cuevas, F. J. & Wilbrecht, L. Adolescent maturation of inhibitory inputs onto cingulate cortex neurons is cell-type

specific and TrkB dependent. *Front. Neural Circuits* (2015). doi:10.3389/fncir.2015.00005